

# Magnetic Fields and the Formation of Aspherical Planetary Nebulae

Dissertation

zur

Erlangung des Doktorgrades (Dr. rer. nat.)

der

Mathematisch-Naturwissenschaftlichen Fakultät

der

Rheinischen Friedrich-Wilhelms-Universität Bonn

vorgelegt von

**Marcelo de Lima Leal Ferreira**

aus

Rio de Janeiro, Brasilien

Bonn, 2014

Angefertigt mit Genehmigung der Mathematisch-Naturwissenschaftlichen Fakultät  
der Rheinischen Friedrich-Wilhelms-Universität Bonn

1. Gutachter: Dr. Wouter Vlemmings
2. Gutachter: Prof. Dr. Frank Bertoldi

Tag der Promotion: 21. November 2014

Erscheinungsjahr: 2015

Diese Dissertation ist auf dem Hochschulschriftenserver der ULB Bonn unter  
[http://hss.ulb.uni-bonn.de/diss\\_online](http://hss.ulb.uni-bonn.de/diss_online)  
elektronisch publiziert.

Gedruckt mit Unterstützung des Deutschen Akademischen Austauschdienstes.



# Abstract

*The general evolution of stars with initial mass between 0.8 and 8  $M_{\odot}$  is believed to be well understood until the last stages, when significant mass loss starts. However, an initially spherical star may evolve into an asymmetrical planetary nebula (PN), whereas the underlying mechanism to this process remains as a puzzle. Until about a decade ago, it was believed that stars in the asymptotic giant branch (AGB) phase were still spherically symmetric. Nevertheless, observations performed in the last years show that, for some sources, elongated and asymmetrical envelopes can already be detected during the AGB phase. In the following pre-PN and planetary nebula phases, a variety of morphologies is observed, and the sources are classified into round, elliptical/elongated, bipolar, quadrupolar, multipolar, spiral, collimated lobes and irregular. It is unknown which mechanism or set of mechanisms is responsible for this change of morphology, making this topic to be one of the most discussed by the evolved stars community.*

*To shed some light on this problem, three AGB stars (IK Tau, R Scl, and V644 Sco) and one red supergiant (VY CMa) were observed at optical wavelengths. We analyzed their dust scattered emission and searched for signs of upcoming asymmetries in their circumstellar envelope. The observations in R band reveal that the dust envelope of the AGB star IK Tau has a global elliptical morphology, and the presence of a central waist is discussed. The observation of VY CMa shows a complex morphology in the very extended nebula that surrounds the source. Furthermore, for the first time the detached shell around the AGB star V644 Sco was imaged, allowing a better investigation of the mass-loss episodes of the source. The detached shell around R Scl was also imaged and analyzed. The results reported in this thesis add together with previous works, confirming that the loss of spherical symmetry in the circumstellar envelope of evolved stars can already start during the AGB phase.*

Moreover, we studied one of the mechanisms that can play a role in the shaping process of the circumstellar envelope of these sources: magnetic fields. For this purpose, we investigated 22 GHz  $H_2O$  maser observations around five sources: four AGB stars (IK Tau, RT Vir, IRC+60370, and AP Lyn) and one pre-PN (OH231.8+4.2). By analyzing the linear and circular polarization in the masers, we detected the presence of magnetic field in four of these five sources. We measured the field strengths to be from a few tens up to a few hundreds of milligauss in the  $H_2O$  maser region (at a few tens of astronomical units from the star). Comparing our results with magnetic field measurements from the literature, obtained at different distances with respect to the stars, we tried to determine the most plausible geometry of the magnetic fields for the observed sources. However, it is not yet definitive if the observed fields are toroidal, poloidal, or dipole.

The influence of magnetic fields on the shaping process of the circumstellar envelope of evolved stars is still unclear, but their detection around AGB stars, pre-PNe and PNe supports that they might play a role in the process. More measurements of the strength of the fields, also at different distances to the stars, and the investigation of the geometry of the fields are fundamental for providing better constraints to models, and for the better understanding of this subject.

# Contents

<b>Abstract</b>	<b>v</b>
<b>1 Introduction and context</b>	<b>5</b>
1.1 The Evolution of Low- and Intermediate-Mass Stars . . . . .	5
1.1.1 Dust . . . . .	10
1.2 Observation Techniques . . . . .	12
1.2.1 Very Long Baseline Interferometry . . . . .	12
1.2.2 Observations with the ESO 3.6 m Telescope and the PolCor Instrument . . . . .	14
1.3 Types of Radiation Analyzed in this Thesis . . . . .	14
1.3.1 Masers . . . . .	15
1.3.2 Scattered Light Polarization . . . . .	17
<b>2 Asymmetries on evolved stars</b>	<b>21</b>
2.1 Morphologies of (pre-)Planetary Nebulae . . . . .	21
2.2 Mechanisms to Shape the Mass Loss of Evolved Stars . . . . .	25
2.2.1 Binary Interactions . . . . .	25
2.2.2 Magnetic Fields . . . . .	27
2.2.3 Further Mechanisms to Shape the Mass Loss of Evolved Stars	32
<b>3 The Magnetic Field of a Binary Evolved Star</b>	<b>35</b>
3.1 Introduction . . . . .	36
3.2 Observations and Data Reduction . . . . .	38
3.3 Results . . . . .	39

3.3.1	Masers Location . . . . .	39
3.3.2	Linear Polarization . . . . .	43
3.3.3	Circular Polarization . . . . .	43
3.4	Discussion . . . . .	46
3.4.1	Kinematics . . . . .	46
3.4.2	Polarization . . . . .	48
3.5	Conclusions . . . . .	50
<b>4</b>	<b>Magnetic fields around AGB stars</b>	<b>53</b>
4.1	Introduction . . . . .	54
4.2	Observations and data reduction . . . . .	56
4.3	Results . . . . .	59
4.3.1	IK Tau . . . . .	60
4.3.2	RT Vir . . . . .	64
4.3.3	IRC+60370 . . . . .	66
4.4	Discussion . . . . .	66
4.4.1	Non-detection toward AP Lyn . . . . .	66
4.4.2	Spatial distribution of the masers . . . . .	67
4.4.3	Stellar Position . . . . .	68
4.4.4	Distance of the masers to the star . . . . .	69
4.4.5	Magnetic field detection . . . . .	74
4.5	Conclusions . . . . .	77
<b>5</b>	<b>Asymmetric CSE around evolved stars</b>	<b>91</b>
5.1	Introduction . . . . .	92
5.2	Observations and Data Reduction . . . . .	93
5.3	Results . . . . .	97
5.3.1	IK Tau . . . . .	98
5.3.2	VY CMa . . . . .	100
5.4	Discussion . . . . .	105
5.4.1	IK Tau . . . . .	105
5.4.2	VY CMa . . . . .	107
5.5	Conclusions . . . . .	109



<b>6 Detached shells</b>	<b>111</b>
6.1 Introduction . . . . .	112
6.2 Observations and Data Reduction . . . . .	114
6.3 Results . . . . .	114
6.3.1 R Scl . . . . .	117
6.3.2 V644 Sco . . . . .	118
6.4 Discussion . . . . .	122
6.4.1 R Scl . . . . .	122
6.4.2 V644 Sco . . . . .	128
6.4.3 The Region Between the Star and the Shell . . . . .	129
6.5 Conclusion . . . . .	131
<b>7 Conclusion</b>	<b>133</b>
7.1 Conclusions . . . . .	133
7.2 Perspectives . . . . .	136
<b>Bibliography</b>	<b>137</b>
<b>Abbreviations</b>	<b>147</b>
<b>Acknowledgements</b>	<b>149</b>
<b>Curriculum Vitae</b>	<b>152</b>



# Chapter 1

## Introduction and context

*In this thesis the origin of asymmetries in the circumstellar envelope developed by many low-/intermediate-mass stars in their late stages of evolution is investigated. These sources maintain their initial spherical symmetry during most of their evolution but, at some point between the asymptotic giant branch and the planetary nebula phases, they develop elongations, bipolar features, jets, and/or point symmetrical structures, etc. The exact moment when the metamorphosis occurs is not yet well determined, nor are the mechanisms triggering and characterizing this process.*

*In the present chapter, an overview on the main aspects of stellar evolution and of the observation techniques used in this work is given. This overview serves as an introduction to the analysis presented in the following chapters.*

### 1.1 The Evolution of Low- and Intermediate-Mass Stars

Low- and intermediate-mass stars are stars with initial masses between 0.8 and 8  $M_{\odot}$ . A detailed description of their evolution can be found in several standard books of astrophysics and scientific review articles (e.g. Swihart 1968; Clayton 1983; Maciel 1999; Habing & Olofsson 2004; Herwig 2005). Thus, here only a brief review of the main evolutionary stages of low- and intermediate-mass stars is given.

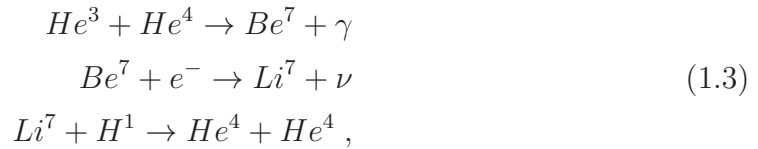
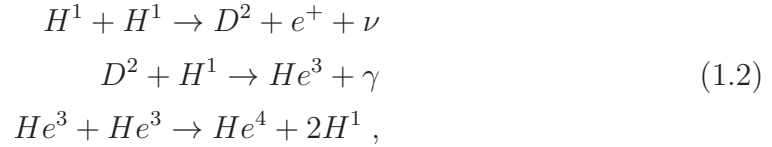
The primordial composition of a star depends on the abundances of elements of

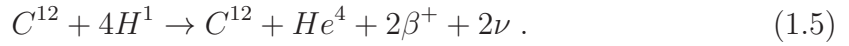
the environment in which the star is born which, in turn, depends on the generation of the star: Older generations of stars feed the interstellar medium with heavier elements, enriching newer regions of star formation. However, hydrogen will always be the major component of the newborn star.

Already during the phase when the molecular cloud contracts to give birth to the star, at the pre-main sequence phase, the temperature and pressure raise, and a fusion reaction that creates  $\text{He}^3$  occurs:



However, the abundance of deuterium in the star is very low and it gets quickly exhausted in the fusion process. Thus, the only consequence of this reaction is that the contraction of the star is slowed down. Once in the main sequence phase, which is the longest evolutionary stage of the star, the most significant reactions are the proton-proton chains PPI, PPII, and PPIII, shown respectively in Eqs. 1.2, 1.3, and 1.4, and the CNO cycle, shown in Eq. 1.5:

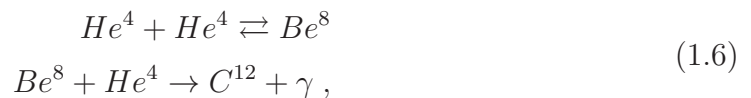




All these reactions give stability to the star by counterbalancing the gravitational pressure and when about 10%-20% of the hydrogen in the core is consumed, the core contracts and the outer layers of the shell expand. From here on the evolution of low-mass ( $0.8 M_{\odot}$ - $1.8 M_{\odot}$ ) and intermediate-mass ( $1.8 M_{\odot}$ - $8 M_{\odot}$ ) stars differs.

In low-mass stars the thermonuclear reactions stop in the core after the hydrogen is exhausted in that region, and no counterbalance for the gravitational pressure is present anymore. As a result the core contracts, raising its temperature and heating up the neighboring shell. Once the temperature crosses a critical value, the burning of hydrogen into helium is triggered in this shell, which in turn heats up the outer layers, which expand as a result, leading to an increase of luminosity of the star. At this stage the surface area of the star is larger but also colder, inducing the star to become redder. This is the red giant phase.

The core continues to contract until its temperature is high enough for the helium to be processed, generating carbon and oxygen through the nuclear reactions shown in Eqs. 1.6 and 1.7.



At this stage the core is degenerate, meaning that its pressure does not increase as a function of the temperature anymore. Therefore, the core does not expand and the nuclear reactions heat up the core even more. The consequence is an extreme intensification of the helium burning, leading to a process of runaway fusion. This process is called the helium flash, which leads to a further temperature increase in the core until the degeneracy is overcome and the gas can expand and cool down.

This is a fast process, and the luminosity of the stellar core during the flash is of about  $10^{11} L_{\odot}$  (*i.e.*, comparable to a supernova) for a few hours. Most of this energy is used to expand the envelope and, therefore, does not reach the surface.

Now, the star is again in a stable condition, burning helium in its core and hydrogen in the neighboring layers. This phase of helium core burning is about ten times shorter than the previous hydrogen core burning phase. When the helium in the core is exhausted, the core contracts again, raises once more its temperature and prompts the outer layers to heat up and expand. Afterward, the core is an inactive core of carbon and oxygen. However, the temperature of the surrounding layers reaches a level that is high enough for the helium burning to occur in those regions, while the outer layers continue burning hydrogen. This is the asymptotic giant branch (AGB) phase.

In the AGB phase, the interplay of the different layers of the star determines the stellar surface luminosity. During the first years in the AGB phase, corresponding to  $\sim 3 \times 10^5$  years for a star with initial mass of  $1 M_{\odot}$ , the helium burning layer dominates over the hydrogen burning layer in terms of the contribution to the stellar surface luminosity. With time, the helium burning shell becomes thinner and the hydrogen layer becomes more prominent and, in comparison to the helium burning shell, more luminous. Eventually, the luminosities originating from the different shells start to oscillate in an inverse correlation pattern. This is the phase of instability of the AGB star, in which thermal pulses are produced. The thermally pulsing phase culminates in intense winds that eject the external layers of the star and the source turns into a pre-planetary nebula (pPN).

Observations of AGB stars have revealed the presence of thin detached shells (width/radius  $< 0.1$ ) around some of the stars. It is believed that the formation of these shells is related to a short but intense event of mass loss related to a helium shell flash, followed by a period where the mass loss is interrupted or is very low, before the stable wind blows again. Such an eruptive mass-loss event produces an expanding shell with a higher velocity than the one from the material previously expelled. Therefore, the faster shell sweeps up the slower one, creating a detached shell (Mattsson et al. 2007). The detached shells around AGB stars will be discussed

in detail in Chapter 6 of this thesis.

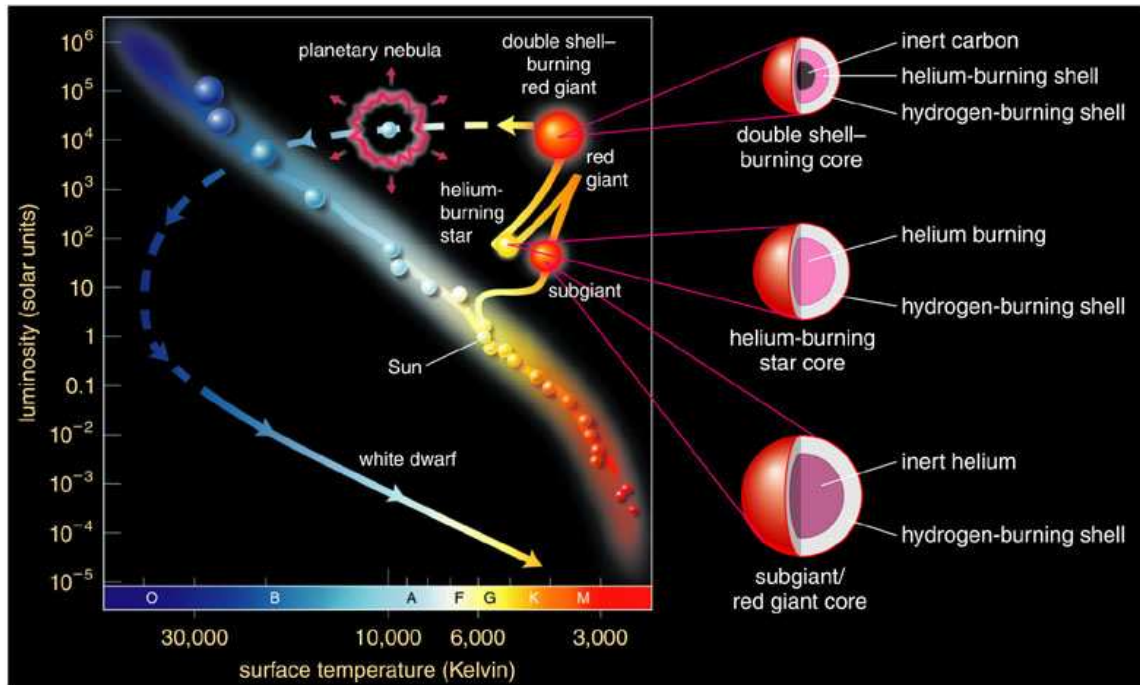
The planetary nebula phase is explained by the interacting stellar winds model (Kwok et al. 1978) that suggests that the material previously ejected by the AGB star, expanding as a slow wind ( $\sim 15$  km/s), is compressed by a later fast wind ( $\sim 10^3$  km/s) from the central star (the hot exposed core). The swept-up dense shell is then ionized by the ultraviolet radiation from the central star and the planetary nebula is produced. Once the nebula dissipates in the interstellar medium, the central star remains and it is called a white dwarf.

An intermediate-mass star evolves in the same way as a low-mass star until the hydrogen starts to be burned in the first shell around the core. While the hydrogen burning takes place in the shell, the core continues to contract and the temperature continues to raise, heating up the outer layers. The mechanisms that induce the star to become a red giant are not fully understood, but in this phase the outer layers are expanded and the surface of the star has cooled down.

The temperature in the core continues to raise until the helium burning can begin. In this case the core is not completely degenerate, so that the burning induces the pressure to increase which, in turn, acts to expand the core, decreasing the temperature. Another contraction of the core induces the helium burning phase to settle down until this element is exhausted. When this point is reached, the core collapses again, raising the temperature of the surrounding layers even more and, now, themselves start to burn helium and the hydrogen is burned in a layer around the former. The nuclear reactions in the layers continue until dynamical instabilities and pulses eject the stellar envelope and the (pre-)PN phase is reached.

A visualization of the evolution of a low-/intermediate-mass star is given in Figure 1.1, which shows the evolutionary track of these sources in the Hertzsprung-Russell (HR) diagram. The HR diagram is a plot of the surface temperature (horizontal axis) against luminosity (vertical axis) of the star.

The description in the previous paragraphs illustrates the general scenario of the evolution of low- and intermediate-mass stars. However, not all the details of this process are fully known, and how the ejected layers get shaped to the variety of



Copyright © 2004 Pearson Education, publishing as Addison Wesley.

Figure 1.1: Evolutionary track of a low-/intermediate-mass star, from the main sequence to the white dwarf phase, in the HR diagram.

morphologies observed in PNe is yet to be understood (see Chapter 2).

### 1.1.1 Dust

Dust is an important component of AGB stars and it strongly affects the thermodynamical, hydrodynamical, and chemical structure of the source. From all the astronomical sources with dust formation, AGB stars are responsible for more than 80% of the mass deposited in the disk of the Galaxy (Weinzielr 1991; Sedlmayr 1994).



The dust grains formed in the stars can be of distinct shapes, as three-dimensional solid grains, flat or curved (two-dimensional) plates, or fractal like structures. They are generated from a chain of chemical reactions under favorable conditions that will finally result in solid macroscopic products, depleting the molecular composition of the gas. Once the hot matter of the star expands, it cools down and dilutes at larger distances from the star, so that the necessary conditions for the grains to emerge are reached. When the temperature is below 1500 K, certain atoms and molecules combine to form stable clusters that may gather other molecules, growing into macroscopic specimens. The initial process of dust crystallization occurs in a narrow spatial region, where the temperature is between 1300 K and 700 K, and in outer neighboring regions, with lower temperature and density, the grains are found in conditions favorable to grow (Sedlmayr 1994).

Some specific molecules are more significant for the initial step of cluster condensation, as they fulfill the following criteria for dust production: (i) The molecule should be significantly abundant in the gas, (ii) the bounding energy of the molecule should not be high, and (iii) the molecule should be able to condense in a high temperature environment (between 700 K and 1300 K). Only a small number of species fulfill these important requirements for the initial step of dust formation (Gail & Sedlmayr 1986, 1987; Sedlmayr 1994).

Furthermore, dust grains can capture photons, scatter (see Section 1.3.2) them isotropically and gather part of their momentum. Therefore, dust plays a key role in the mass-loss process of evolved stars and dust-driven winds are one of the major mechanisms to eject the material into the medium. Moreover, the presence of dust in the circumstellar envelope (CSE) is closely related to pulsation of the stars (Jura 1986; Lafon & Berruyer 1991).

The radiation scattered by dust can provide us with significant observational data, which can be used to map the dust distribution in a given source. In Chapters 5 and 6, observations of this kind are used to investigate asymmetries in the CSE of evolved stars and structures like detached shells around AGB stars.

## 1.2 Observation Techniques

Two distinct observation methods were used for obtaining the data analyzed in this thesis. For the analysis described in Chapters 3 and 4, the data were observed with Very Long Baseline Interferometry (VLBI), while for the investigation in Chapters 5 and 6, the targets have been observed with an optical telescope and a polarimeter. Thus, in the following the VLBI observations are described in Section 1.2.1 and the details of the optical observations are reported in Section 1.2.2.

### 1.2.1 Very Long Baseline Interferometry

The principle of interferometry is to observe a given source with multiple telescopes simultaneously and to combine the signals from the individual telescopes to simulate a single telescope with the diameter of the biggest baseline ( $B$ ; distance between two given telescopes) of the interferometer. That allows observations with small angular resolutions ( $\theta'$ ) even when the observed radiation has longer wavelengths ( $\lambda$ ), as  $\theta' \sim \lambda/B$ . This technique is based on the principle of interference, which states that two incoming beams with the same frequency can produce constructive interference and thus increase the amplitude of the signal, if they are in phase.

The individual telescopes that compose an astronomical interferometer are located in different positions on Earth (or in outer space, in the case of space VLBI). Such difference in location causes the signal of a given source to travel different paths before being detected by each individual telescope. As these paths do not have the same length, the signals observed by the individual telescopes are not necessarily in phase (Figure 1.2). In order to combine the signals, these differences in the path lengths have to be corrected for.

In contrast to conventional interferometry, VLBI does not require the telescopes that compose the interferometer to be physically connected by a transmission line (e.g., a coaxial cable), allowing the baselines to be much larger and increasing the angular resolution of the observations up to the order of milliarcseconds (mas). While longer baselines define the angular resolution of the observations, the shorter

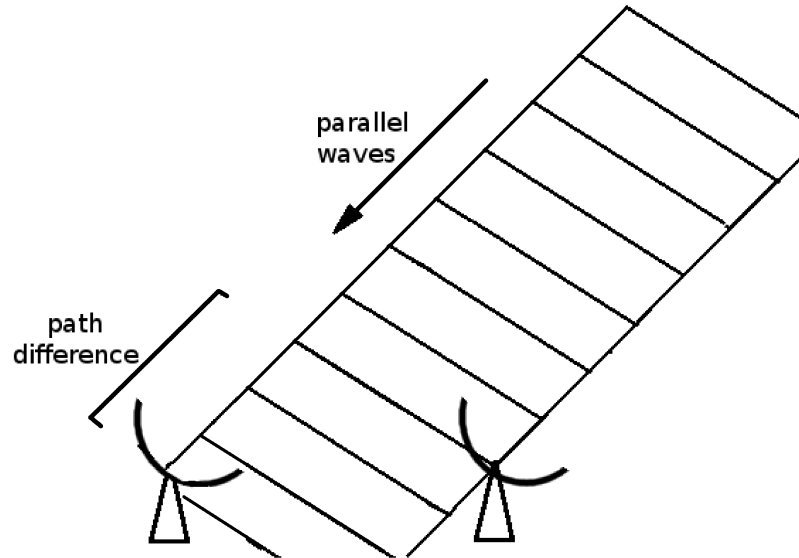


Figure 1.2: The signal of the target follows parallel paths before being detected by the antennas that make up the interferometer. As the antennas are located in different positions, these paths do not have the same length, and the path difference induces a phase delay that has to be corrected for.

baselines are needed to detect the extended structures of the source. As in VLBI the telescopes are not physically connected, the correction for phase delay is not made in real time. For each telescope, the data are recorded in the facility where the telescope is located, and the correction for phase delay is made in a future date at a correlation facility. Further specific calibrations that are not needed in observations with conventional interferometry but with VLBI are also made during that stage, like the correction for geophysical and Earth orientation effects, such as tectonic motion influence (Walker 1999).

The high spatial resolution achieved with VLBI observations is essential for the identification of individual maser features, while the very high spectral resolution is needed for the detection of the small Zeeman splitting in the masers. The Very Long Baseline Array (VLBA) is a Very Long Baseline Interferometer made up of ten antennas spread across the territory of the United States of America. These antennas make up baselines from 200 km up to 8600 km and cover the radio frequency bands

from 300 MHz to 86 GHz<sup>1</sup>, making the VLBA ideal for the observations of H<sub>2</sub>O masers at  $\sim 22$  GHz, which were investigated in this thesis.

### 1.2.2 Observations with the ESO 3.6 m Telescope and the PolCor Instrument

The ESO 3.6 m Telescope<sup>2</sup> is located at the La Silla Observatory in Chile. Its primary mirror has 3.57 m of diameter and the image quality of the telescope is better than 0.2 arcsec at the zenith. I used this telescope together with the visitor instrument PolCor to perform the observations I discuss in Chapters 5 and 6. PolCor stands for Polarimeter and Coronagraph. This instrument uses the “lucky image” method, which has the aim of decreasing the consequences of the seeing effect. The seeing effect is the consequence of instabilities in the atmosphere, which results in a given observation being smudged out while the observed radiation is integrated into an image. The “lucky image” method consists of observations of short-exposure images with a high frame rate, avoiding the seeing to have a big effect in each individual image. After the observations are finished, the individual images (the sharpest ones) are shifted with respect to a reference point in order to compensate for the seeing effect. This method can improve the quality of the images by a factor of 20%–30% (Ramstedt et al. 2011). For more details on these observations, see Section 5.2.

## 1.3 Types of Radiation Analyzed in this Thesis

Radiations of different nature were analyzed in this work. In Chapters 3 and 4, I report the analysis of H<sub>2</sub>O maser observations around evolved stars, and investigate their polarization due to magnetic fields. In Chapters 5 and 6, I present observations of dust scattered light. Thus, in this section I describe the nature of masers in 1.3.1 and the mechanism of scattered light polarization in 1.3.2.

---

<sup>1</sup><https://science.nrao.edu/facilities/vlba/other/Intro%20to%20the%20VLBA>

<sup>2</sup><http://www.eso.org/public/teles-instr/lasilla/36/>

### 1.3.1 Masers

#### The Nature of Masers

When an electron in an atom is found in an energy level higher than its ground state, it can undergo a transition to a lower energy level by emitting a photon in a process of spontaneous emission. Another possibility is stimulated emission, where an incident photon with the same energy as the transition energy induces the transition to occur, resulting in a second photon with the same wavelength, phase, plane of polarization, and direction as the incident photon to be emitted (Maitland & Dunn 1969).

When an external mechanism causes the population level of the atoms/molecules of the medium to be inverted, *i.e.*, the electrons are mostly found in an energy level higher than the ground state, then a main requirement for a maser emission to occur is satisfied. Under such conditions, each transition from the upper to the lower level will produce a photon able to stimulate further transitions with the same properties, in a ripple effect. This chain of events produces a maser (*Microwave Amplification by Stimulated Emission of Radiation*) when the resulting radiation is in the microwave regime. Often the prime input photon that gives rise to the ripple effect is generated by a spontaneous emission. This is then amplified by the stimulated emissions (Litvak 1974). A sketch of the maser emission process is presented in Figure 1.3.

#### Masers Around AGB Stars

Masers can be observed at different distances from evolved stars and they can be emitted by different molecules. The three maser species that are mainly detected around AGB stars and pre-PNe are radiated by SiO, H<sub>2</sub>O, and OH. When occurring around AGB stars they trace, respectively, (i) the dust formation zone from  $\sim 2$  AU up to  $\sim 5$  AU from the stellar surface, (ii) the region at tens of AU from the stellar surface, and (iii) the region more distant to the star, from  $\sim 100$  AU up to thousands of AU, where the emission at 1665/1667 GHz originates from a more inward location than the emission at 1612 GHz (Figure 1.4). Toward pre-PNe, the H<sub>2</sub>O masers

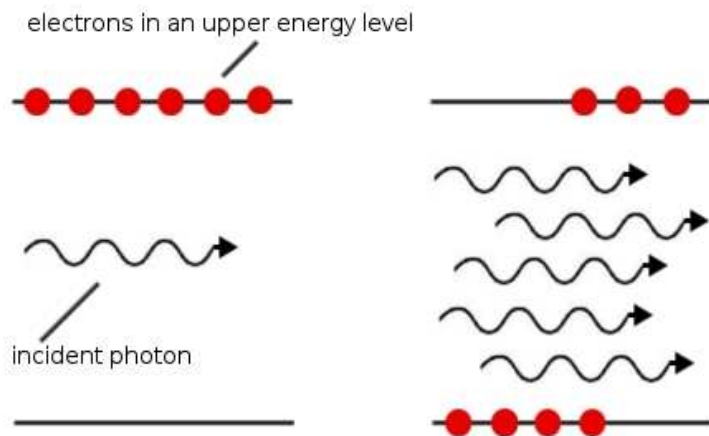


Figure 1.3: Sketch of the maser emission process. The circles indicate electrons on an upper energy state (left). An incident photon stimulates one electron to perform a transition to the lower state, emitting a photon with the same properties as the incident one. The process repeats itself in a ripple effect, and the original input radiation is amplified (right).

can be found at similar or greater distances than OH masers (e.g. Cohen 1987). Hereafter, I will refer to these regions as SiO, H<sub>2</sub>O, and OH maser regions.

### Maser Polarization

When an atom experiences the influence of a magnetic field, its energy states are split into multiple sub-levels. Under these conditions, a given transition that would otherwise occur between two well-determined energy levels, now may occur between a number of different sub-levels. This is the principle of the Zeeman effect (Zeeman 1897) and the distance between the Zeeman sub-levels is proportional to the strength of the field. Thus, the analysis of the Zeeman effect is a powerful tool to derive the strength of the magnetic field acting in the medium. The measurement of the small Zeeman sub-levels splitting in non-paramagnetic molecules like H<sub>2</sub>O or

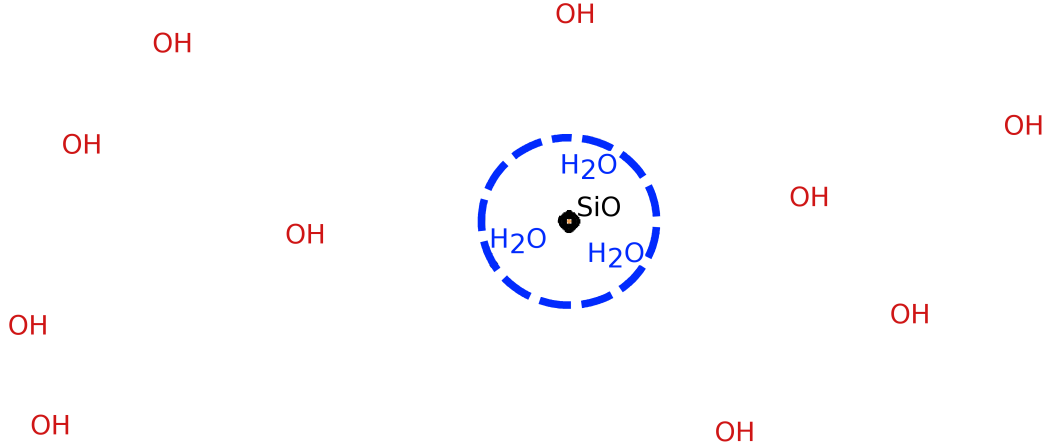


Figure 1.4: Sketch of masers around an AGB star. The orange dot represents the surface of the AGB star and the black continuous and the blue dashed circles represent the outer radius of the SiO and the H<sub>2</sub>O maser regions, respectively. The outer radius of the OH maser region is bigger than the size of this figure. The SiO masers are found closer to the star, between  $\sim 2$  AU and  $\sim 5$  AU from the surface, the H<sub>2</sub>O masers can be detected at tens of AU to the star, and the OH masers emit from an outer region from  $\sim 100$  AU to thousands of AU.

SiO provides the projected value of the field strength  $B \cos \theta$ , where  $\theta$  is the angle between the direction of the field and the direction of propagation of the maser. On one hand, if the stimulated emission is greater than the Zeeman splitting, the circular polarization in the masers can be dominated by non-Zeeman effects. On the other hand, if the splitting is higher than the stimulated emission, the decay rate, and rate of redistribution of the level population over the different maser sub-states, the circularly polarized masers will be mainly induced by the Zeeman effect. Additionally, linearly polarized masers occur when the masers start to be saturated and the stimulated emission approaches the decay rate. Fields stronger than 0.1 mG are sufficient to polarize maser emissions (Goldreich et al. 1973; Vlemmings 2007).

### 1.3.2 Scattered Light Polarization

In Chapters 5 and 6 of this thesis the results derived from the observation of dust scattered polarization of evolved stars are presented. Thus, an overview on

polarization by scattering is given in the following.

An incident radiation is composed of an electric field ( $\vec{E}$ ) perpendicular to a magnetic field ( $\vec{B}$ ). The direction of propagation ( $\vec{S}$ ) is perpendicular to both, the electric and magnetic fields. If unpolarized, the directions of  $\vec{E}$  and  $\vec{B}$  vary randomly in the plane perpendicular to  $\vec{S}$ . When linearly polarized, the directions of  $\vec{E}$  and  $\vec{B}$  are located on a preferential axis, which will be the case of study in the following.

When propagating, the linearly polarized radiation induces the atoms/molecules of the medium to oscillate in a parallel direction to  $\vec{E}$ . Oscillating charges are constantly being accelerated and, therefore, radiate. The emission from these oscillating dipoles is called scattered light, and it will be completely linearly polarized in the direction perpendicular to  $\vec{S}$  from the original radiation. The scattered light parallel to  $\vec{S}$  will be unpolarized and no scattered light is radiated in the direction of the dipole oscillating axis. A scheme of this process is shown in the left part of Figure 1.5.

In the general case of unpolarized incident radiation, the scattered light will be emitted in every direction, as the axis of oscillation of the atom/molecule is not constant. As such, the scattered light will be totally linearly polarized in any direction that is perpendicular to  $\vec{S}$  and the scattered light emitted in an angle between  $0^\circ$  and  $90^\circ$  will be partially polarized, being more polarized for larger angles – adopting  $0^\circ$  in direction of  $\vec{S}$ , and  $90^\circ$  perpendicular to it – (Figure 1.5, right part; Hecht 2001).

Analogously, dust grains also scatter radiation and even when the grain is irradiated by an unpolarized light, the scattered light is generally polarized. In this case the polarization occurs when non-spherical grains are aligned by some mechanism, resulting in the major axis of the grains having a preferred direction. The degree of polarization will not only depend on the angle of scattering, but also on the wavelength of the incident radiation and on the properties of the grains (e.g. Whittet 1996; Draine 2003). Therefore, the observation of dust scattered light can provide us with significant information about the dust distribution and dust properties in the target.

The polarization state of an incident radiation can be described by the Stokes



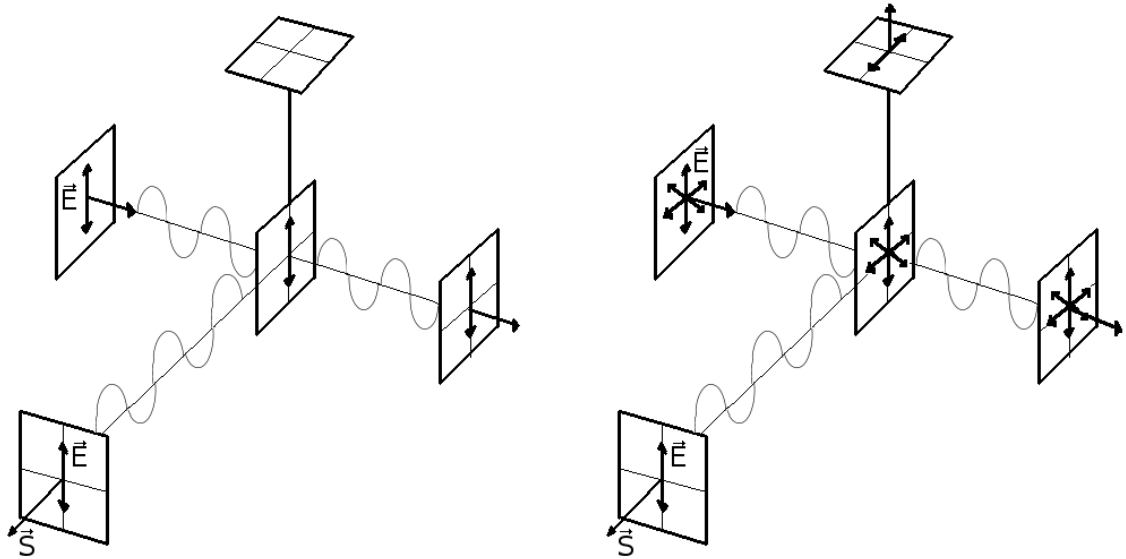


Figure 1.5: Polarization by scattering. Left: Linearly polarized incident radiation. Right: Unpolarized incident radiation. Figure adapted from Hecht (2001).

parameters  $I$ ,  $Q$ ,  $U$ , and  $V$ . The total intensity is defined by  $I$ , the intensity of linear polarization is described by  $Q$  and  $U$ , and the intensity of circular polarization by  $V$ . These quantities are used in Chapters 3, 4, 5, and 6, and are further discussed in those chapters.



# Chapter 2

## Asymmetries on evolved stars

*In this chapter a brief overview is given on asymmetries of mass loss from AGB stars and planetary nebulae, and on the mechanisms discussed by the scientific community that may play a role in the shaping process of these evolved stars. The role of a companion to the star, magnetic fields, accretion disks, torii, and the interaction with the interstellar medium are discussed.*

### 2.1 Morphologies of (pre-)Planetary Nebulae

In Section 1.1 the evolution of low- and intermediate-mass stars was described. One unsolved characteristic in the evolution of these objects is the apparent morphological transition that occurs between the AGB phase and the PN phase. While the mass loss during the AGB phase exhibits (almost) spherical symmetry, planetary nebulae present a huge variety of morphologies and only a fraction of them are spherical. About 62% of the pre-PNe and 75% of the PNe in the Galaxy are classified as non-spherical (Manchado 2003, 2012). The variety of shapes inspired morphological classifications including round, elliptical/elongated, bipolar, quadrupolar, multipolar, irregular, collimated lobes, spiral shaped, and subclasses like the presence of multiple shells and point symmetric features (Figure 2.1). It should be highlighted that the morphological classification reflects the projection of the objects on the sky. As a consequence, a fraction of the objects classified as round nebulae may actually

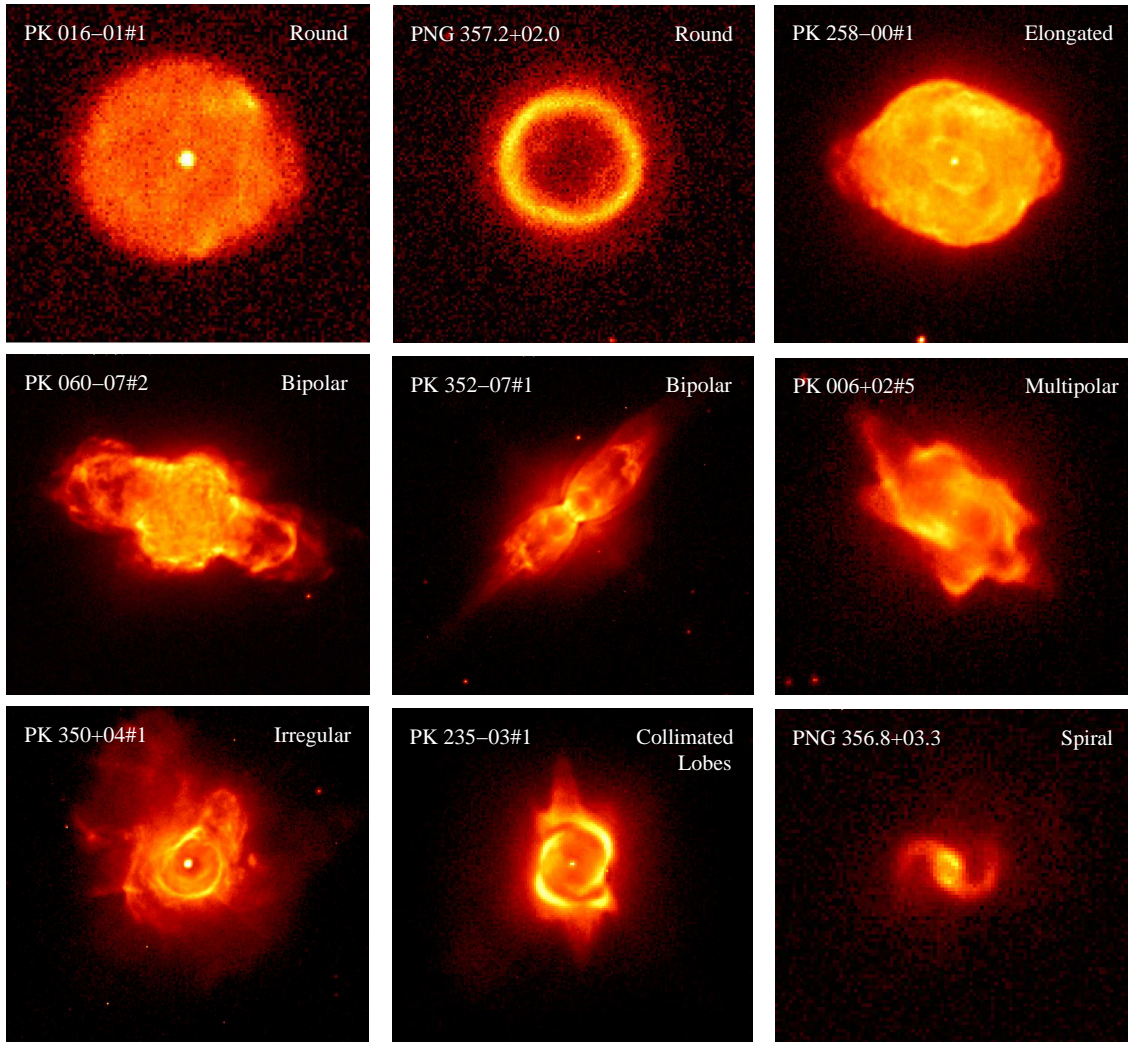


Figure 2.1: Examples of different morphologies of young planetary nebulae. All images show the H $\alpha$  emission and were taken with the Hubble Space Telescope (HST). The source identification and primary morphological classification is given, respectively, on the top left and top right of each image. Figure adapted from Sahai et al. (2011).

have a non-spherical three-dimensional geometry. Manchado (2003) estimates that in his sample of 255 sources 17% of the PNe observed as round nebulae may actually be elliptical nebulae seen pole on. In the same sample, the contribution of bipolar nebulae seen as round nebulae due to projection effects should be negligible due to

the low number of bipolar nebulae in the sample.

The morphological classification of a given source is often not straightforward. For example, a particular PN may show different shapes and structures when observed in different wavelengths, since radiation from distinct processes may trace different regions of the nebula. Moreover, even when observed in a given band, a longer exposure time may reveal structures not seen in observations with shorter exposures (Figure 2.2). Therefore, when classifying a sample of objects, it is important that each individual target is observed under the same observational settings.

Several studies investigated the correlation between the PN morphology and its properties (e.g. Stanghellini et al. 1993; Corradi & Schwarz 1995; Gorny et al. 1997). Some results from these studies include:

- PNe with multiple shells have central stars that are older than those with single shell.
- Bipolar PNe are, on average, closer located to the disk of the Galaxy than elliptical PNe.
- The central stars of bipolar PNe are among the hottest central stars of all PNe.
- The nebular abundances of bipolar PNe have overabundances of He, N, and Ne.
- Compared to other morphological types, bipolar PNe are produced by more massive progenitors.

Despite the broad investigations on the various morphologies of PNe, it is not yet clear how PNe are shaped. Several mechanisms are proposed to explain the morphological metamorphosis of these evolved stars and I discuss them in the following section.

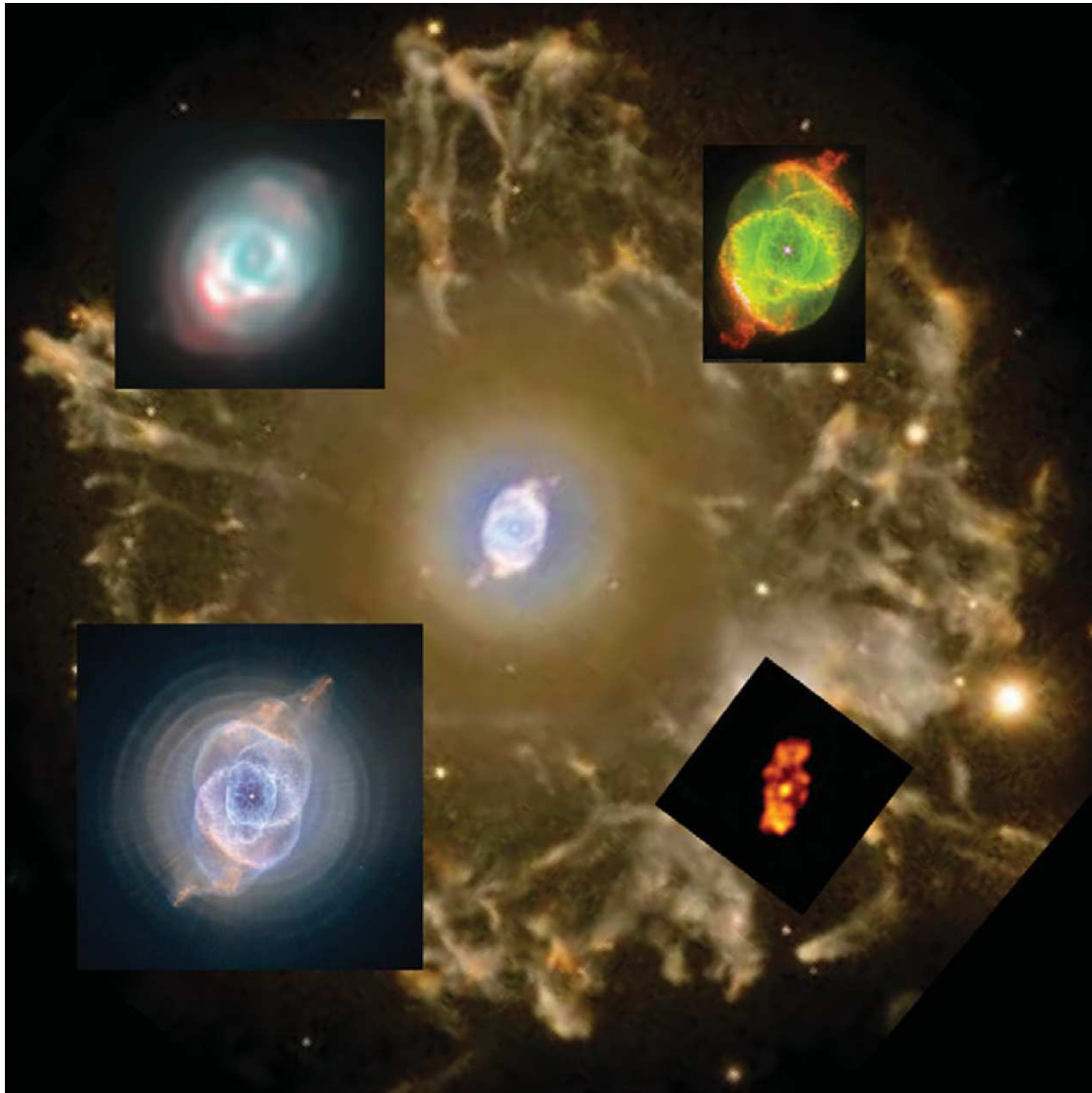


Figure 2.2: Five independent observations of the planetary nebula NGC 6543 show different structures of the source, leading to different observed shapes of the PN. In the center a deep multi-band ( $[\text{N II}] \lambda 6584 \text{ \AA} + [\text{O III}] \lambda 5007 \text{ \AA}$ ) image observed with the Nordic Optical Telescope in La Palma, Spain is shown (credits: R. L. M. Corradi, D. R. Gonçalves). Superimposed to this, it is shown an amateur ground-based image (top left), a multi-band ( $\text{H}\alpha + [\text{N II}] \lambda 6584 \text{ \AA} + [\text{O I}] \lambda 6300 \text{ \AA}$ ) image taken with the HST (credits: J. P. Harrington, K. J. Borkowski, and NASA; top right), a multi-band ( $\text{H}\alpha + [\text{N II}] \lambda 6584 \text{ \AA} + [\text{O III}] \lambda 5007 \text{ \AA} + \text{FR505N}$ ) image observed with the HST (credits: NASA, ESA, HEIC, and The Hubble Heritage Team STScI/AURA; bottom left), and a X-ray image from the Chandra X-Ray Observatory (credits: Chu et al. and NASA; bottom right). Figure from Shaw (2012).

## 2.2 Possible Mechanisms to Shape the Mass Loss of Evolved Stars

In this section, mechanisms that might act in the shaping process of mass loss from evolved stars are discussed. Two of them will be described in more detail: binary interactions (Section 2.2.1) and magnetic fields (Section 2.2.2). The need of binary interactions in the formation of a bipolar planetary nebula is postulated by several authors (e.g. Soker 1997). Possibly the presence of a companion is also needed to maintain a magnetic field around the evolved star (e.g. Nordhaus et al. 2007). The second mechanism, magnetic fields, is in the focus of Chapters 3 and 4 of this thesis, where the detection of fields around a sample of evolved stars is reported. Moreover, alternative mechanisms like accretion disks, central waists/torii/disks, and the interaction with the interstellar medium (ISM) are also briefly discussed in Section 2.2.3. It shall be highlighted that more than one mechanism may act simultaneously in the shaping process of evolved stars, and that one given mechanism may induce another one.

### 2.2.1 Binary Interactions

Several authors (e.g. Soker 1997; De Marco 2009) suggest that the majority of PNe are generated from the interaction of a binary system and that the existence of a companion to the central star is needed to form an asymmetric planetary nebula. This scenario is called Binary Hypothesis. In this hypothesis, binary systems are classified as: (i) binaries with a very wide orbit (when the orbital period  $T_{orb}$  of the system is much larger than the total time of formation and life of the planetary nebula  $T_{PN}$ ), (ii) binaries with a wide orbit (when  $T_{orb}$  is similar to  $T_{PN}$ ), (iii) binaries in a close orbit (when the gravitation interaction is significant) that do not undergo a common-envelope phase, (iv) binaries that undergo a common-envelope phase but do not merge, (v) binaries that undergo a common-envelope interaction that results in a merger, and (vi) binary systems composed of a star and a massive planet or a brown dwarf. According to the Binary Hypothesis these classes of binary systems can, in contrast to the other suggested mechanisms, generate most of the

observed morphological cases of PNe, like: almost spherical haloes with elliptically shaped inner regions (or bubbles), jets, bipolar shapes, axisymmetrical structures, spiral structures, disks, and small features.

Nordhaus & Blackman (2006) found that even a low-mass companion (less than  $0.3 M_{\odot}$ ) can influence the mass-loss event of an AGB star, ultimately resulting in an ejection (partially or fully) of the AGB envelope. Such ejection can occur in the equatorial plane when the mass loss occurs via the transfer of the orbital energy from the companion or, when the companion is not able to directly eject the envelope, the ejection can occur in the polar direction due to induced differential rotation. In addition, the companion may disrupt into a disk that can then influence the morphological evolution of the mass loss of the AGB star as described in Section 2.2.3.

Population synthesis calculations predict that  $\sim 46000$  PNe with nebular radius less than  $\sim 0.9$  pc currently reside in the Galaxy (Moe & De Marco 2006). However, observations estimate the existence of only about 8000 PNe with the same nebular radius in the Galaxy (Jacoby 1980; Peimbert 1990, 1993). The disagreement could be explained if not all low-/intermediate-mass stars form a PN, as discussed by De Marco (2009). If the number of PNe predicted by the population synthesis calculations is multiplied by the fraction of stars that undergo a binary common-envelope phase ( $\sim 13\%$ ; Han 1995; De Marco 2006), there should be  $\sim 6000$  PNe with radius less than  $\sim 0.9$  pc produced by common-envelope interaction in the Galaxy. However, that result leads to the fact that 75% of the total number of PNe is produced by common-envelope interaction. The other 25% of PNe would be derived from weaker binary interactions or from single stars. If this scenario is close to reality, the majority of PNe are generated from binary systems. However, the fraction of 75% of PNe produced by common-envelope interaction is far more than the 10%–21% fraction of close binaries on PN central stars (Bond 1979; Bond et al. 1992; Bond 1995, 2000; De Marco et al. 2008; Miszalski et al. 2009).

An alternative fate is required to describe the evolution of the  $\sim 38000$  missing PNe. A possible solution for that problem could be different time scales for the evolution of the central star and for the evolution of the nebula. In the two extreme



cases, if the star evolves too slowly, at the time it gets hot enough to ionize the gas, the nebula would have been already dissipated into the ISM. On the other hand, if the evolution of the star is too fast, it would illuminate the nebula only for a brief period of time (Kwok 1994). Moreover, it is suggested that interactions with a stellar or a substellar companion could prevent the star from following its natural evolution, and that about 20% of the low- and intermediate-mass stars would not even ascend the AGB (De Marco & Soker 2011).

Another poorly understood detail is the suggestion that bipolar PNe are generated by more massive progenitors compared to other morphological types of PNe (e.g., Stanghellini et al. 1993; Corradi & Schwarz 1995). Soker (1998) claims that binary stars that undergo a common-envelope phase (producing a bipolar PN) would more frequently have higher masses, whereas stars with lower masses would go through a more significant interaction with the companion along the red giant phase (due to its greater radius) and never ascend the AGB. This appears to support the Binary Hypothesis, however, De Marco (2009) points out that the masses determined for primaries known to belong to a close binary system are not particularly high.

In conclusion, so far neither the binary nor the single star evolution are clearly supported by observations for the formation of asymmetrical planetary nebulae (De Marco 2009). It is expected that the investigation on this topic will continue for years to come.

### 2.2.2 Magnetic Fields

In recent years, several observational studies have reported the detection of magnetic fields around evolved stars (e.g. Vlemmings et al. 2002, 2005; Amiri et al. 2011; Pérez-Sánchez et al. 2011). Most of these detections are obtained from maser observations, where different maser species characterize different radial distances to the star (see Section 1.3.1 for details). An example of maser measurements of magnetic fields is reported by Vlemmings et al. (2006), where a toroidal magnetic field is detected almost perpendicular to the collimated outflow of the young pre-planetary nebula W43A.

The origin of these fields is still under investigation by the scientific community. A possible scenario for their origin is a connection of the birth of magnetic fields with the large mass-loss rate and the short evolutionary phase of post-AGB stars. The magnetic fields would drive the AGB winds by magnetic pressure, making the winds reach high speeds (from a few tens up to  $10^3$  km/s) and leading to the formation of highly collimated pPNe (García-Segura et al. 2005).

In general, two distinct shaping scenarios that involve magnetic fields are suggested: In the first case the field is sustained around a single star and acts as the main force shaping the source via magnetic pressure. In the second case a companion to the evolved star is needed to maintain the field at levels necessary to significantly influence the shaping process of the mass loss. In this section I discuss these two scenarios and the role of magnetic fields on the shaping process of evolved stars.

### **Is a Companion Needed to Maintain a Magnetic Field Around an Evolved Star?**

If magnetic fields are the dominant process responsible for shaping evolved single stars, then the field must be sustained over the AGB lifetime. For that to be possible, it is suggested that the differential rotation between the core and the envelope of the star has to be re-supplied via convection or another mechanism. Otherwise, the presence of a companion (a secondary star, a brown dwarf, or a massive planet) would be mandatory to spin up the envelope of the star, providing the missing angular momentum to sustain a strong magnetic field around the source (Nordhaus et al. 2007; Blackman 2009).

Furthermore, according to stellar evolution models, the transfer of angular momentum from the stellar core to the CSE in single stars is insufficient to provide a rotation for the envelope that fulfills the requirements of current MHD simulations to generate a bipolar PN (García-Segura et al. 2014). However, Cantiello et al. (2014) highlight that the physics of the transport of angular momentum inside stars is not yet well understood, and that stellar evolution models fail to explain the observed rotation of stellar cores.

The need for a companion to sustain a magnetic field around the star is sup-

ported by Soker (2006), who states that even though the detections of magnetic fields around evolved stars are significant, this does not necessarily imply that the magnetic fields are the main force in the shaping process. Moreover, if a companion is present, it will have the most influential effect in the mass-loss process, making the magnetic field, at most, play a secondary role. However, locally enhanced magnetic fields could lead to the formation of moderately elliptical PNe, but not account for lobes, jets, etc.

The planetary nebula NGC 1360, which has a bipolar jet, brings extra ingredients to this debate. Attempts of detecting a binary system in this source led to negative results (Wehmeyer & Kohoutek 1979). Despite the fact that such results do not discard the possibility of a merger in the past, the current rotational velocity of the central star is not unusually high, which would be expected if a merger had occurred (García-Díaz et al. 2008). Even without evidence for the presence of a companion in the center of this source, Jordan et al. (2012) reported the detection of a magnetic field around its central star. While early measurements pointed to a strong field of the order of 3 kG (Jordan et al. 2005), a re-analysis of the data agrees with a much weaker field, of  $244 \pm 162$  G (Jordan et al. 2012).

Despite the discussion on whether a strong magnetic field can survive around a single star or if a companion is needed, Bujarrabal et al. (2001) showed that, for a sample of 37 pPNe, in about 80% of the sources the radiation pressure itself is unable to provide the amount of energy observed in the fast collimated molecular flows, leading to the need of an alternative source of energy to drive the outflows (Bujarrabal et al. 2001). If the magnetic fields act only locally instead of globally, they cannot be responsible for collimating the outflows and another source of energy is needed to explain the phenomena. Furthermore, while radiation and rotation alone are insufficient to provide the necessary energy for the collimated outflows, a combination of rotation, differential rotation and a large scale magnetic field remains as a possible source of the missing energy. Furthermore, large scale fields are supported by theory, simulations, and observations of coronae and jets. In conclusion, dynamos of single stars, magnetic fields fueled by binary interaction, or accretion engines cannot be ruled out around evolved stars (Blackman 2009).

### How Significant are Magnetic Fields for the Shaping Process of Evolved Stars?

Several magnetohydrodynamic (MHD) simulations explore how magnetic fields can act to change the morphology of evolved stars. These simulations assume that the field is present around the source yet do not explore its origin. In the following, some relevant results from these simulations are discussed.

Large-scale structures, like thick disks and polar jets, can be successfully generated by single stars with a super-wind triggered by internal MHD effects (Pascoli & Lahoche 2008). Moreover, single stars with masses above  $1.3 M_{\odot}$ , that spin up their rotation just prior to the PN ejection, can create morphologies from spherical to extremely bipolar even without a magnetic field (in this case, the stellar rotation rate would drive the shaping process). However, if a magnetic field is included in the simulations, more elongated shapes are produced, transforming the prior spherical models into elliptical ones, and the bipolar models into more collimated ones. Thus, a toroidal field is able to constrain the motion of the flow and elliptical or bipolar nebulae are produced even when the slow wind is spherical. Together with the interaction of the slow and fast winds, the field can also generate a pair of collimated outflows. A stronger field is also capable of blowing out a pair of jets from the nebula, making the magnetic collimation the most likely mechanism to explain point-symmetric nebulae, and a potentially significant agent in the origin of FLIERs (Fast Low Ionization Emission Regions) (García-Segura et al. 1999). Further comparisons between purely hydrodynamic and MHD models were done by Dennis et al. (2009), who investigated the morphological consequences of the absence/presence of the fields. This work found profound differences in the shaping process when a (nested) magnetic field was included.

Other simulations of single stars with global magnetic fields show that the mass loss of the source can be induced to occur preferentially around the equator, leading to the formation of a disk. This phenomenon is supplemented by the simultaneous appearance of a polar jet (Pascoli & Lahoche 2010). A dipole magnetic field of only a few Gauss on the star surface and an isotropic wind acceleration mechanism are sufficient to produce an equatorial disk if the magnetic field energy on the surface

of the star is comparable or greater than the energy (thermal plus kinetic) of the otherwise spherical stellar wind. This is due to the plasma being forced to flow along the dipole field lines near the star and the outflow being denser in the magnetic equatorial plane, producing a disk. However, independently of the strength of the field, there will always be an exterior region where the outflow will be dominated by the kinetic energy of the wind. This model is valid even for very slowly rotating stars (unless by the fact that rotation should be needed to maintain the field), and if more massive stars are more suitable for maintaining a strong field, that could justify the indication that bipolar PNe are generated by more massive stars (Matt et al. 2000).

Quadrupolar outflow is another global structure that can be produced by magnetic fields, as shown by Matt et al. (2006). A dipole field can amplify the rotational energy of the core of the star and blow the envelope generating such a morphology.

In summary, magnetic fields can have pronounced effects on the morphology of evolved stars but only if they can survive into and beyond the AGB phase. In the single star scenario, if viable, the fields can be the primary shaping mechanism. However, if indeed a companion is needed to sustain the field, then the companion may act as the main shaping agent, with the fields acting as a secondary shaping agent.

## Discussion

Many open questions related to the presence of magnetic fields around evolved stars remain. De Marco (2009) highlight that in order to investigate the correlation between magnetic fields and companions to the star, the detection of magnetic fields, especially in binary systems with well-determined parameters, is needed to provide the observational constraints for the models. Blackman (2009) reinforces this necessity by pointing out that the magnetic field measurements statistically lead to field geometries that drop off like  $r^{-1}$  to  $r^{-3}$ , where  $r$  is the distance to the star. This range of possibilities only provides a weak constraint on the models.

Furthermore, the question whether the observed fields are local or global needs to be answered. On this issue, a global magnetic field was observed around the

planetary nebula S216 through Faraday rotation<sup>1</sup>. If such a field is confirmed and found to originate from the PN itself, the measurement is of extreme importance as it would show that global fields can exist around PNe. However, it is not yet clear if the field detected in this source is stellar or interstellar (Uyaniker 2004; García-Segura 2006; Ransom et al. 2008).

In this thesis, I report the detection of magnetic fields around the pre-Planetary Nebula OH231.8+4.2 (Chapter 3) and the asymptotic giant branch stars IK Tau, RT Vir, IRC+60370 (Chapter 4), aiming to increase the number of measurements of magnetic fields around evolved stars and to shed some light on this controversial discussion. These results were also published in Leal-Ferreira et al. (2012, 2013).

### 2.2.3 Further Mechanisms to Shape the Mass Loss of Evolved Stars

In addition to binaries and magnetic fields, alternative mechanisms to shape evolved stars include accretion disks, central waists/torii/disks, interaction with the interstellar medium, and planetary systems. The case of planetary systems is analogous to the binary case, and often a planet is considered to act as the companion of the star. Thus, here I will briefly describe only accretion disks, torii, and the interaction with the Interstellar Medium as possible alternative mechanisms to shape Planetary Nebulae.

#### Accretion Disks

An accretion disk can be formed through mass transfer from a close companion, or if a merger spins up the AGB star rotation to breakup, a disk can be formed. In the presence of a disk, a jet can be produced even though the mechanism on how the jet is launched is not yet understood (Morris 1987; Soker & Livio 1994; Balick & Frank 2002). Furthermore, a wobbling accretion disk could induce a precession in the jet and give rise to point symmetric features (Livio & Pringle 1996, 1997).

---

<sup>1</sup>The Faraday Effect is the rotation of the polarization direction of the radiation induced by the component of the magnetic field of the medium that is in the direction of the radiation propagation (Faraday 1845).

## Torii

While the generation of an accretion disk requires the presence of a secondary star, a torus might also be able to form without the presence of a companion (e.g., Bjorkman & Cassinelli 1993; Frank 1995; Dorfi & Hoefner 1996). The formation of a torus around a single star can be due to different reasons. As an example, one possible cause is the presence of cool starspots in the AGB photosphere (Frank 1995). Observations indicate that the presence of a torus is associated with jets, and these jets typically appear a few hundred years after the torus (Huggins 2007).

## Interaction with the Interstellar Medium

The material expelled by the AGB star is subject to interaction with the ISM. Several properties are important when such interaction occurs, like the relative velocity between the source and the medium, the density of the ISM, the stellar progenitor mass, and the Galactic magnetic field. The proper motion of the source will cause the star to appear displaced from the geometrical center of the envelope. Furthermore, simulations show that the interaction with the interstellar medium can generate bow shocks and elongated tails. If a Galactic magnetic field of a few micro Gauss is considered, the modeled features become even more collimated (Villaver et al. 2012, 2014). However, at least in models where the Galactic magnetic field has not been taken into account, the simulations show that for stars more massive than  $3.5 M_{\odot}$  the interaction with the ISM is expected not to leave any morphological imprint on the source when it reaches the PN phase (Villaver et al. 2012).





## Chapter 3

# Rotten Egg Nebula: The magnetic field of a binary evolved star

The analysis and results reported in this chapter are published by Leal-Ferreira et al. 2012 (A&A, 540, 42)

*Most of the Planetary Nebulae (PNe) observed are not spherical. The loss of spherical symmetry occurs somewhere between the Asymptotic Giant Branch (AGB) phase and the PNe phase. The cause of this change of morphology is not yet well understood, but magnetic fields are one of the possible agents. The origin of the magnetic field remains to be determined, and potentially requires the presence of a massive companion to the AGB star. Therefore, further detections of the magnetic field around evolved stars, and in particular those thought to be part of a binary system, are crucial to improve our understanding of the origin and role of magnetism during the late stages of stellar evolution. One such binary is the pre-PN OH231.8+4.2, around which a magnetic field has previously been detected in the OH maser region of the outer circumstellar envelope.*

*We aim to detect and infer the properties of the magnetic field of the pre-PN OH231.8+4.2 in the H<sub>2</sub>O maser region that probes the region close to the central star. This source is a confirmed binary with collimated outflows and an envelope containing several maser species.*

*In this work we observed the  $6_{1,6}-5_{2,3}$  H<sub>2</sub>O maser rotational transition to determine its linear and circular polarization. As a result of Zeeman splitting, the properties of the*

*magnetic field can be derived from maser polarization analysis. The  $H_2O$  maser emissions of OH231.8+4.2 are located within the inner regions of the source (at a few tens of AU).*

*We detected 30  $H_2O$  maser features around OH231.8+4.2. The masers occur in two distinct regions that are moving apart with a velocity on the sky of 2.3 mas/year. Taking into account the inclination angle of the source with the line of sight, this corresponds to an average separation velocity of 21 km/s. Based on the velocity gradient of the maser emission, the masers appear to be dragged along the direction of the nebula jet. Linear polarization is present in three of the features, and circular polarization is detected in the two brightest features. The circular polarization results imply a magnetic field strength of  $|B_{||}| \sim 45$  mG.*

*We confirm the presence of a magnetic field around OH231.8+4.2, and report the first measurements of its strength within a few tens of AU of the stellar pair. Assuming a toroidal magnetic field, this implies  $B \sim 2.5$  G on the stellar surface. The morphology of the field is not yet determined, but the high scatter found in the directions of the linear polarization vectors could indicate that the masers occur near the tangent points of a toroidal field.*

### 3.1 Introduction

During the final stages of their evolution, low and intermediate mass stars ( $0.8-8 M_{\odot}$ ) evolve from the Asymptotic Giant Branch (AGB) phase to Planetary Nebulae (PNe). During this transition most of these objects lose their spherical symmetry. The process responsible for the change of morphology is, so far, not well understood. Bujarrabal et al. (2001) have shown that, in most cases, the radiation pressure does not have enough energy to drive the acceleration of the fast bipolar flows observed in pre-PNe (pPNe). Moreover, the mass ejection on a preferred axis requires an extra agent to collimate the flow. The possible mechanisms that could both provide the missing energy to drive the fast flows and that could collimate it on a preferred axis are: (i) a companion to the star (either a binary stellar companion or massive planet) and its tidal forces, (ii) disk interaction and (iii) magnetic fields - or a combination of these (Balick & Frank 2002; Frank et al. 2007; Nordhaus et al. 2007, and references therein).

From magneto-hydrodynamic (MHD) simulations, García-Segura et al. (1999) concluded that magnetic fields can indeed have a pronounced effect on shaping stars beyond the AGB stage and that, working together with rotation, they can produce collimated bipolar nebulae and jets. Since then, several other MHD simulations have been designed to investigate how magnetic fields can shape a pPN and, consequently, a Planetary Nebula (e.g., García-Segura et al. 2005; García-Díaz et al. 2008; Dennis et al. 2009).

Observations of the magnetic fields around evolved stars, however, are still rare. Most current magnetic field measurements are performed using Zeeman splitting (Zeeman 1897) of maser lines (e.g., Vlemmings et al. 2001, 2006). Each maser species requires different physical conditions to occur. Therefore, different masers originate in different locations of the studied object. The SiO masers are found close to the central star (CS), in regions with a temperature of  $\sim 1300$  K. The OH masers are generally expected to occur further out, at a few hundred AU from the CS. For AGB stars, the H<sub>2</sub>O maser emission is expected to be intermediate between these two regions; but for a pPN/PN it can be found at a similar or greater radius than the OH maser emission (Cohen 1987; Reid & Menten 1997; Vlemmings & Diamond 2006).

In this work, we aim to investigate the polarization of the H<sub>2</sub>O maser emission toward the pPN OH231.8+4.2 (Rotten Egg Nebula; Calabash Nebula), and infer the properties of its magnetic field. Located at a distance of  $\sim 1540$  pc (Choi et al. 2011, updated from private communication), the bipolar nebula OH231.8+4.2 contains a binary system in its core, where a Main Sequence type A star accompanies an evolved star - the Mira variable QX Pup (Sanchez Contreras et al. 2004). The SiO, H<sub>2</sub>O and OH maser emission toward the Rotten Egg Nebula have been observed several times before (e.g., Morris et al. 1982; Gómez & Rodríguez 2001; Sanchez Contreras et al. 2002; Desmurs et al. 2007; Etoke et al. 2008, 2009). These prior works have shown that the spatial distribution of both the SiO and OH maser emission lie perpendicular to the nebular symmetry axis, consistent with the presence of a torus around the equator of the central star. However, the H<sub>2</sub>O masers (located at only  $\sim 40$  AU from the CS) do not follow the same pattern, and are instead located toward the bipolar structure. Few of the prior studies included polarization mea-

surements. Sanchez Contreras et al. (2002) note that their SiO polarization maps are not reliable and Gómez & Rodríguez (2001) found no circular polarization in the OH maser emission. Etoke et al. (2008, 2009), however, found both circular and linear polarization in the OH masers, and conclude that a well-organized magnetic field seems to be flaring out in the same direction as the outflow.

This paper is structured as follows: Section 2 describes the observations, data reduction, and calibration, and Section 3 includes a presentation of the results. The results are discussed in Section 4 and the concluding analysis is presented in Section 5.

## 3.2 Observations and Data Reduction

The observations of the pPN OH231.8+4.2 were carried out on March 1<sup>st</sup>, 2009, using the NRAO<sup>1</sup> Very Long Baseline Array (VLBA), under project code BV067A. We observed the H<sub>2</sub>O 6<sub>1,6</sub>–5<sub>2,3</sub> rotational transition, at an adopted rest frequency of 22.235081 GHz. We used 2 baseband filters of 1 MHz bandwidth and, following the VLBA H<sub>2</sub>O observations of Desmurs et al. (2007) (hereafter; D07), the filters were centered at  $V_{lsr}$  44.0 km s<sup>-1</sup> and 26.0 km s<sup>-1</sup> respectively. This was done in order to detect both the emission from the northern (NReg; ~30 mas from the CS) and southern regions (SReg; ~40 mas from the CS) of the source. The observations were centered on RA<sub>0</sub>(J2000) = 07<sup>h</sup>42<sup>m</sup>16.93 and Dec<sub>0</sub>(J2000) = -14°42'50".2. Both a lower and a higher spectral resolution correlation were performed. The former was undertaken in full polarization mode (to obtain all 4 Stokes correlations:  $RR$ ,  $LL$ ,  $RL$  and  $LR$ ) over 128 channels, with a resulting nominal channel width of 0.104 km/s. The latter correlation was performed in dual polarization mode (to obtain  $RR$  and  $LL$ ) over 512 channels, with a resulting nominal channel width of 0.026 km/s. The synthesized beam size was ~1.7×0.9 mas. The observations spanned 8 hours, of which 4.7 hours were spent on OH231.8+4.2.

For calibration purposes, we observed J0854+2006. This reference source was

---

<sup>1</sup>The National Radio Astronomy Observatory (NRAO) is a facility of the National Science Foundation operated under cooperative agreement by Associated Universities, Inc.

used to perform bandpass, phase and polarization calibration. We used the Astronomical Image Processing Software Package (AIPS) and followed the data reduction procedure documented by Kemball et al. (1995), and which has been successfully adopted by several authors (e.g., Vlemmings et al. 2001; Surcis et al. 2011).

Using the low resolution data, we created image cubes for the Stokes parameters  $I$ ,  $Q$ ,  $U$  and  $V$ . The noise level measured from these image cubes ranges between  $\sim 3$  and  $\sim 5$  mJy/beam in the emission free channels. From the Stokes  $Q$  and  $U$  images, we derived image cubes for the linear polarization intensity ( $P$ ) and the linear polarization direction (also referred to as electric vector position angle, EVPA).

Using the high resolution data, we created image cubes for the Stokes parameters  $I$  and  $V$ . The noise level measured from these image cubes lay between  $\sim 6$  and  $\sim 10$  mJy/beam in the emission free channels. To estimate the polarization leakage and consequently the minimum believable fractional linear polarization we determined the Stokes  $Q$  and  $U$  limits for the brightest maser feature with no detected polarization. We conclude that, at  $3\sigma$ , the minimum detected fractional polarization is  $\sim 0.1\%$ , a value that is consistent with the self-calibration method used during the data reduction, described in further detail by Leppänen et al. (1995).

In our analysis we adopted a signal-to-noise ratio cutoff of four times the measured noise ( $4\sigma$ ). We define a maser feature to be successfully detected when maser spots located at similar spatial positions (within the beam size) appear and survive the threshold cut in at least 3 consecutive channels. The position of the maser feature is then defined by the emission in the channel where the peak appears (see e.g. Richards et al. 2011).

## 3.3 Results

### 3.3.1 Masers Location

We detected 30 maser features in total, 20 of them located in the NReg and the remaining 10 located in the SReg. In Figure 3.1 we present four plots: 1.a and 1.b correspond to the NReg, and 1.c and 1.d to the SReg. Plots (a) and (c) show the

distribution of all 252 maser spots that comprise the 30 maser features. The dashed vectors indicate the direction of the pPN jet. Plots (b) and (d) show the maser features, scaled by their flux densities (proportional to the size of the triangles), and color-coded according to their line-of-sight velocities. The black line segments, scaled in size by the degree of polarization, show the EVPA (see section 3.3.2). The origin (0,0) of all four plots is centered on the brightest feature we detected, located in the SReg.

In order to aid the comparison of the observations presented by D07 with the current work, we over-plotted both observations in Figure 3.2. Since we did not use phase-referencing during our observations, unlike D07, we do not have a precise value for the absolute maser positions (but we do have accurate relative astrometric information). Therefore, to be able to make this comparison, we assumed a common origin point at the center of the maser emission. We determined this center point by taking the mean position over all the 30 maser features detected here, and over 15 of the 16 features detected by D07. We chose not to include maser feature number 16 from D07 in the analysis, because it is clearly a spatial outlier in the field that contains the features we observed. Figure 3.2 shows the entire field of view (NReg and SReg). The filled triangles represent the 30 features detected in the current work and the hollow squares show the observations from D07. Five regions (2.A, 2.B, 2.C, 2.D and 2.E) are drawn on the figure to facilitate their identification in the text.

In the NReg, the positions of the brightest feature and its surrounding features, are similar to those found by D07, except that the current observations detected more widespread features (region 2.A). On the eastern side of the brightest northern feature, at a separation of  $\sim 30$  mas, we detected only one weak feature, while two features were detected by D07 in this region, at  $\sim 20$  mas from the brightest maser (region 2.B). On the western side of the main feature we detected a group of 7 features that together seem to compose a single extended structure (region 2.C). This group of features does not appear in the observations of D07. Instead, they found only two features in that same region. Moreover, the emissions we detected in the NReg are contained within a much wider North-South area ( $\sim 26$  mas) than that in the D07 image ( $\sim 13$  mas).

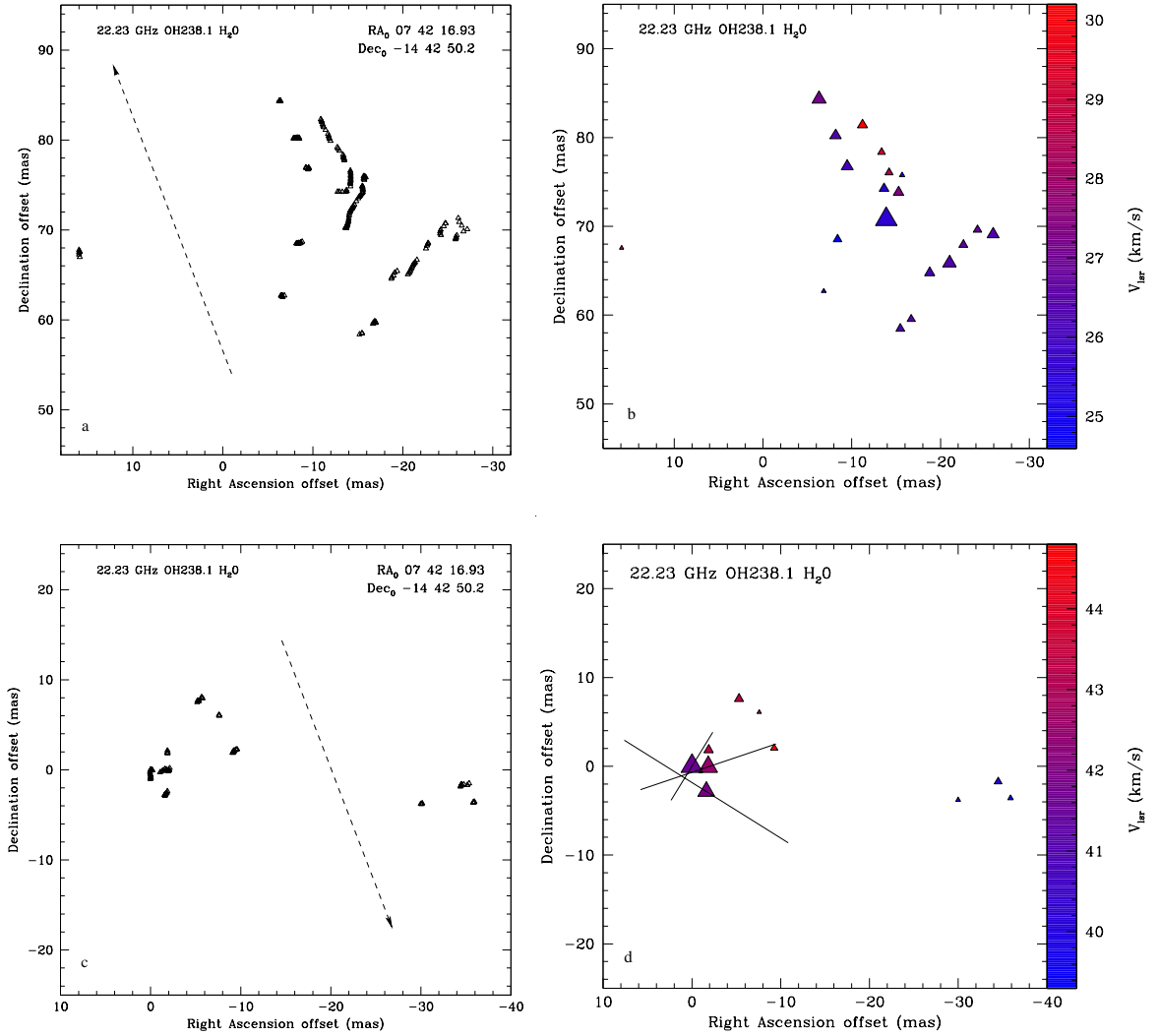


Figure 3.1: Plots a and b (top) corresponds to NReg, and plots c and d (bottom) to SReg. Plots a and c (left) show the position of all the measured maser spots, and plots b and d (right) present the maser features. On plots a and c the dashed vectors indicate the direction of the pPN jet. On plots b and d the size of the triangles are scaled by the maser fluxes, and the color scale is related to the velocity. The black lines represent the EVPA and intensity of the linear polarization.

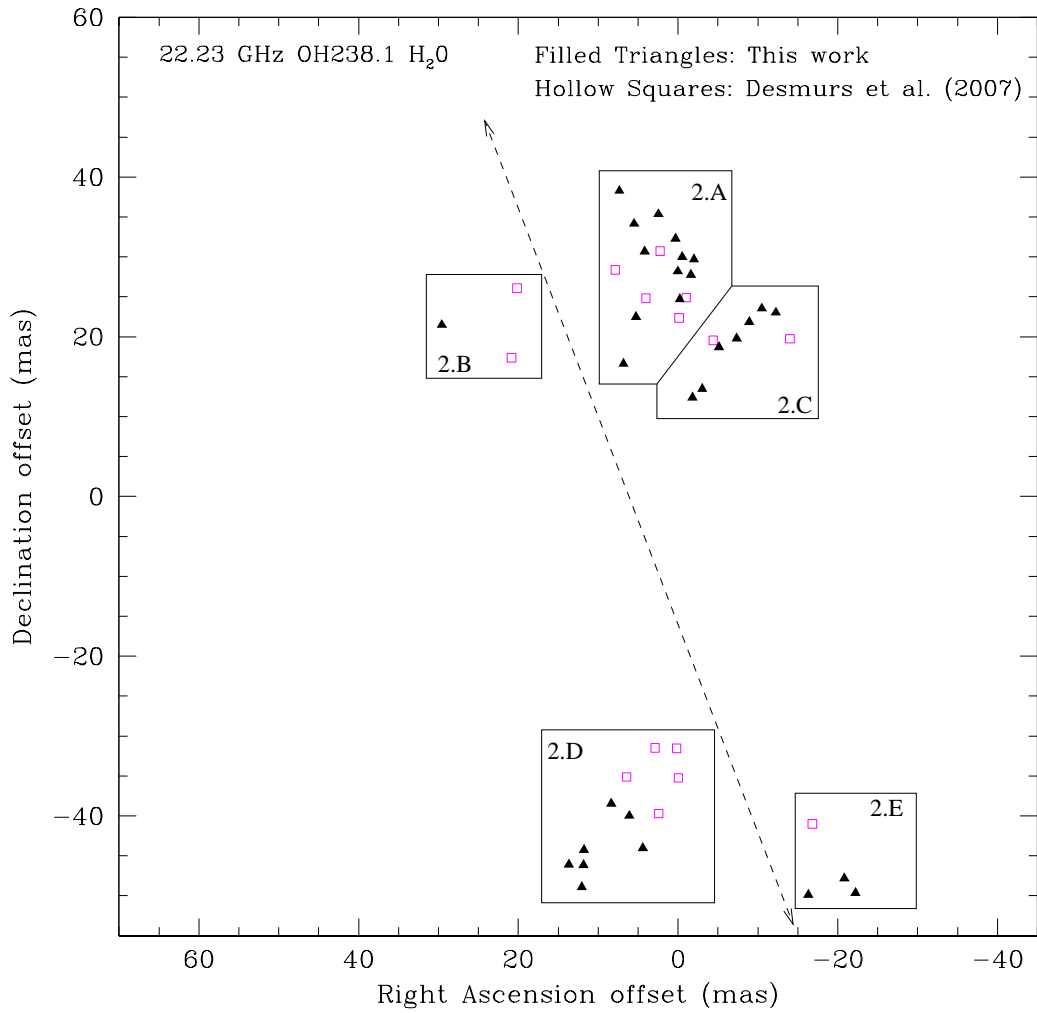


Figure 3.2: Overplot of the maser features observed by D07 and the features presented in the present work. The filled triangles show the 30 features we observed and the hollow squares represent the observations from D07. The dashed vector indicate the direction of the pPN jet.



In the SReg, the distribution of the features we observed is similar to those presented by D07, but appears to have moved away from the origin. Furthermore, we detected 10 features in this region, while D07 detected only six features (considering only regions 2.D and 2.E). The detections in the current observations are spread over a wider East-West area ( $\sim 36$  mas) than that reported by D07 ( $\sim 17$  mas).

The 30 maser features and their properties are listed in Table 3.1.

### 3.3.2 Linear Polarization

We detected linear polarization for three of the 11 maser features in the SReg (S.05, S06 and S07). The degree of polarization and polarization angles of each feature are listed, with their respective errors, in columns 8 and 9 of Table 3.1. Those values correspond to the results given by the brightest channel of each feature. The P error is given by the rms taken from the P image, scaled by the intensity peak. The EVPA error was determined using the expression  $\sigma_{EVPA} = 0.5 \sigma_P/P \times 180^\circ/\pi$  (Wardle & Kronberg 1974).

In Figure 3.1.d, the black lines show the direction of the linear polarization of features S.05, S.06 and S.07. The length of the lines are proportional to the linear polarized intensity of each feature.

In Figure 3.3, for each feature for which linear polarization was detected, we show the polarization vectors across all individual channels. Again the length of the vectors are scaled in proportion to the linearly-polarized intensity.

### 3.3.3 Circular Polarization

The total intensity ( $I$ ) and circular polarization ( $V$ ) spectra of the maser features were used to perform the Zeeman analysis described by Vlemmings et al. (2002). In this approach, the fraction of circular polarization,  $P_V$ , is given by

$$\begin{aligned} P_V &= (V_{max} - V_{min})/I_{max} \\ &= 2 \times A_{F-F'} \times B_{|[Gauss]}/\Delta v_{L[km.s^{-1}]}, \end{aligned} \quad (3.1)$$

Table 3.1: Maser features detected on OH231.8+4.2

Reg	Label	$\Delta\alpha$ (mas)	$\Delta\delta$ (mas)	$I$ (Jy/beam)	$\int I$ (Jy)	$V_{lsr}$ (km/s)	P (%)	EVPA ( $^{\circ}$ )
NReg	N.01	-11.2057	81.4210	0.49	0.81	30.2	-	-
NReg	N.02	+15.8905	67.5530	0.08	0.12	29.4	-	-
NReg	N.03	-13.3862	78.3560	0.24	0.70	29.2	-	-
NReg	N.04	-14.2320	76.0570	0.27	0.32	28.5	-	-
NReg	N.05	-15.2988	73.8400	0.54	1.08	27.4	-	-
NReg	N.06	-6.31373	84.3500	1.67	1.61	27.1	-	-
NReg	N.07	-24.1890	69.6120	0.30	0.46	26.8	-	-
NReg	N.08	-22.6036	67.9370	0.33	1.33	26.7	-	-
NReg	N.09	-16.7119	59.5600	0.26	0.38	26.4	-	-
NReg	N.10	-25.9197	69.1120	0.92	1.72	26.4	-	-
NReg	N.11	-21.0261	65.8640	1.42	2.33	26.4	-	-
NReg	N.12	-8.18628	80.2300	0.72	0.98	26.4	-	-
NReg	N.13	-15.4815	58.4830	0.34	0.60	26.2	-	-
NReg	N.14	-9.49584	76.7490	0.86	1.34	26.1	-	-
NReg	N.15	-18.7994	64.7640	0.49	0.79	26.1	-	-
NReg	N.16	-13.9092	70.7840	16.47	19.24	25.6	-	-
NReg	N.17	-13.6490	74.2530	0.43	0.73	25.4	-	-
NReg	N.18	-6.86105	62.7080	0.09	0.11	24.9	-	-
NReg	N.19	-15.6860	75.7780	0.11	0.13	24.8	-	-
NReg	N.20	-8.41686	68.5520	0.31	0.40	24.6	-	-
SReg	S.01	-9.27134	2.06101	0.08	0.11	44.8	-	-
SReg	S.02	-7.57631	6.09103	0.04	0.04	43.6	-	-
SReg	S.03	-5.31655	7.60502	0.14	0.23	43.3	-	-
SReg	S.04	-1.88907	1.84101	0.16	0.31	43.2	-	-
SReg	S.05	-1.82468	-0.05600	2.55	3.59	42.5	$0.63 \pm 0.13$	$-65 \pm 6$
SReg	S.06	-1.61411	-2.82499	1.35	1.46	41.9	$1.15 \pm 0.24$	$+58 \pm 6$
SReg	S.07	+0.00000	0.00000	5.53	6.77	41.6	$0.28 \pm 0.04$	$-32 \pm 4$
SReg	S.08	-34.4941	-1.73098	0.10	0.14	40.2	-	-
SReg	S.09	-29.9659	-3.77899	0.04	0.05	40.0	-	-
SReg	S.10	-35.9028	-3.57598	0.05	0.07	39.3	-	-

From left to right, the following maser parameters are presented: region of location (Reg); feature label (Label); right ascension offset, in reference to Figure 3.1 ( $\Delta\alpha$ ); declination offset, in reference to Figure 3.1 ( $\Delta\delta$ ); peak intensity ( $I$ ); integrated intensity ( $\int I$ ); radial velocity ( $V_{lsr}$ ); P; EVPA.

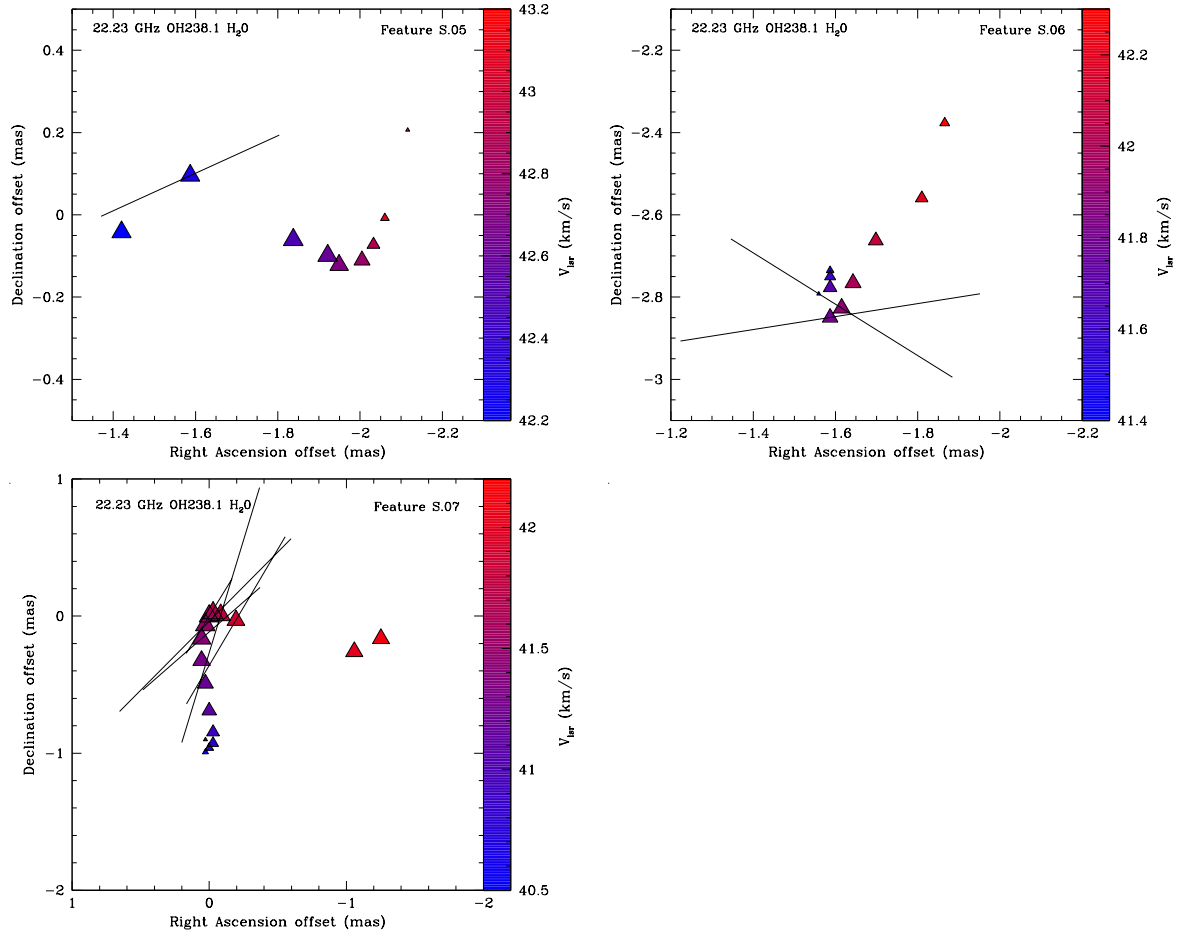


Figure 3.3: Maser spots of the features S.05, S.06 and S.07. The triangle sizes are scaled to the intensity of each spot emission; the color scale shows how the velocity varies at each spot; and the black lines show the direction of linear polarization for those spots that have survived to the polarization threshold cut. The size of the black lines are scaled to the linearly-polarized intensity measured for each spot.

where  $V_{max}$  and  $V_{min}$  are the maximum and minimum of the model fitted to the  $V$  spectrum and  $I_{max}$  is the peak flux of the emission.  $A_{F-F'}$  is the Zeeman splitting coefficient, whose exact value depends on the relative contribution of each hyperfine component of the H<sub>2</sub>O 6<sub>1,6</sub>–5<sub>2,3</sub> rotational maser transition. We adopt the value  $A_{F-F'} = 0.018$ , which is the typical value reported by Vlemmings et al. (2002).  $B_{||[Gauss]}$  is the projected magnetic field strength along the line of sight, and  $\Delta\nu_L$  is the full-width half-maximum of the  $I$  spectrum. Although the non-LTE analysis in Vlemmings et al. (2002) has shown that the circular polarization spectra are not necessarily strictly proportional to  $dI/d\nu$ , using  $A_{F-F'}$  determined by a non-LTE fit introduces a fractional error of less than  $\sim 20\%$  when using Eq. 1. To increase the signal-to-noise ratio of the  $I$  and  $V$  spectra, we smoothed the data by applying a running average over three consecutive channels. We note that the same result, albeit at lower signal-to-noise ratio, was obtained using the non-smoothed spectra.

In Figure 3.4 we show the spectra from Stokes  $I$  and  $V$ , with  $aI$  subtracted. Over-plotted on the  $V$  spectrum (red), we show the model curve that best fits the spectrum (blue). From this model fit, we derive a magnetic field strength of  $B_{||}(\text{NReg}) = 44 \pm 7$  mG and  $B_{||}(\text{SReg}) = -29 \pm 21$  mG. The reported errors are based on the single channel rms using Eq.1, but similar errors were found using a chi-square analysis of the model circular polarization fitted to the smoothed spectra. We also further confirmed the result for both maser features by performing the chi-square analysis on spectra smoothed to different spectral resolutions (up to  $\sim 0.2$  km s<sup>-1</sup>). This leads us to conclude that the detection in the SReg is marginally significant. The flux densities of the other 28 features, however, were not sufficient for a detection of circular polarization.

## 3.4 Discussion

### 3.4.1 Kinematics

Assuming that the maser features observed in this work, at the epoch of March 1<sup>st</sup> 2009, correspond to approximately the same features detected by D07 on November 24<sup>th</sup> 2002, we can estimate the apparent proper motion between both observational

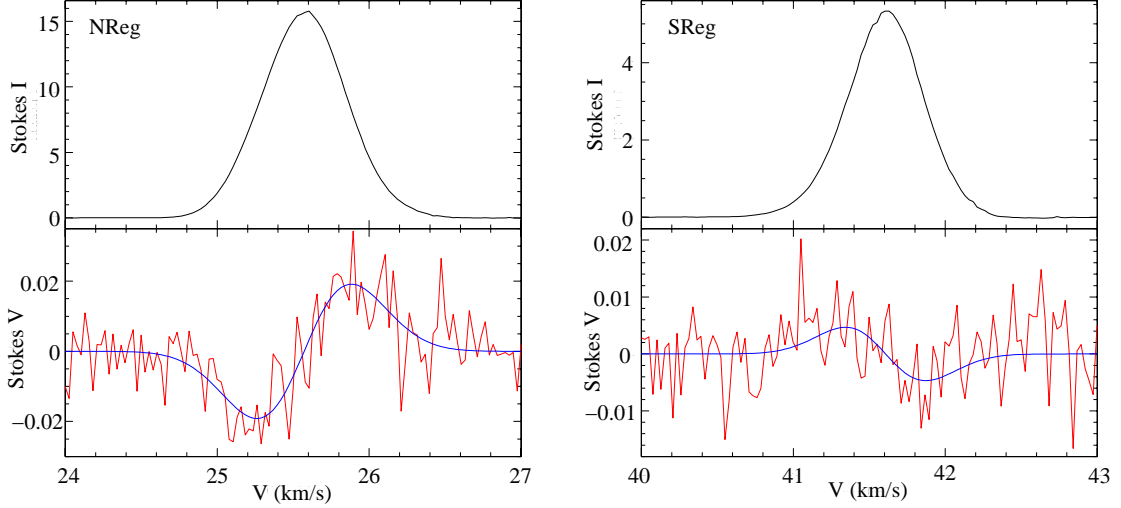


Figure 3.4: Spectra of the Stokes  $I$  (top) and  $V$  (bottom). On the left hand side we present the spectra on the spatial position of the peak emission of the NReg. On the right hand side we show the spectra on the spatial position of the peak emission of the SReg. From the best fit model (blue line) we obtained  $B_{\parallel}(\text{NReg}) = 44 \pm 7$  mG and  $B_{\parallel}(\text{SReg}) = -29 \pm 21$  mG.

epochs. We compared the distance between the mean position of all features located in region 2.A to the mean position of all features located in region 2.D in our data (Figure 3.2), against the distance between the two corresponding points from D07. We present these mean positions and the offsets between the two observational epochs in Table 3.2. The offsets<sup>2</sup> in  $\alpha$  and  $\delta$  give a total offset of 14.4 mas which, at a distance of 1540 pc, corresponds to 22.2 AU. Accordingly, for the time elapsed between the observations (2288 days), the velocity of the separation between the two mean points on the sky is computed to be 2.3 mas/year, or 16 km/s. Assuming the inclination of the bipolar flow is  $i=36^\circ$  (Kastner et al. 1992; Shure et al. 1995), the real separation velocity is  $21 \pm 11$  km/s.

Furthermore, we considered the overall distribution of the maser spots for all features that we observed. In Figure 1.a we show that the spots in the NReg appear

<sup>2</sup>These offsets occur in tangent plane project in the sky. So, strictly, the  $\alpha$  and  $\delta$  listed in Table 3.2 correspond to the coordinate angles of these projections.

Table 3.2: Coordinates of the center (mean) points of the features located in regions 2.A and 2.D, from Figure 3.2; and their offsets between the observations from D07 and ours

Reference	Reg	$\Delta\alpha$ (mas)	$\Delta\delta$ (mas)
Present work	NReg	+2.3	+29.2
Present work	SReg	+9.7	-44.0
D07	NReg	+2.6	+26.2
D07	SReg	+2.4	-34.6
Offset	NReg	-0.3	+2.9
Offset	SReg	+7.4	-9.4
Offset	Total	7.7	12.3

From left to right: Reference, Region (Reg), Offset right ascension ( $\Delta\alpha$ ), Offset in declination ( $\Delta\delta$ ).

to align well with the direction of the nebular jet. The same property is found for the spots from the SReg, as can be seen more clearly in Figure 3.3. In particular, the spots from feature S.07 appear to be closely aligned with the direction of the jet. However, despite being co-linear with the jet, the H<sub>2</sub>O maser outflow velocity is significantly lower than that reported for the jet,  $v_{jet} \sim 330 \text{ km s}^{-1}$  (Sanchez Contreras 1997). Hence, our interpretation is that the masers are being entrained by the jet but are not located in the jet itself. As a consequence, the maser spots have a velocity gradient; with higher velocity further from the origin. The nature of the H<sub>2</sub>O masers in OH231.8+4.2 is thus very different from that of the water fountain sources where the H<sub>2</sub>O masers lie at the tip of their fast bipolar outflows (e.g Imai et al. 2002).

It is important to highlight, however, that a more precise kinematics analysis will require more accurate astrometric observations.

### 3.4.2 Polarization

We detected linear polarization for three H<sub>2</sub>O maser features, all of them located in the SReg (S.05, S.06 and S.07). According to maser polarization theory, the

direction of the linear polarization can be either parallel or perpendicular to the direction of the magnetic field lines. It is parallel when the angle between the magnetic field and the direction of maser propagation ( $\theta$ ) is less than the van Vleck angle ( $\sim 55^\circ$ ), and it is perpendicular when  $\theta$  is greater than this angle (Goldreich et al. 1973). The percentage of linear polarization is affected by  $\theta$  and by the degree of saturation. Based on the level of linear polarization detected ( $\sim 1\%$ ) we cannot conclude definitively in which regime - parallel or perpendicular - the masers of OH231.8+4.2 occur.

The linear polarization angles of the features S.05, S.06 and S.07 display a significant scatter (Fig 3.1.d). The cause of this scatter is not known, but we propose three different scenarios: (i) the scatter could be caused by turbulence, or (ii) in the case of a toroidal magnetic field, the masers could be located at its tangent points; both would explain the different local directions of the field, or (iii) the scatter could be caused by internal Faraday rotation (Faraday 1845). Under the effect of Faraday rotation, the linear polarization angle of the emission ( $\Phi$ ) is rotated by

$$\Phi[^\circ] = 2.02 \times 10^{-2} L[AU] n_e[cm^{-3}] B_{||}[mG] \nu^{-2}[GHz], \quad (3.2)$$

where  $L$  is the path-length of the maser emission through a medium with magnetic field  $B_{||}$  and electron density  $n_e$  at a frequency  $\nu$ . By assuming typical values  $L \sim 10$  AU and  $B_{||} \sim 50$  mG for the H<sub>2</sub>O masers, Eq. 2 becomes:  $\Phi \sim 0.02^\circ \times n_e$ . For the Faraday rotation angle to be of the order of the observed scatter, an electron density of order  $10^3$  is required. For example, if  $n_e \sim 2000$  cm<sup>-3</sup>, then  $\Phi \sim 40^\circ$ . For an electron density of this order at this distance to the central star(s), the fractional ionization would be significantly higher than for a regular evolved star. However, considering the pre-PNe nature of OH231.8+4.2 this cannot be completely ruled out. Still, we consider either scenarios (i) and (ii) more likely than the internal Faraday rotation effect. We note, however, that both scenarios (i) and (ii) differ from the results reported by Etoke et al. (2009) for the OH maser region. The OH masers indicate a uniform field that seems to be flaring out in the same direction of the jet. However, the H<sub>2</sub>O and OH masers occur in very different regions. While the current work finds the H<sub>2</sub>O masers to be located at  $\sim 40$  AU from the CS, the OH masers

are located on a torus with a radius of  $\sim 2$  arcsec (Zijlstra et al. 2001; Etoke et al. 2008). At 1540 pc this correspond to a distance of  $\sim 3100$  AU.

We detected circular polarization for two maser features. Based on these detections, we determined the strength of the magnetic field in each feature to be ( $B_{\parallel}(\text{NReg}) = 44 \pm 7$  mG,  $B_{\parallel}(\text{SReg}) = -29 \pm 21$  mG). If, as argued in Sect. 3.3 that the detection in the SReg is marginally significant, it is evident that the magnetic field in the SReg has an opposite sign compared to the field in the NReg - the positive sign indicates that the direction of the magnetic field is away from the observer, while the negative sign corresponds to a direction toward the observer.

A precise determination of the morphology of the magnetic field is not possible from the current work, as different field morphologies can fit the circular and linear polarization results obtained here. To reach a final conclusion as to the morphology of the magnetic field of OH231.8+4.2 more sensitive polarization information is necessary. If, however, we assume a toroidal<sup>3</sup> magnetic field ( $B \propto r^{-1}$ ), it is possible to extrapolate the field strength to the stellar surface. By taking the separation between the NReg and SReg, and assuming that the CS is located centrally between the two, each H<sub>2</sub>O maser region is at  $\sim 40$  AU from the star. Therefore, from the measured  $B_{\parallel}$  for these regions, the magnetic field strength on the stellar surface (taken to have a radius of  $\sim 1$  AU) must be  $\sim 2.5$  G. This is consistent with the result found for W43A (1.5 G; Vlemmings et al. 2006). This value presents a lower limit if the magnetic field vs. radius relation has a steeper than toroidal dependence.

### 3.5 Conclusions

We detected 30 H<sub>2</sub>O maser features toward OH231.8+4.2. By comparing the current work with the prior observations of Desmurs et al. (2007), we can conclude that the features are moving away from the central star. The average separation velocity of the masers is  $21 \pm 11$  km/s. Furthermore, the masers appear to be dragged in the direction of the collimated outflow. This likely indicates that the masers arise in the turbulent material that is entrained by the jet.

---

<sup>3</sup>Note that solar-type and dipole fields have  $r^{-2}$  and  $r^{-3}$  dependencies, respectively.



We detected linear polarization for three H<sub>2</sub>O maser features. The large scatter in the directions of the linear polarization could be caused by turbulence, or could be due to the masers being located close to the tangent points of a toroidal magnetic field. The possibility of Faraday rotation has also been investigated but, unless the electron density is exceptionally high ( $\gtrsim 2000 \text{ cm}^{-3}$ ), is ruled out.

Based on the detection of circular polarization for two maser features, we determined that the strength of the source magnetic field is  $B_{\parallel}(\text{NReg}) = 44 \pm 7 \text{ mG}$  and  $B_{\parallel}(\text{SReg}) = -29 \pm 21 \text{ mG}$ . The exact morphology of the field in the H<sub>2</sub>O maser region could however not be determined. Assuming a toroidal magnetic field ( $B \propto r^{-1}$ ), the extrapolated magnetic field strength on the stellar surface is  $\sim 2.5 \text{ G}$ .

Our polarization detections, together with the results from Etoke et al. (2009), make pPN OH231.8+4.2 the first evolved star that is known to be a binary and in which the presence of a magnetic field is confirmed throughout the circumstellar envelope. A more comprehensive model of the magnetic field morphology and its potential evolution based on a comparison of the inner and outer wind will require more sensitive observations.



## Chapter 4

# Magnetic fields around evolved stars: Further observations of H<sub>2</sub>O maser polarization

The analysis and results reported in this chapter are published by Leal-Ferreira et al. 2013 (A&A, 554, 134)

*A low- or intermediate-mass star is believed to maintain a spherical shape throughout the evolution from the main sequence to the Asymptotic Giant Branch (AGB) phase. However, many post-AGB objects and planetary nebulae exhibit non-spherical symmetry. Several candidates have been suggested as factors that can play a role in this change of morphology, but the problem is still not well understood. Magnetic fields are one of these possible agents. We aim to detect the magnetic field and infer its properties around four AGB stars using H<sub>2</sub>O maser observations. The sample we observed consists of the following sources: the semi-regular variable RT Vir, and the Mira variables AP Lyn, IK Tau, and IRC+60370. We observed the  $6_{1,6}-5_{2,3}$  H<sub>2</sub>O maser rotational transition in full-polarization mode to determine its linear and circular polarization. Based on the Zeeman effect, one can infer the properties of the magnetic field from the maser polarization analysis. We detected a total of 238 maser features in three of the four observed sources. No masers were found toward AP Lyn. The observed masers are all located between 2.4 and 53.0 AU from the stars. Linear and circular polarization was found in 18 and 11*

*maser features, respectively. We more than doubled the number of AGB stars in which a magnetic field has been detected from H<sub>2</sub>O maser polarization. Our results confirm the presence of fields around IK Tau, RT Vir, and IRC+60370. The strength of the field along the line of sight is found to be between 47 and 331 mG in the H<sub>2</sub>O maser region. Extrapolating this result to the surface of the stars, assuming a toroidal field ( $\propto r^{-1}$ ), we find magnetic fields of 0.3–6.9 G on the stellar surfaces. If, instead of a toroidal field, we assume a poloidal field ( $\propto r^{-2}$ ), then the extrapolated magnetic field strength on the stellar surfaces are in the range between 2.2 and  $\sim 115$  G. Finally, if a dipole field ( $\propto r^{-3}$ ) is assumed, the field strength on the surface of the star is found to be between 15.8 and  $\sim 1945$  G. The magnetic energy of our sources is higher than the thermal and kinetic energy in the H<sub>2</sub>O maser region of this class of objects. This leads us to conclude that, indeed, magnetic fields probably play an important role in shaping the outflows of evolved stars.*

## 4.1 Introduction

Low- and intermediate-mass stars ( $0.8\text{--}8 M_{\odot}$ ) are believed to maintain their sphericity until the asymptotic giant branch (AGB) phase. Even though some AGB stars are slightly elliptical (e.g., Reid & Menten 2007; Castro-Carrizo et al. 2010), many planetary nebulae (PNe) do not present any spherical symmetry. How an almost-spherical AGB star gives rise to a non-spherical PN is still an open question. A companion to the star (binary system or a massive planet), disk interaction, the influence of magnetic fields, or a combination of these agents are candidates to explain this phenomenon (Balick & Frank 2002; Frank et al. 2007; Nordhaus et al. 2007, and references therein).

Magneto-hydrodynamic (MHD) simulations show that the magnetic field can be an important agent in shaping post-AGBs and PNe (e.g., García-Segura et al. 1999, 2005; García-Díaz et al. 2008; Dennis et al. 2009). Moreover, recent observations support the presence of magnetic fields around AGB and post-AGB stars (e.g., Amiri et al. 2011; Pérez-Sánchez et al. 2011; Leal-Ferreira et al. 2012; Vlemmings et al. 2012). However, the sample of low and intermediate mass evolved stars around which magnetic fields have been measured is still small. So far, detections of magnetic

field from H<sub>2</sub>O maser polarization were reported around two AGB stars only; U Her and U Ori (Vlemmings et al. 2002, 2005). Also, the morphology and strength of the magnetic field as a function of radial distance throughout the circumstellar envelope is still unclear. Observations of different magnetic field tracers are needed to constrain the field dependence on the radial distance from the star and, therefore, improve future MHD simulations.

Different maser species can provide information about different regions around these objects. While SiO masers are expected to be found within the extended atmosphere of the star (between the photosphere and the dust formation zone), OH masers are detected much further out ( $\sim 65\text{--}650$  AU). The H<sub>2</sub>O masers emit at an intermediate distance to the star, between the SiO and OH maser regions. The distance of the H<sub>2</sub>O masers from the star is expected to lie within a few to less than a hundred AU (e.g., Cohen 1987; Bowers et al. 1989; Elitzur 1992).

The present work aims to enlarge the number of magnetic field detections around low- and intermediate-mass evolved stars. We imaged five sources of this class using very-long-baseline interferometry (VLBI), in full-polarization mode, with the goal of detecting H<sub>2</sub>O masers around them. As a result of Zeeman splitting (Zeeman 1897), we can measure the magnetic field signature on maser lines by investigating the polarized emission of the masers (e.g., Vlemmings et al. 2001, 2006).

Our sample is composed of the pre-PN OH231.8+4.2, the semi-regular (SR) variable RT Vir, and the Mira variables AP Lyn, IK Tau, and IRC+60370. We presented the results of OH231.8+4.2 in Leal-Ferreira et al. (2012). The analysis of the four remaining sources is presented in the present paper. Single-dish SiO maser observations in full-polarization mode have been previously reported by Herpin et al. (2006) for RT Vir, AP Lyn, and IK Tau. Their results show a magnetic field of  $0 \leq B_{\parallel}[\text{G}] \leq 5.6$  in RT Vir,  $0.9 \leq B_{\parallel}[\text{G}] \leq 5.6$  in AP Lyn, and  $1.9 \leq B_{\parallel}[\text{G}] \leq 6.0$  in IK Tau. The AGB star RT Vir also shows strong circular polarization in single dish OH maser observations, indicating a strong global magnetic field (Szymczak et al. 2001). We did not find any literature reports concerning the magnetic field for IRC+60370 in the SiO maser region, nor for AP Lyn, IK Tau, and IRC+60370 in the OH maser region.

Table 4.1: Low- and high-resolution correlation passes

Label	$N_{chans}$	BW (MHz)	$\Delta v$ (km/s)	PolMode
Low	128	1.0	0.104	Full (LL,RR,LR,RL)
High	512	1.0	0.026	Dual (RR,LL)

Correlation parameters for the low- and high-resolution correlation passes. Description of Cols. 1 to 5: The label of the observed data – low- (Low) and high- (High) resolution – (Label), the number of channels ( $N_{chans}$ ), the bandwidth (BW), the channel width ( $\Delta v$ ), and the polarization mode (PolMode).

This paper is structured as follows: in Sect. 2, we describe the observations, data reduction, and calibration; in Sect. 3, we present the results; in Sect. 4, we discuss the results and, in Sect. 5, we conclude the analysis.

## 4.2 Observations and data reduction

We used the NRAO<sup>1</sup> Very Long Baseline Array (VLBA) to observe the H<sub>2</sub>O  $6_{1,6}-5_{2,3}$  rotational maser transition at a rest frequency toward 22.235081 GHz of the stars in our sample. In each observing run, we used two baseband filters and performed separate lower (Low) and higher (High) resolution correlation passes. The first was performed in full-polarization mode and the second in dual-polarization mode. We show the characteristics of the Low and High correlation passes in Table 4.1 and the individual observation details of each source in Table 4.2.

We observed different calibrators for each target. Each calibrator was observed during the same run as its corresponding target. For the calibration of RT Vir, we used 3C84 (bandpass, delay, polarization leakage, and amplitude). To calibrate IK Tau, we used J0238+16 (bandpass, delay, and amplitude) and 3C84 (polarization leakage). To calibrate IRC+60370, we used BLLAC (bandpass, delay, polarization leakage, polarization absolute angle, and amplitude). Unfortunately, no good ab-

<sup>1</sup>The National Radio Astronomy Observatory (NRAO) is a facility of the National Science Foundation operated under cooperative agreement by Associated Universities, Inc.

Table 4.2: Source observation details

Code	Source	Class	$V_{lsr}$ (IF1) (km/s)	$V_{lsr}$ (IF2) (km/s)	Beam (mas)	RA <sub>0</sub> (J2000)	Dec <sub>0</sub> (J2000)	Date (mm/dd/yy)
BV067A*	OH231.8+4.2	pre-PN	+44.0	+26.0	1.7×0.9	07 <sup>h</sup> 42 <sup>m</sup> 16.93 <sup>s</sup>	-14°42'50".2	03/01/09
BV067B	AP Lyn	Mira variable	-19.5	-32.5	–	06 <sup>h</sup> 34 <sup>m</sup> 34.88 <sup>s</sup>	+60°56'33".2	03/15/09
BV067C	IK Tau	Mira variable	+42.5	+29.5	1.2×0.5	03 <sup>h</sup> 53 <sup>m</sup> 28.84 <sup>s</sup>	+11°24'22".6	02/20/09
BV067D	RT Vir	SR variable	+25.5	+12.5	1.2×0.9	13 <sup>h</sup> 02 <sup>m</sup> 37.98 <sup>s</sup>	+05°11'08".4	03/15/09
BV067E	IRC+60370	Mira variable	-44.5	-57.5	0.8×0.5	22 <sup>h</sup> 49 <sup>m</sup> 58.88 <sup>s</sup>	+60°17'56".7	03/05/09

\*Presented in Leal-Ferreira et al. (2012)

From left to right: The project code (Code), the name of the source (Source), the nature of the source (Class), the velocity center position of each of the 2 filters ( $v_{lsr}$ ), the PSF beam size (Beam), the center coordinates of the observations (RA<sub>0</sub> and Dec<sub>0</sub>), and the starting observation date (Date).

solute polarization angle calibrator were available for RT Vir and IK Tau, making it impossible to determine the absolute direction of the linear polarization vectors (also referred to as electric vector position angle; EVPA). However, the relative EVPA angles for individual polarized components within RT Vir are still correct (no linear polarization was detected for IK Tau). To determine the absolute EVPA of IRC+60370, we created a map of BLLAC and compared the direction of the measured EVPA with that reported in the VLA/VLBA polarization calibration database<sup>2</sup>. Our IRC+60370 observation was carried out between the calibration observations of February 21 and March 19, 2009 in that database, where the polarization angle of BLLAC changed from 25.7° to 26.0°. We thus adopted a reference angle of 25.8° to obtain the absolute EVPA.

After an initial analysis of the raw data, we did not detect any maser emission around AP Lyn and so did not proceed with further calibration of this data set. For the other three targets, we used the Astronomical Image Processing Software Package (AIPS) and followed the data reduction procedure documented by Kembell et al. (1995) to perform all the necessary calibration steps. This included using the AIPS task *SPCAL* to determine polarization leakage parameters using a strong maser feature.

After the data were properly calibrated, we used the low-resolution data to create the image cubes for the Stokes parameters  $I$ ,  $Q$ ,  $U$ , and  $V$ . The  $Q$  and  $U$  cubes were used to generate the linear polarization intensity ( $P = \sqrt{Q^2 + U^2}$ ) cubes and the EVPA cubes. The noise level measured on the emission-free channels of the low-resolution data cubes is between  $\sim 2$  mJy and  $\sim 6$  mJy. The high-resolution data were used to create the data cubes of the Stokes parameters  $I$  and  $V$ , from which the circular polarization could be inferred. The noise level measured from the emission-free channels of the high-resolution data cubes is between  $\sim 5$  mJy and  $\sim 11$  mJy.

The detection of the maser spots was done by using the program *maser finder*, as described by Surcis et al. (2011). We defined a maser feature to be successfully detected when maser spots located at similar spatial positions (within the beam size)

---

<sup>2</sup>[http://www.vla.nrao.edu/astro/calib/polar/2009/K\\_band\\_2009.shtml](http://www.vla.nrao.edu/astro/calib/polar/2009/K_band_2009.shtml)



survive the signal-to-noise ratio cutoff we adopted ( $8\sigma$ ) in at least three consecutive channels. The position of the maser feature was taken to be the position of the maser spot in the channel with the peak emission of the feature (see e.g., Richards et al. 2011).

### 4.3 Results

We found 85 maser features around IK Tau, 91 toward RT Vir, and 62 around IRC+60370. The maser identification and properties are shown in Table 4.7. In Figure 4.1 we show the spatial distribution of the maser components (depicted as circles). The size of the circles is proportional to the maser flux densities, and they are colored according to velocity. The black cross indicates the stellar position determined in Sect. 4.4.3.

Positive linear polarization detection is reported when successfully found in at least two consecutive channels. The linear polarization percentage ( $P_L$ ) quoted in Table 4.7 is the  $P_L$  measured in the brightest channel of the feature. The  $P_L$  error is given by the rms of the  $P$  spectrum on the feature spatial position, scaled by the intensity peak. The  $EVPA$  error was determined using the expression  $\sigma_{EVPA} = 0.5 \sigma_P/P \times 180^\circ/\pi$  (Wardle & Kronberg 1974). The linear polarization results are enumerated in Cols. 8 ( $P_L$ ) and 9 ( $EVPA$ ) of Table 4.7. In Figure 4.1, the black vectors show the  $EVPA$  of the features in which linear polarization is present. The length of the vectors is proportional to the polarization percentage.

To measure the circular polarization, we used the  $I$  and  $V$  spectra to perform the Zeeman analysis described by Vlemmings et al. (2002). In this approach, the fraction of circular polarization,  $P_V$ , is given by

$$\begin{aligned} P_V &= (V_{max} - V_{min})/I_{max} \\ &= 2 \times A_{F-F'} \times B_{||}[\text{Gauss}]/\Delta v_L[\text{km/s}], \end{aligned} \quad (4.1)$$

where  $V_{max}$  and  $V_{min}$  are the maximum and minimum of the model fitted to the  $V$  spectrum, and  $I_{max}$  is the peak flux of the emission. The variable  $A_{F-F'}$  is the Zeeman splitting coefficient. Its exact value depends on the relative contribution

of each hyperfine component of the  $\text{H}_2\text{O}$   $6_{1,6}-5_{2,3}$  rotational maser transition. We adopted the value  $A_{F-F'} = 0.018$ , which is the typical value found by Vlemmings et al. (2002). The projected magnetic field strength along the line of sight is given by  $B_{\parallel}$  and  $\Delta\nu_L$  is the full-width half-maximum of the  $I$  spectrum. Although the non-LTE analysis in Vlemmings et al. (2002) has shown that the circular polarization spectra are not necessarily strictly proportional to  $dI/d\nu$ , using  $A_{F-F'}$ , determined by a non-LTE fit, introduces a fractional error of less than  $\sim 20\%$  when using Eq. 1. We report circular polarization detection when the magnetic field strength given by the model fit is  $\geq 3\sigma$ . The reported errors are based on the single channel rms using Eq. 4.1 (see Leal-Ferreira et al. 2012, Sect. 3.3, for further discussion). We list the  $P_V$  and  $B_{\parallel}$  results in Cols. 10 and 11 of Table 4.7, where the positive sign on  $B_{\parallel}$  indicates that the direction of the magnetic field along the line of sight is away from the observer, while the negative sign corresponds to a direction toward the observer. In Figures 4.2, 4.3, and 4.4, we present the  $I$  and  $V$  spectra and the model fit of  $V$  spectra for those features in which we detect circular polarization.

### 4.3.1 IK Tau

We observed a total of 642  $\text{H}_2\text{O}$  maser spots toward IK Tau. Of these, 525 spots survived the multi-channel criteria and comprise 85 maser features around this source. In Figs. 4.1.I, we present the spatial distribution of these 85 maser features. In Figure 4.1.II and 4.1.III, we zoom in on the two areas indicated in Figure 4.1.I.

We did not find linear polarization in any maser feature around IK Tau. However, circular polarization was detected in three features around this source: IK.20, IK.69, and IK.84 (see Table 4.7). The magnetic field strength along the line of sight given by the model fits are:  $-147 \pm 15$  mG,  $-96 \pm 31$  mG, and  $+215 \pm 56$  mG, respectively. These features are identified in Figure 4.1 labeled according to their field strengths.

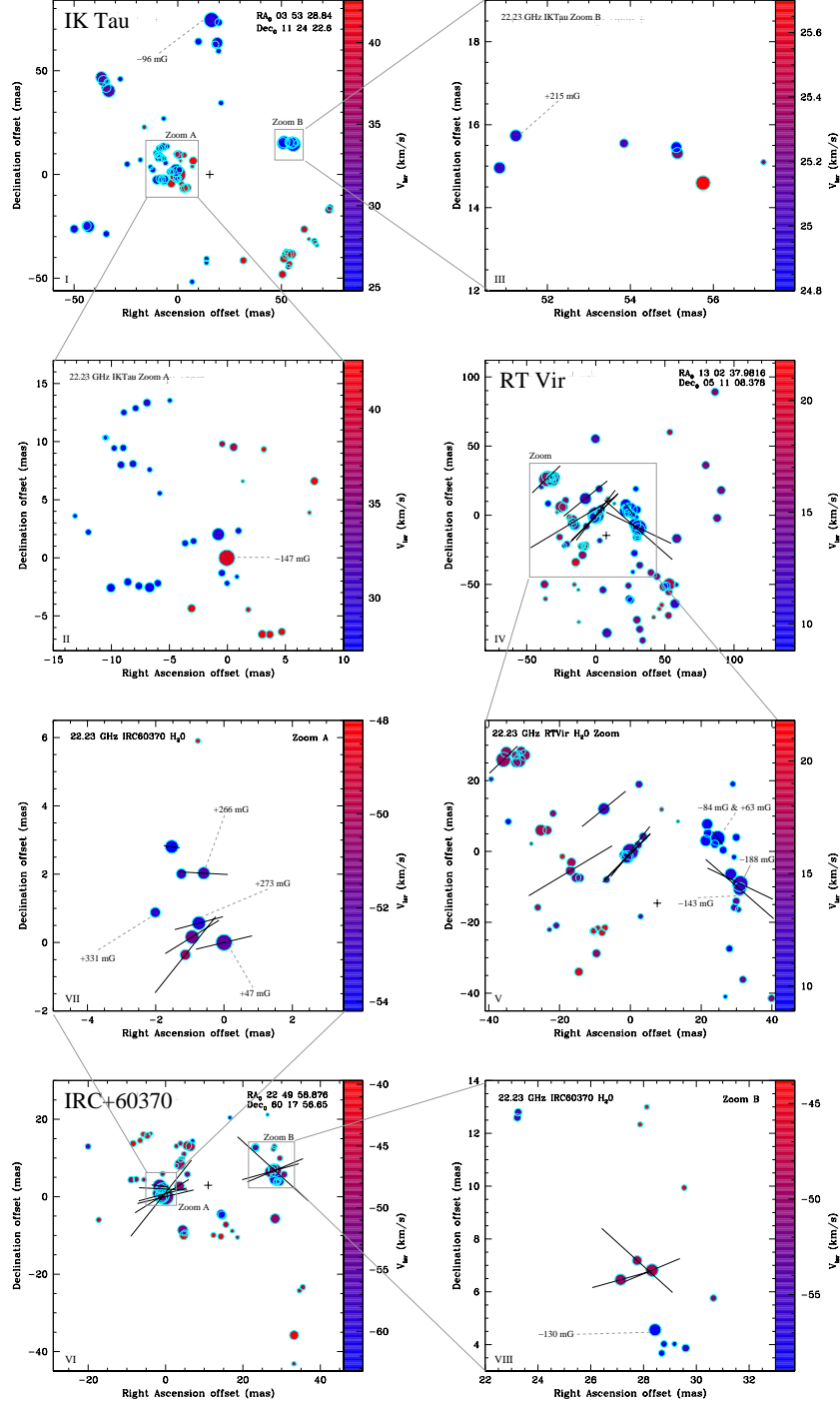


Figure 4.1: Maps of the maser features detected toward RT Vir, IK Tau, and IRC+60370. The size of the circles is proportional to the maser flux densities, and their colors show the velocity scale. The black crosses indicate the stellar positions (see Sect. 4.4.3). The black lines indicate the EVPA (for RT Vir, they could not be calibrated in terms of absolute EVPA), and their lengths are proportional to the fractional linear polarization. The magnetic field strength along the line of sight are also shown for the features in which we detected circular polarization. The x-axis is the projected offset on the plane of the sky in the direction of right ascension. The y-axis is the declination offset. The offsets are with respect to the reference maser.

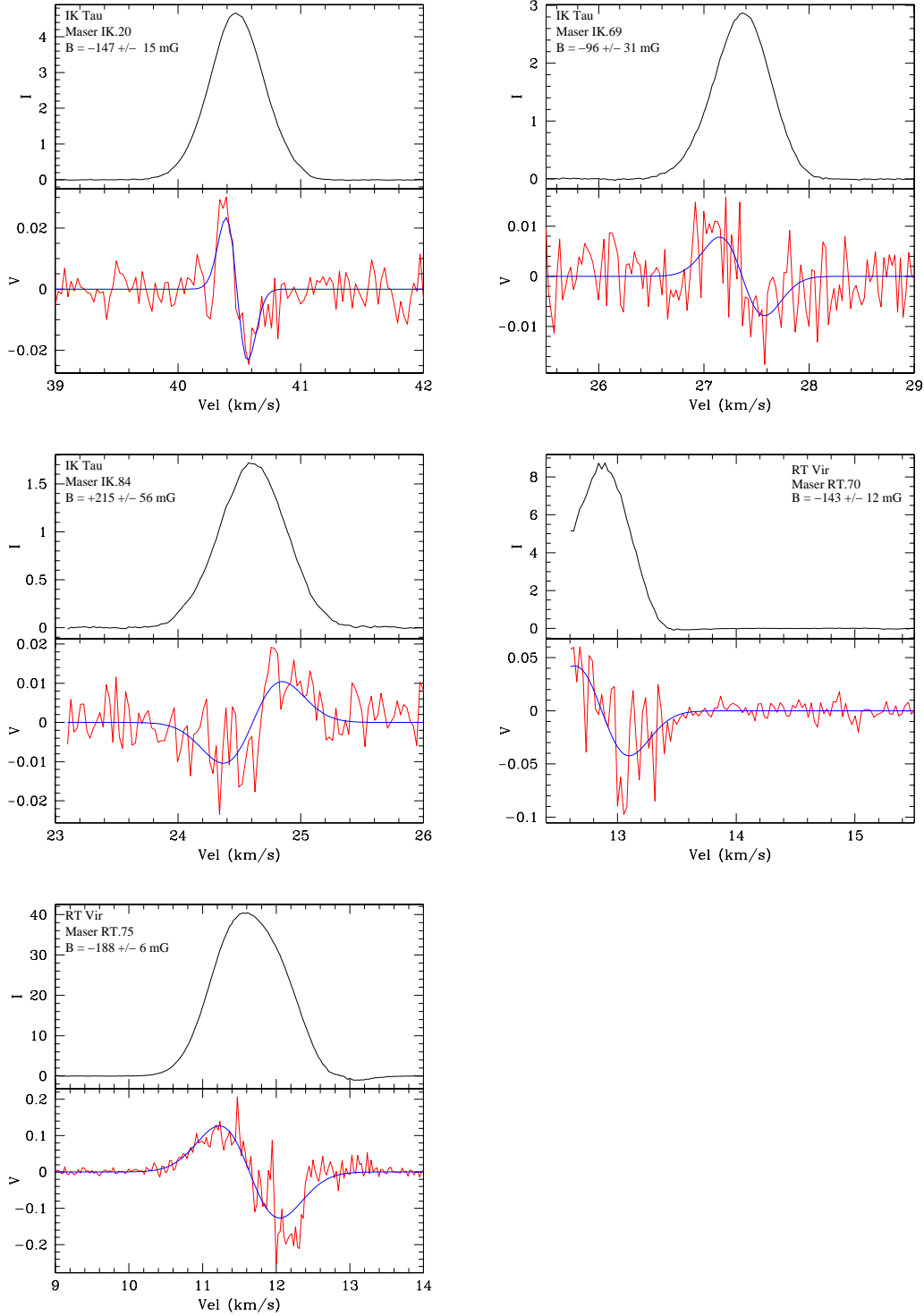


Figure 4.2: Plots of Stokes  $I$  (top; black line) and  $V$  (bottom; red line) spectra of all maser features around IK Tau and RT Vir in which we detected circular polarization. The blue lines show the best model fit to each  $V$  spectrum. The source, the maser identification, and the magnetic field strength along the line of sight given by the fit are presented in top-left corner of each plot. The x-axis shows  $V_{LSR}$  in km/s and the y-axis the intensity in Jy/beam.

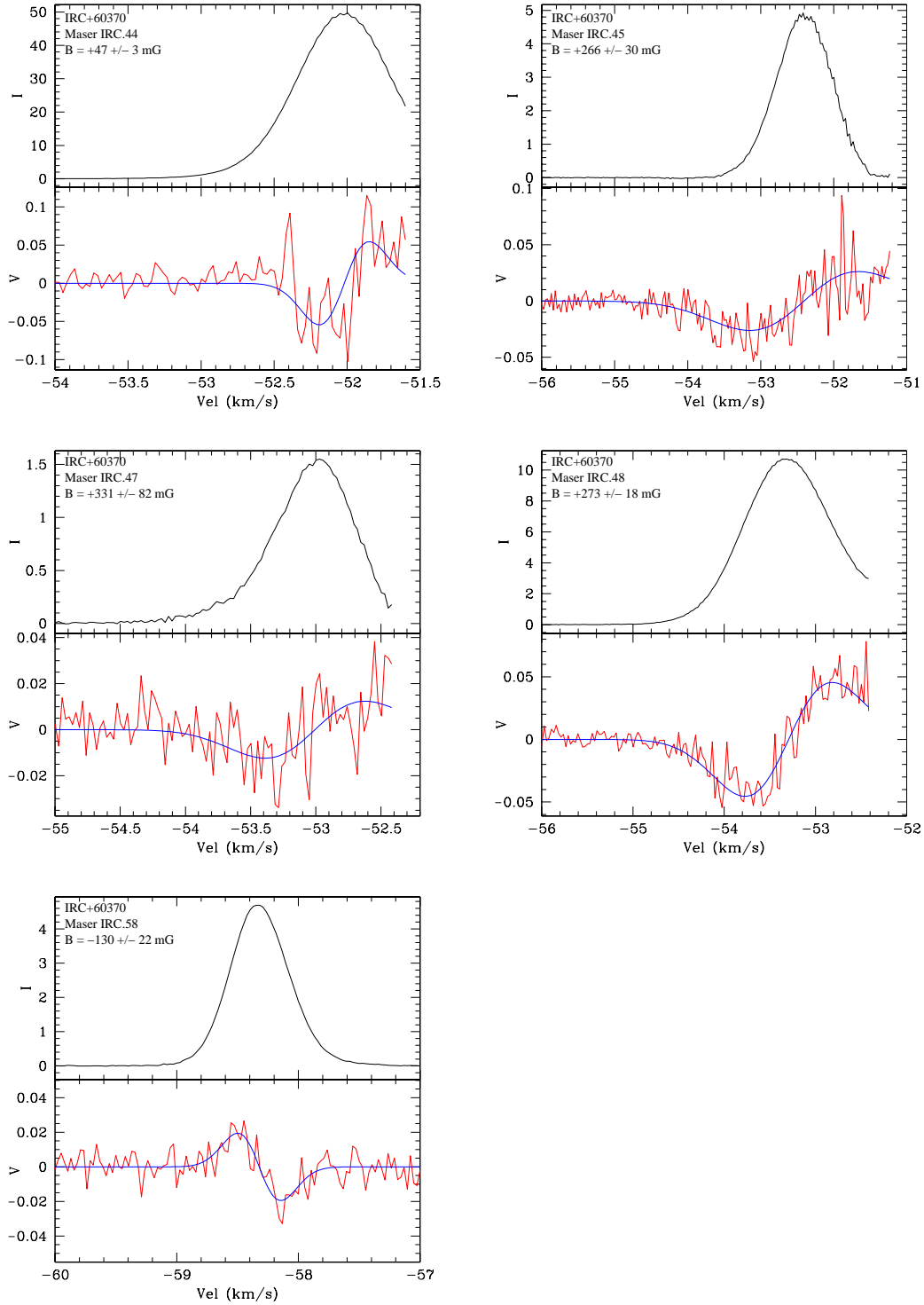


Figure 4.3: Same as Figure 4.2 for the masers around IRC+60370.

### 4.3.2 RT Vir

We observed 830 H<sub>2</sub>O maser spots toward RT Vir in total. Of these, 671 spots comprise 91 maser features around this source. In Figure 4.1.IV, we present the spatial distribution of these 91 maser features and in Figure 4.1.V we show an enlargement of the area indicated in Figure 4.1.IV.

We detected linear polarization in nine features toward RT Vir: RT.31, RT.34, RT.67, RT.68, RT.70, RT.72, RT.73, RT.75, and RT.90 (see Table 4.7). Unfortunately, no good polarization calibrator was available, making it impossible to determine the absolute direction of the polarization vectors (the relative *EVPA* between components is still correct).

The distribution of *EVPA* among the nine features clearly distinguishes two groups of masers. Six features, located within projected right ascension offset  $-40 \lesssim \alpha_{off} \lesssim 0$  mas and declination offset  $-10 \lesssim \delta_{off} \lesssim 30$  mas (Figure 4.1.V) have *EVPA* between  $-38^\circ$  and  $-59^\circ$ . Another group of features, located within  $25 \lesssim \alpha_{off} \lesssim 35$  mas and  $-15 \lesssim \delta_{off} \lesssim 5$  mas (Figure 4.1.V), also has a small *EVPA* dispersion ( $+38^\circ \leq EVPA \leq +64^\circ$ ).

Circular polarization was found in three features around RT Vir: RT.70, RT.75, and RT.90. From the fit of the *V* spectra, we inferred magnetic field strengths along the line of sight of  $-143 \pm 12$  mG and  $-188 \pm 6$  mG in RT.70 and RT.75, respectively. We note, however, that the model fit of RT.70 does not superimpose the whole S-shape structure of its *V* spectrum. This is a consequence of the strong emission that peaks at 11.7 km/s (RT.75). Because of this strong emission, a higher noise is present in the spectra around 11.7 km/s. Therefore, we truncated the RT.70 spectrum at velocity values lower than 12.6 km/s to minimize the impact of this noise on the fit. However, even with this truncation, a high noise is still present in part of the *V* spectrum and so the results from the model fit of RT.70 should be taken with caution.

The shape of the *V* spectrum of RT.90 suggests blended emission. There are many free parameters to be taken into account in fitting emission of blended features. Consequently, any attempt to obtain a magnetic field strength from RT.90 will not generate a solution that is unique or robust. However, it is important to emphasize

that the shape of its  $V$  spectrum clearly indicates the presence of a magnetic field. As an example, we created a possible fit for this feature. The solution we found for this fit gives a magnetic field of  $-84$  mG for the slightly more blue-shifted emission and  $+63$  mG for the slightly more red-shifted feature. The features themselves are separated by approximately  $0.2$  km/s and have widths of  $0.38$  and  $0.4$  km/s. We present this possible fit in Figure 4.4.

In Figure 4.1.V, RT.70, RT.75, and RT.90 are labeled with the magnetic field strength along the line of sight obtained from the model fits shown in Figures 4.2, 4.3, and 4.4.

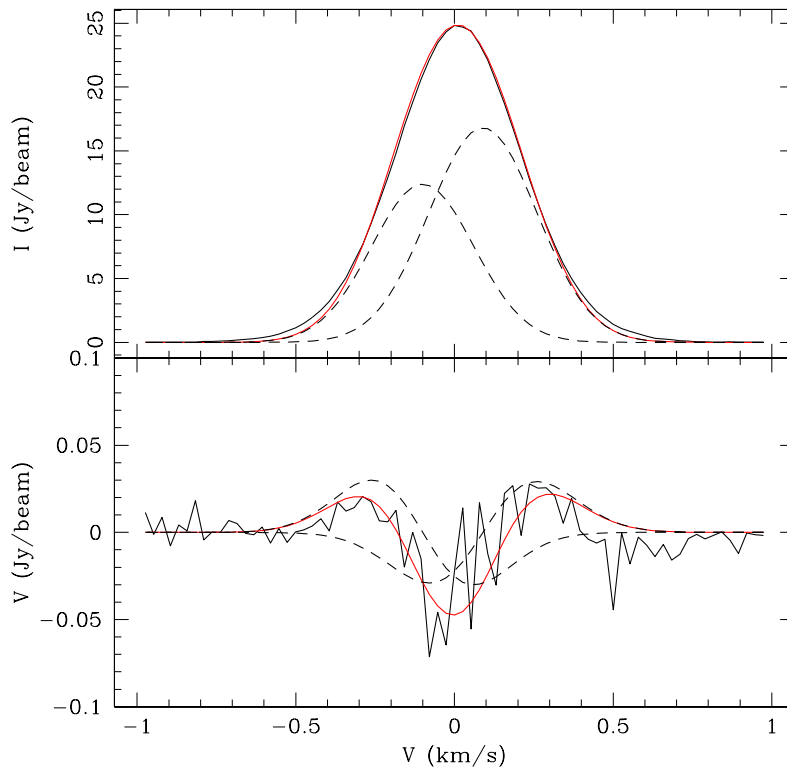


Figure 4.4: Spectra  $I$  and  $V$  (black curves) of RT.90. The dashed lines show the fit of the individual blended features. In red, we show a fit for  $I$  and  $V$ .

### 4.3.3 IRC+60370

We observed 658 H<sub>2</sub>O maser spots in IRC+60370 in total. Of these, 634 spots comprise 62 maser features around this source. In Figure 4.1.VI, we present the spatial distribution of these 62 maser features and in Figure 4.1.VII and 4.1.VIII we show an enlargement of the areas indicated in Figure 4.1.VI.

We detected linear polarization in nine features toward IRC+60370. These nine features are concentrated in two small projected regions, with areas of  $\sim 2$  mas<sup>2</sup> each. Six of them are located within  $-2 \lesssim \alpha_{off} \lesssim 0$  mas and  $-1 \lesssim \delta_{off} \lesssim 3$  mas (Figure 4.1.VII; Zoom A). The other three features with linear polarization detection are located within  $27 \lesssim \alpha_{off} \lesssim 29$  mas and  $6 \lesssim \delta_{off} \lesssim 8$  mas (Figure 4.1.VIII; Zoom B). The EVPA of the masers in Zoom A vary from  $-97^\circ$  to  $-39^\circ$ , while the EVPA of the masers in Zoom B are between  $-74^\circ$  and  $-132^\circ$ .

Circular polarization was found in five features around IRC+60370: IRC.44, IRC.45, IRC.47, IRC.48, and IRC.58. From the model fit to the V spectra, we measured magnetic field strengths along the line of sight of  $+47 \pm 3$  mG,  $+266 \pm 30$  mG,  $+331 \pm 82$  mG,  $+273 \pm 18$  mG, and  $-130 \pm 22$  mG, respectively. We note that, once more, the model fit of several features does not superimpose the full expected S-shape of the V spectra. For this source three factors contributed to this: (i) the limit of the observed spectral range, (ii) features with similar spatial and spectral position, and (iii) the increase in the noise near  $-52$  km/s, due to the strong feature IRC.44. Therefore, the results given by the fit to IRC.44, IRC.45, IRC.47, and IRC.48 should also be taken with caution. In Figure 4.1.VII, the five features with circular polarization detection are labeled with the magnetic field strength along the line of sight that we obtained from the model fits shown in Figures 4.2 and 4.3.

## 4.4 Discussion

### 4.4.1 Non-detection toward AP Lyn

Several H<sub>2</sub>O masers toward AP Lyn have been detected before (e.g., Imai et al. 1997; Migenes et al. 1999; Colomer et al. 2000; Sudou et al. 2002; Shintani et



al. 2008; Kim et al. 2010). Shintani et al. (2008) monitored this and other sources from 2003 to 2006, using the Iriki 20 m telescope of the VLBI Exploration of Radio Astrometry (VERA). They reported a high flux variation, and fit a maser light curve for Ap Lyn. The peak flux of the H<sub>2</sub>O masers reported in the other works vary from  $\sim 6$  Jy (observed with the VLBA in 1996; Migenes et al. 1999) up to  $\sim 120$  Jy (observed with the Kashima-Nobeyama Interferometer in 1992; Sudou et al. 2002). Conservatively, we suggest an upper limit of 1 Jy for the flux density of our non-detection (in the raw data).

Richards et al. (2012) give a detailed discussion of the possible causes of H<sub>2</sub>O maser variability. They point out that a correlation of the infrared light curve and maser variability can exist. Also, they disagree with previous papers (e.g., Shintani et al. 2008) stating that no systematic relationship between maser brightness and the optical phase was found at the times of their observations.

#### 4.4.2 Spatial distribution of the masers

The spatial distribution of the features around IK Tau shows a clear correlation between velocity and position. While masers with higher velocities (red circles) are concentrated in the west and southwest, the features with lower velocity (blue circles) appear, mostly, in the east and northeast (Figure 4.1.I). This behavior is also reported by Bains et al. (2003). They suggest that the shell of IK Tau has an equatorial density enhancement. The brightest masers would lie in an oblate spheroid and the plane of the equator would have an inclination angle  $i'$  with the line of sight ( $45^\circ \lesssim i' \lesssim 90^\circ$ ). The eastern end of the polar axis would then be approaching us, explaining the east-west velocity segregation. This model also explains why the IK Tau observations made more than 10 years apart show a persistent east-west offset between moderately red- and blue-shifted emission, although individual masers do not survive for more than  $\sim 1.5$  years. Our IK Tau data were observed in 2009, almost 15 years later than the observations reported by Bains et al. (2003), and 24 years after the observations reported by Yates & Cohen (1994).

Bains et al. (2003) also observed a similar east-west velocity offset in RT Vir. Our data do not show a clear correlation between velocity and position for this

source (Figure 4.1.I), but a moderate enhanced concentration of red-shifted features in the east is present, while the bluer features are concentrated in the center of the plot. This is different from the east-west relation seen in Figure 6 of Bains et al. (2003). In their figure, the red-shifted masers are located on the western side, and the blue-shifted features are concentrated on the eastern side.

An individual H<sub>2</sub>O maser has its life time estimated to be less than 1–2 years. Multi-epoch imaging of 22 GHz H<sub>2</sub>O masers often shows major changes in the maser distribution over the years (e.g., Richards et al. 2012). IK Tau is, therefore, an exception to this behavior.

### 4.4.3 Stellar Position

Some of the analysis discussed in this paper requires information concerning the stellar position in relation to the observed masers (Sects. 4.4.4 and 4.4.5). However, the absolute stellar position is not known for our observations. So to infer the stellar position, we used the shell-fitting method (Yates 1993; Bains et al. 2003). This method assumes a distribution of masers on a tridimensional sphere, with the star located in its center. All masers in a velocity range determined by

$$V_{star} \pm i(\Delta V_{LSR}/n), \quad (4.2)$$

are identified, where  $V_{star}$  is the velocity of the star,  $\Delta V_{LSR}$  the total maser velocity range, and  $n$  is a number taken here to be equal to 8. We choose that value to restrict the selection of the masers to lie within a small velocity range. The constant  $i$  sets which ring(s) along the line of sight is considered. If  $i$  is equal to 1, then a ring at the same line of sight velocity as the star is taken. If  $i$  is bigger than 1, then one ring in front and one behind of the star are considered. Once the masers are selected, the central position of the features is assumed to be the stellar position. We emphasize that the more asymmetric the maser distribution, the larger the uncertainty of this method.

For each object, we varied the value of  $i$ , obtaining different locations for the stellar position. An additional position was calculated by taking the center point of

Table 4.3: Stellar position

	IK Tau	RT Vir	IRC+60370
	$\alpha, \delta$ (mas)	$\alpha, \delta$ (mas)	$\alpha, \delta$ (mas)
$i=1$	–	$\alpha = +04.51$	$\alpha = +07.44$
	–	$\delta = -13.83$	$\delta = +03.57$
$i=2$	$\alpha = +07.43$	–	$\alpha = +14.49$
	$\delta = +03.09$	–	$\delta = +03.61$
$i=3$	$\alpha = +28.58$	–	$\alpha = +11.17$
	$\delta = -05.38$	–	$\delta = +01.99$
All Features	$\alpha = +10.41$	$\alpha = +10.69$	$\alpha = +10.92$
	$\delta = +02.36$	$\delta = -15.32$	$\delta = +02.68$
Mean Position	$\alpha = +15.47$	$\alpha = +07.60$	$\alpha = +11.01$
	$\delta = +00.02$	$\delta = -14.58$	$\delta = +02.96$

Position of the star, relative to the reference maser, for different values of  $i$ . The positions we obtained as the centroid of all the observed maser features are also shown. Finally, the mean result is reported at the bottom of the table. Columns 2 to 4 show the stellar position of IK Tau, RT Vir, and IRC+60370.

all the observed masers. We assumed the stellar position to be the mean location of the different positions we obtained by using different values of  $i$ , and by using the center point of all the observed masers. In Table 4.3 we show the stellar position we calculated for each value of  $i$  and the mean result.

#### 4.4.4 Distance of the masers to the star

In Figs. 4.5 and 4.6 we show, for each source, a plot of the velocity of the features versus their projected angular offsets from the star ( $\theta_{off}$ ; see Sect. 4.4.3 for the determination of the stellar position). For each source, two parabolas are fitted to the velocity-offset positions. These fits are shown by the dotted lines in the figures. In the fitting process, made by eye, the area between the parabolas which contains all masers is minimized. The parabolas obey the relation

$$\theta_{off} = \frac{R}{V_{shell}} \times (V_{shell}^2 - (V_{LSR} - V_{star})^2)^{1/2}, \quad (4.3)$$

where  $R$  is the distance to the star,  $V_{shell}$  the expanding velocity of the masers, and  $V_{star}$  the velocity of the star.

Assuming that the masers are located in a spherical shell around the star, it is possible to determine the internal ( $R_i$ ) and external ( $R_o$ ) radius of this shell from the internal and external parabola fits, and their corresponding expansion velocities ( $v_i$  and  $v_o$ ). The values we adopted for  $V_{star}$ , the distance to the source, their respective references, and the fit parameters ( $v_i$ ,  $v_o$ ,  $R_i$ ,  $R_o$ ) are shown in Table 4.4.

Bains et al. (2003) and Richards et al. (2011) also investigated the kinematics of IK Tau and RT Vir and found similar results for  $v_i$ ,  $v_o$ ,  $R_i$ , and  $R_o$ . To illustrate the comparison with our results, we reproduce the fits from Bains et al. (2003) for IK Tau and RT Vir in our Figure 4.5. Those authors present two alternative solutions for the internal fit to IK Tau. We choose to show only the one with the larger radius here. Their fits are shown in Figure 4.5 by the dashed lines. We note that there is a big disagreement between the external fits from Bains et al. (2003) and ours. This is probably because our observations with the VLBA resolve out more diffuse emissions, due to its longer baselines. Additionally, our result implies that the H<sub>2</sub>O maser regions around IK Tau and RT Vir reach closer to the star than was determined by Bains et al. (2003). Quantitatively, we found  $R_i$  equal to 38 and 18 mas for IK Tau and RT Vir, respectively. The fits that we reproduced from Bains et al. (2003) correspond to  $R_i$  equal to 60 and 45 mas for IK Tau and RT Vir, respectively. We emphasize, however, that their alternative solution for the internal fit of IK Tau shows an inner radius of the H<sub>2</sub>O maser region closer to the star than ours ( $R_i$  equal to 25 mas). For IK Tau, Richards et al. (2011) found  $R_i$  between 60 and 75 mas for different epochs, but they also detected a faint group of masers with  $R_i$  smaller than 64 mas (at 23 mas). For RT Vir, Richards et al. (2011) found  $R_i$  between 34 and 45 mas for different epochs. Hence, considering the stellar radius of IK Tau and RT Vir to be, respectively, 0.8 AU and 2.8 AU (Monnier et al. 2004; Ragland et al. 2006; Richards et al. 2012), it seems that although the majority of the 22 GHz H<sub>2</sub>O masers occur outside a distance of  $\sim 5$ – $7$  stellar radius, occasional clumps can be found as close as  $\sim 3$  stellar radius.

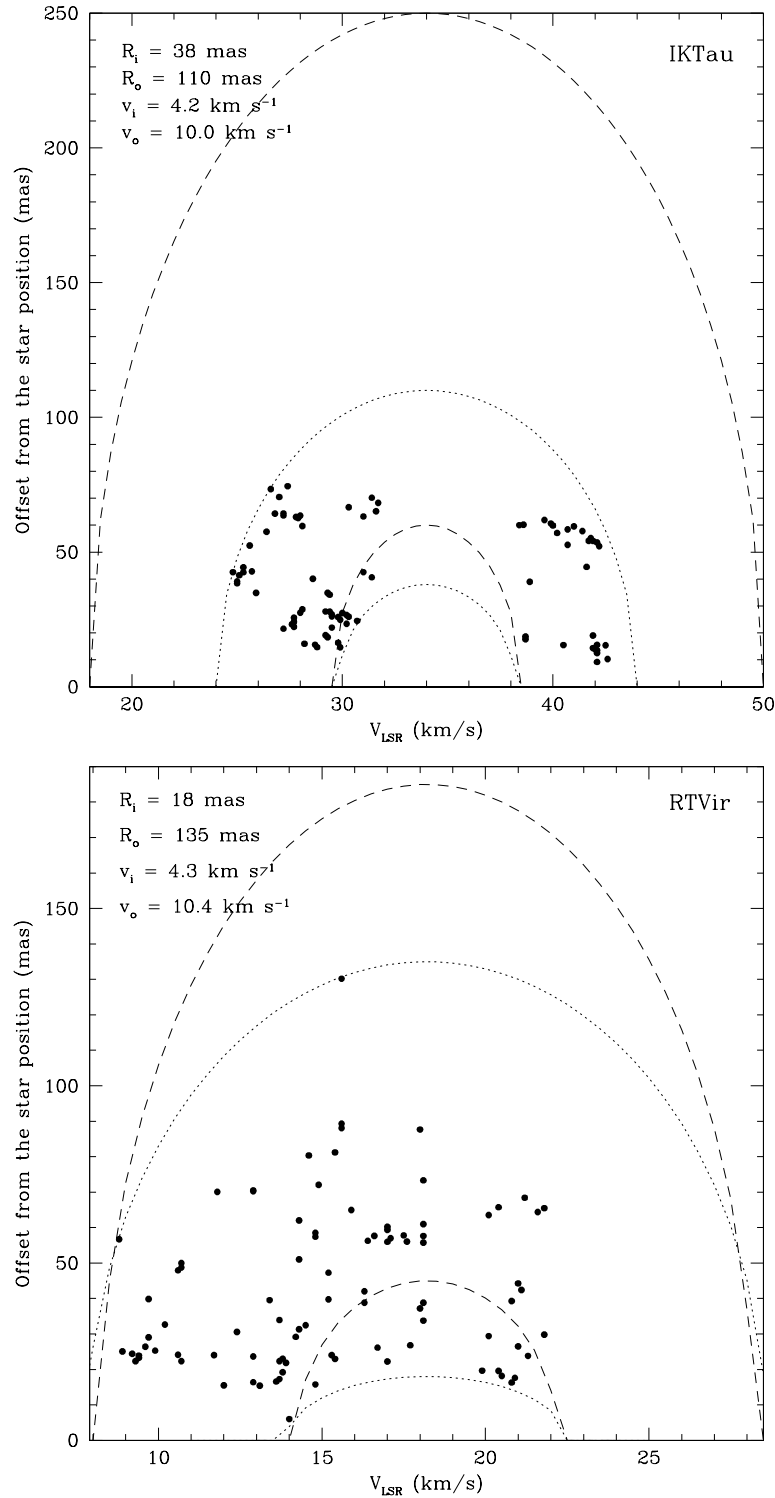


Figure 4.5: Velocity of the features versus their projected offsets from the star. The dotted lines represent our fits; the dashed lines were reproduced from Bains et al. (2003). From top to bottom, we show the plots for IK Tau and RT Vir.

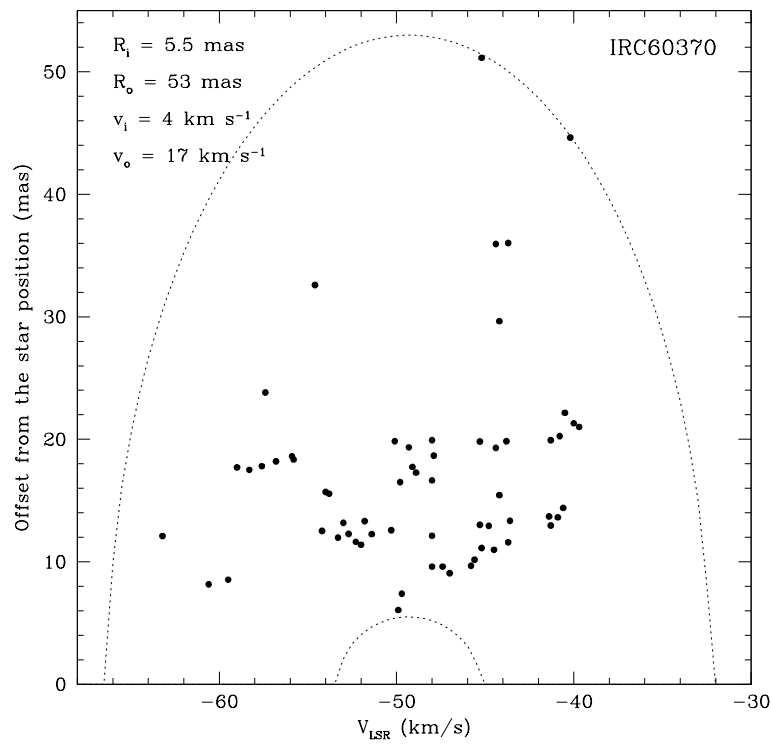


Figure 4.6: Velocity of the features versus their projected offsets from the star. The dotted lines represent our fits. Here we show the plot for IRC+60370.

Table 4.4: Distance of the masers to the star: input and output parameters

Source	$V_{star}$ (ref) (km/s)	$D$ (ref) (pc)	$v_i$ (km/s)	$v_o$ (km/s)	$R_i$ (mas)	$R_o$ (mas)	$R_i$ (AU)	$R_o$ (AU)
IK Tau	+34.0 (K87)	265 (H97)	4.2	10.0	38	110	10.1	29.2
RT Vir	+18.2 (N86)	133 (H97)	4.3	10.4	18	135	2.4	18.0
IRC+60370	-49.3 (I08)	1000 (I08)	4.0	17.0	5.5	53	5.5	53.0

From Cols. 1 to 9: the source name (Source), the velocity of the source and its reference ( $V_{star}$  (ref)), the distance to the source and its reference ( $D$  (ref)), the inner ( $v_i$ ) and outer ( $v_o$ ) expansion velocities of the H<sub>2</sub>O envelope, and the inner ( $R_i$ ) and outer ( $R_o$ ) distances of the H<sub>2</sub>O maser region to the star, both in mas and AU. References: K87: Kirrane (1987); N86: Nyman et al. (1986); I08: Imai et al. (2008); H97: Hipparcos (1997).

### 4.4.5 Magnetic field detection

#### Linear polarization and field geometry

We measured fractional linear polarization from 0.1% to 1.4% around RT Vir, and between 0.2% and 1.6% around IRC+60370. The non-detection of linear polarization in the features around IK Tau imply that, if present, it is lower than  $\sim 0.5\%$  on the brightest masers. These results agree with the upper limits for fractional linear polarization derived from the non-detections of Vlemmings et al. (2002).

According to maser theory, the magnetic field lines can be either parallel or perpendicular to the EVPA. It is parallel when the angle  $\theta$  between the field and the direction of propagation of the maser is less than the Van Vleck angle ( $\sim 55^\circ$ ), and perpendicular when  $\theta$  is greater than the Van Vleck angle (Goldreich et al. 1973). The linear polarization is affected by  $\theta$  and the degree of saturation but, based on our measured values, we cannot ensure in which regime - parallel or perpendicular - the emission originates.

As shown in Sects. 4.3.2 and 4.3.3, linear polarization has been detected in masers toward RT Vir and IRC+60370. In each of these sources, the polarized features are separated into two groups. In RT Vir, both of these groups show a small EVPA dispersion ( $\leq 26^\circ$  for all masers within a given group). If, in this source, we are dealing with a magnetic field perpendicular to the EVPA, either a poloidal or a dipole field seems to be the best qualitative fit of the field geometry to our results. On the other hand, if the field is parallel to the EVPA, the polarization vectors could trace tangent points of a toroidal field. In IRC+60370, the EVPA of the features have a higher dispersion, but the vectors still seem to trace a dominant direction, pointing toward the position of the star, especially in the features located within the Zoom A region. If, in this source, we are dealing with a magnetic field perpendicular to the EVPA, either a poloidal or a dipole field could be argued as probable fits to our results. On the other hand, if the field is parallel to the EVPA, a toroidal field may provide a better qualitative fit. Furthermore, we detected circular polarization in four features located within the Zoom A region and, from the model fit of their V spectra, all of them show a magnetic field strength with a positive sign. Inside the Zoom B region, however, the single feature in which we detected



circular polarization shows a magnetic field strength with a negative sign. These results lead to the conclusion that the component of the magnetic field along the line of sight points in opposite directions on either side of the star. That evidence suggests, again, a toroidal field around IRC+60370.

### Magnetic field dependence

In Figure 4.7, we show a plot of the magnetic field strength along the line of sight for the stars in our sample, estimated from different maser species, against the radial distance of these masers to the star. We use this plot to investigate the field dependence on  $R$ :  $B \propto R^{-\alpha}$ , where  $\alpha$  depends on the structure of the magnetic field in the circumstellar envelope. When  $\alpha$  equal to 1, it refers to a toroidal magnetic field,  $\alpha$  equal to 2 corresponds to a poloidal field, and  $\alpha$  equal to 3 indicates a dipole geometry. In the plot we show one single box where the results of OH masers occur. However, we emphasize that the 1665/7 MHz OH maser emission originates in inner regions when compared to the 1612 MHz OH maser transition. Therefore, it is expected that magnetic field strength measurements based on the first line to be stronger than the second (Wolak et al. 2012).

In this plot, we included polarization results of the SiO maser region from the literature. We took the magnetic field strength in the SiO maser region from Herpin et al. (2006) for RT Vir (upper limit) and IK Tau. For IK Tau, the distance of the SiO region to the star was adapted from Boboltz & Diamond (2005), adopting a distance to the source of 265 pc. For RT Vir, we used a typical value for the radial distance of the SiO maser region (between 2 and 5 AU from the star). Unfortunately, we did not find any reports of the magnetic field strength in the OH maser region that would allow us to make a more complete plot. For all cases, the major uncertainty in the plot concerns  $R$ .

The data from RT Vir and IRC+60370 do not allow a definitive conclusion regarding the functional form of radial dependence. For IK Tau, however, even though a  $B \propto R^{-1}$  dependence is not totally ruled out,  $B \propto R^{-2}$  and  $B \propto R^{-3}$  provide qualitatively better fits.

### Magnetic Field on the Star Surface

By assuming a magnetic field dependence ( $B \propto R^{-1}$ ,  $B \propto R^{-2}$ , or  $B \propto R^{-3}$ ; see previous subsection), we can extrapolate the projected field strength to the surface of the star ( $B_{star}$ ). If  $B \propto R^{-\alpha}$ , then

$$B_{star} = B_{H_2O} \times (R/R_*)^\alpha, \quad (4.4)$$

where  $B_{H_2O}$  is the field strength along the line of sight in the water maser region, and  $R_*$  is the stellar radius (Reid et al. 1979; Reid 1990). However, we emphasize that the magnetic field could deviate from any power law if the various masers come from conditions with different densities, fractional ionization, etc. These differences in the physical conditions of the medium could lead to differences in how much the field is frozen in, dissipated, enhanced by shocks, etc. Therefore, a homogeneous medium is assumed in this extrapolation.

In the analysis with Eq. 4.4 we investigate each source individually, by varying the power law, with  $\alpha$  from 1 to 3. For IK Tau and RT Vir, we adopted  $R_*$  as updated by Richards et al. (2012). For IRC+60370, however, there is no accurate measurement for the stellar radius. Therefore, for this source we adopted  $R_*=1.8$  AU as an upper limit based on 18  $\mu\text{m}$  imaging (Meixner et al. 1999).

In order to define the value of  $R$  to be given as input in Eq. 4.4, for each source we created an alternative plot of velocity versus position offset (analogous to the procedure described in Sect. 4.4.4 and Figs. 4.5 and 4.6). In these alternative plots we considered only the features in which we detected circular polarization, getting alternative values for  $R_i$  and  $R_o$  ( $R'_i$  and  $R'_o$ ). We adopted  $R'_i$  and  $R'_o$  as minimum and maximum values of  $R$  to be given in Eq. 4.4. We emphasize that these alternative plots were created with very few data points, and thus provide only approximate results for  $R'_i$  and  $R'_o$ . We combined  $R = R'_i$  with the lowest value of  $B_{H_2O}$  that we observed (taking the error bar into account –  $B_{H_2O_{min}}$ ) to derive the lower limit of field strength on the surface of the star ( $B_{star_{min}}$ ). For the upper limit ( $B_{star_{max}}$ ), we combined  $R = R'_o$  with the highest value of  $B_{H_2O}$  that we observed (taking the

error bar into account  $- B_{H_2O_{max}}$ ).

In Table 4.6, we show the values given as input in Eq. 4.4 ( $R_*$ ,  $B_{H_2O_{min}}$ ,  $B_{H_2O_{max}}$ ,  $R'_i$ , and  $R'_o$ ), and the results of  $B_{star_{min}}$  and  $B_{star_{max}}$  for each source.

### Magnetic field energy

One question that needs to be answered to improve our understanding on low and intermediate mass stellar evolution is: if present, does the magnetic field around evolved stars have enough energy to drive the shaping of these objects?

Several magnetic field detections around AGB and post-AGB stars have been reported in recent years (e.g., Amiri et al. 2011; Pérez-Sánchez et al. 2011; Leal-Ferreira et al. 2012; Vlemmings et al. 2012). To check if the magnetic energy density ( $U = B^2/2\mu_0$ ) is important, we compare it with typical values of the kinetic and thermal energy density around evolved stars (Table 4.5). For the calculation of these values we assume  $V_{exp} \sim 5$  km/s,  $n_{H_2} \sim 10^{14}$  cm $^{-3}$ , and  $T \sim 2500$  K at the stellar photosphere, and  $V_{exp} \sim 8$  km/s,  $n_{H_2} \sim 10^8$  cm $^{-3}$ , and  $T \sim 500$  K in the H $_2$ O maser region. In Table 4.5, we show the limits of the magnetic energy density in the H $_2$ O maser region that we observed and the magnetic energy density extrapolated to the surface of the star. The limits are based on the field strengths along the line of sight reported in Table 4.6. Our results show that the magnetic energy density is dominant in the H $_2$ O maser region. Therefore, the magnetic fields probably play an important role in shaping the different morphologies of evolved stars that are progenitors of PNe.

The dominant energy on the surface of the star is still inconclusive since different conclusions can be drawn if a dependence of either  $B \propto R^{-1}$ ,  $B \propto R^{-2}$ , or  $B \propto R^{-3}$  is assumed.

## 4.5 Conclusions

We observed four AGB stars in order to detect H $_2$ O maser in full polarization at VLBI resolution. We did not detect any maser emission toward AP Lyn. Toward IK Tau, RT Vir, and IRC+60370 we detected 85, 91, and 62 features, respectively.

Table 4.5: Magnetic energy density

Source	$U_{H_2O}$ (J/m <sup>3</sup> )	$U_{Star} (\alpha=1)$ (J/m <sup>3</sup> )	$U_{Star} (\alpha=2)$ (J/m <sup>3</sup> )	$U_{Star} (\alpha=3)$ (J/m <sup>3</sup> )
IK Tau	-4.8 – -3.5	-3.0 – -1.5	-1.2 – 0.5	0.7 – 2.4
RT Vir	-4.2 – -3.8	-2.4 – -1.3	-0.7 – 1.2	1.1 – 3.7
IRC+60370	-5.1 – -3.2	-3.4 – -0.7	-1.7 – 1.7	0.0 – 4.2
U (J/m <sup>3</sup> )	H <sub>2</sub> O	Star		
$nKT$	~-6.2	~0.5		
$\rho V_{exp}^2$	~-5.1	~0.5		

In the upper part of the table, from Cols. 1 to 4: the source name (Source), the log of the magnetic energy density ( $U = B^2/2\mu_0$ ) in the H<sub>2</sub>O maser region ( $U_{H_2O}$ ), in the stellar surface assuming  $\alpha$  equal to one ( $U_{star} (\alpha=1)$ ), in the stellar surface assuming  $\alpha$  equal to two ( $U_{star} (\alpha=2)$ ), and in the stellar surface assuming  $\alpha$  equal to three ( $U_{star} (\alpha=3)$ ). In the lower part of the table, we show the log of typical values for kinetic and thermal energy densities (Col. 1; Energy density) in the H<sub>2</sub>O maser region (Col. 2; H<sub>2</sub>O) and on the stellar surface (Col. 3; Star).

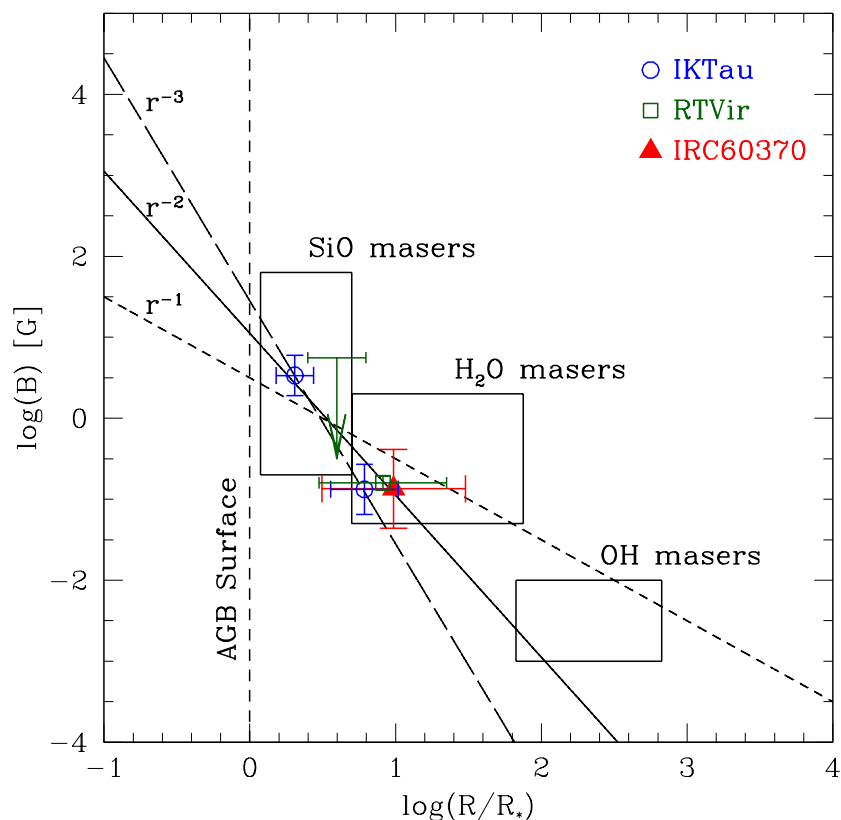


Figure 4.7: Magnetic field strength along the line of sight versus the radial distance of the masers to the star. The black boxes show typical regions of the plot where results from the literature for SiO, H<sub>2</sub>O, and OH maser occur, and they are normalized for  $R_*=1$  (Vlemmings et al. 2002, 2005; Herpin et al. 2006; Rudnitski et al. 2010). Our measurements are shown by the hollow blue circles (IK Tau), hollow green squares (RT Vir), and filled red triangles (IRC+60370). The short-dashed, solid, and long-dashed inclined lines show a dependence  $\propto R^{-1}$ ,  $\propto R^{-2}$ , and  $\propto R^{-3}$  for the magnetic field, respectively. The position of the AGB surface of a star with radius of 1 AU is also shown.

Table 4.6: Projected magnetic field strength on the star surface

Source	$R_*$ (AU)	$B_{H_2O_{min}}$ (mG)	$B_{H_2O_{max}}$ (mG)	$R'_i$ (AU)	$R'_o$ (AU)	$B_{star_{min}}$ (G) ( $\alpha=1$ )	$B_{star_{max}}$ (G) ( $\alpha=1$ )	$B_{star_{min}}$ (G) ( $\alpha=2$ )	$B_{star_{max}}$ (G) ( $\alpha=2$ )	$B_{star_{min}}$ (G) ( $\alpha=3$ )	$B_{star_{max}}$ (G) ( $\alpha=3$ )
IK Tau	2.8	65	271	22.5	27.8	0.5	2.7	4.2	26.8	33.8	$\sim 265$
RT Vir	0.8	131	194	6.0	14.6	1.0	3.5	7.3	64.9	54.9	$\sim 1185$
IRC+60370	1.8	44	413	12.5	29.5	0.3	6.9	2.2	$\sim 115$	15.8	$\sim 1945$

From Cols. 1 to 12: the source name (Source), the stellar radius ( $R_*$ ), the lower ( $B_{H_2O_{min}}$ ) and upper ( $B_{H_2O_{max}}$ ) magnetic field strengths along the line of sight observed in the H<sub>2</sub>O region, the input values of  $R$  on Eq. 4.4 ( $R'_i$  and  $R'_o$ ), and the lower ( $B_{star_{min}}$ ) and upper ( $B_{star_{max}}$ ) limits of the projected magnetic field strength on the stellar surface assuming  $\alpha = 1$ ,  $\alpha = 2$ , and  $\alpha = 3$ .

A structured spatial distribution of maser velocities was observed toward IK Tau. This behavior has already been reported by Bains et al. (2003) and an equatorial density enhancement model was proposed. A similar signature, but less pronounced, was observed toward RT Vir, but with opposite velocity-position pattern to those reported by Bains et al. (2003).

We used the shell-fitting method to infer the projected position of the star relative to the observed masers. With the stellar position determined, we produced a plot of the angular offset of the masers relative to the stellar position versus the maser velocities. We fitted parabolas in these plots to determine the actual distance of the H<sub>2</sub>O maser regions from the central stars. We concluded that the H<sub>2</sub>O masers we observed are located between 10.1 and 29.2 AU from IK Tau, 2.4 and 18.0 AU from RT Vir, and 5.5 and 53.0 AU from IRC+60370.

Linear polarization was observed in 18 features, nine around RT Vir and nine around IRC+60370. Circular polarization was found in 11 features, three around IK Tau, three around RT Vir, and five around IRC+60370. From a model fit of the Stokes V spectra of the features with statistically significant circular polarization detection, we estimated the magnetic field strength along the line of sight needed to generate the observed S-shape profile. The resulting projected magnetic field strengths lie between  $47 \pm 3$  mG and  $331 \pm 82$  mG. With our polarization results, we more than doubled the number of AGB stars around which the magnetic field has been detected in the H<sub>2</sub>O maser region.

Combining our results with published results for the magnetic field measurements in the SiO maser regions, it is not yet possible to determine the magnetic field dependence on the radial distance  $R$  to the star. For IK Tau, either a dependence  $B \propto R^{-2}$  or  $B \propto R^{-3}$  seems qualitatively more likely, but  $B \propto R^{-1}$  is not ruled out. The results we found in the literature for RT Vir and IRC+60370 are not sufficient to draw stronger conclusions.

The results we obtained for the magnetic field strength along the line of sight were extrapolated to the stellar surface of the observed sources, assuming  $B \propto R^{-1}$ ,  $B \propto R^{-2}$ , and  $B \propto R^{-3}$ . In the first case, the projected field strength on the AGB star surface ( $B_{star}$ ) should be between 0.5 G and 2.7 G for IK Tau, 1.0 G and 3.5 G

for RT Vir, and 0.3 G and 6.9 G for IRC+60370. If  $B \propto R^{-2}$  is assumed, then  $B_{star}$  was extrapolated to be between 4.2 G and 26.8 G for IK Tau, 7.3 G and 64.9 G for RT Vir, and 2.2 G and  $\sim 115$  G for IRC+60370. If  $B \propto R^{-3}$ , then  $B_{star}$  was found to be between 33.8 G and  $\sim 265$  G for IK Tau, 54.9 G and  $\sim 1185$  G for RT Vir, and 15.8 G and  $\sim 1945$  G for IRC+60370.

Finally, we compared the magnetic energy density we observed with the typical thermal and kinematic energy density around evolved stars. While the dominant energy density on the surface of the star is still inconclusive, we conclude that, in the H<sub>2</sub>O maser region, the magnetic energy density dominates the thermal and kinematic energy density. Therefore, the magnetic fields cannot be ignored as one of the important agents in shaping planetary nebulae.



Table 4.7: Properties of the observed masers. Respectively, from Cols. 1 to 10: the source in which the maser was observed (Source), the maser identification (feature), projected offset on the plane of sky in direction of right ascension ( $\alpha_{off}$ ), offset in declination ( $\delta_{off}$ ), peak intensity (Peak Int), intensity flux (Int Flux), velocity of the peak ( $V_{peak}$ ),  $P_V$ , magnetic field strength ( $B \cos\theta$ ), and if linear polarization was detected or not (LinPol).  $\alpha_{off}$  and  $\delta_{off}$  are with respect to the reference feature.

Source	Feature	$\alpha_{off}$ (mas)	$\delta_{off}$ (mas)	Peak Int (Jy/Beam)	Int Flux (Jy)	$V_{peak}$ (km/s)	$P_L$ (%)	EVPA ( $^\circ$ )	$P_V$ ( $\times 10^{-3}$ )	$B_{  }$ (mG)
AP Lyn	–	–	–	–	–	–	–	–	–	–
IK Tau	IK.01	7.5	6.6	0.20	0.35	42.6	–	–	–	–
	IK.02	3.2	9.3	0.08	0.15	42.5	–	–	–	–
	IK.03	52.3	–37.0	0.06	0.18	42.2	–	–	–	–
	IK.04	52.6	–38.6	0.33	0.54	42.1	–	–	–	–
	IK.05	3.6	–6.6	0.20	0.41	42.1	–	–	–	–
	IK.06	4.7	–6.4	0.17	0.54	42.1	–	–	–	–
	IK.07	7.1	3.9	0.04	0.09	42.1	–	–	–	–
	IK.08	1.3	6.6	0.03	0.05	42.1	–	–	–	–
	IK.09	3.0	–6.6	0.24	0.52	42.0	–	–	–	–
	IK.10	53.7	–38.3	0.30	0.53	41.9	–	–	–	–
	IK.11	1.8	–4.5	0.08	0.13	41.9	–	–	–	–
	IK.12	–3.1	–4.4	0.22	0.50	41.9	–	–	–	–
	IK.13	55.0	–38.5	0.27	0.87	41.8	–	–	–	–
	IK.14	51.3	–40.6	0.21	0.37	41.7	–	–	–	–
	IK.15	31.7	–41.4	0.14	0.25	41.6	–	–	–	–
	IK.16	53.8	–43.2	0.12	0.20	41.4	–	–	–	–
	IK.17	50.5	–48.1	0.18	0.30	41.0	–	–	–	–
	IK.18	53.3	–44.5	0.07	0.10	40.7	–	–	–	–
	IK.19	61.1	–26.4	0.15	0.31	40.7	–	–	–	–
	IK.20	–0.0	0.0	4.93	10.22	40.5	–	–	10.08 $\pm$ 1.03	–147 $\pm$ 15
	IK.21	63.3	–31.1	0.04	0.06	40.2	–	–	–	–
	IK.22	66.0	–32.1	0.07	0.17	40.0	–	–	–	–
	IK.23	66.4	–32.9	0.06	0.14	39.9	–	–	–	–
	IK.24	67.2	–34.1	0.04	0.07	39.6	–	–	–	–
	IK.25	–16.1	22.8	0.06	0.14	38.9	–	–	–	–

Table 4.7: continued.

Source	Feature	$\alpha_{off}$ (mas)	$\delta_{off}$ (mas)	Peak Int (Jy/Beam)	Int Flux (Jy)	$V_{peak}$ (km/s)	$P_L$ (%)	EVPA ( $^\circ$ )	$P_V$ ( $\times 10^{-3}$ )	$B_{  [Gauss]}$ (mG)
IK Tau	IK.26	0.5	9.5	0.21	0.42	38.7	–	–	–	–
	IK.27	–0.4	9.8	0.11	0.26	38.7	–	–	–	–
	IK.28	73.5	–16.0	0.11	0.28	38.6	–	–	–	–
	IK.29	73.0	–17.0	0.17	0.92	38.4	–	–	–	–
	IK.30	–35.8	45.1	0.61	1.06	31.7	–	–	–	–
	IK.31	–34.5	41.9	0.34	0.77	31.6	–	–	–	–
	IK.32	–36.8	46.9	0.75	1.44	31.4	–	–	–	–
	IK.33	13.9	–40.6	0.07	0.18	31.4	–	–	–	–
	IK.34	–33.3	40.3	1.33	2.54	31.0	–	–	–	–
	IK.35	13.9	–42.5	0.06	0.13	31.0	–	–	–	–
	IK.36	–5.0	13.5	0.06	0.10	30.7	–	–	–	–
	IK.37	–6.9	13.3	0.19	0.59	30.3	–	–	–	–
	IK.38	–34.1	44.7	0.08	0.15	30.3	–	–	–	–
	IK.39	–7.9	12.9	0.12	0.45	30.2	–	–	–	–
	IK.40	–6.7	7.6	0.07	0.15	30.2	–	–	–	–
	IK.41	–8.9	12.5	0.11	0.24	30.0	–	–	–	–
	IK.42	–8.1	8.1	0.17	0.57	29.9	–	–	–	–
	IK.43	1.0	2.3	0.12	0.31	29.9	–	–	–	–
	IK.44	–0.8	2.0	1.11	3.12	29.8	–	–	–	–
	IK.45	–9.2	8.0	0.17	0.49	29.8	–	–	–	–
	IK.46	–5.8	5.6	0.07	0.12	29.5	–	–	–	–
	IK.47	–9.0	9.5	0.13	0.29	29.5	–	–	–	–
	IK.48	–9.8	9.4	0.10	0.22	29.5	–	–	–	–
	IK.49	–18.0	7.0	0.06	0.10	29.4	–	–	–	–
	IK.50	–10.5	10.4	0.08	0.19	29.4	–	–	–	–
	IK.51	–2.9	1.4	0.12	0.28	29.3	–	–	–	–
IK.52	–6.7	26.9	0.06	0.11	29.3	–	–	–	–	
IK.53	–3.7	1.3	0.13	0.26	29.2	–	–	–	–	
IK.54	–10.6	10.3	0.07	0.18	29.2	–	–	–	–	
IK.55	0.8	–1.6	0.05	0.10	28.8	–	–	–	–	
IK.56	–0.0	–2.2	0.09	0.51	28.7	–	–	–	–	

Table 4.7: continued.

Source	Feature	$\alpha_{off}$ (mas)	$\delta_{off}$ (mas)	Peak Int (Jy/Beam)	Int Flux (Jy)	$V_{peak}$ (km/s)	$P_L$ (%)	EVPA ( $^\circ$ )	$P_V$ ( $\times 10^{-3}$ )	$B_{  [Gauss]}$ (mG)
IK Tau	IK.57	-24.3	5.0	0.09	0.20	28.6	-	-	-	-
	IK.58	-0.5	-1.3	0.15	0.28	28.2	-	-	-	-
	IK.59	19.7	59.5	0.08	0.15	28.1	-	-	-	-
	IK.60	-13.1	3.6	0.06	0.11	28.1	-	-	-	-
	IK.61	19.1	63.5	0.60	1.11	28.0	-	-	-	-
	IK.62	-12.0	2.2	0.10	0.21	28.0	-	-	-	-
	IK.63	18.1	62.6	0.14	0.21	27.9	-	-	-	-
	IK.64	-27.6	46.0	0.08	0.14	27.8	-	-	-	-
	IK.65	-6.7	-2.6	0.45	1.14	27.7	-	-	-	-
	IK.66	-10.0	-2.6	0.29	0.88	27.7	-	-	-	-
	IK.67	-8.6	-2.1	0.20	0.56	27.7	-	-	-	-
	IK.68	-7.7	-2.4	0.18	0.60	27.6	-	-	-	-
	IK.69	16.4	74.5	2.97	4.28	27.4	-	-	5.48 $\pm$ 1.78	-96 $\pm$ 31
	IK.70	-43.0	-25.1	0.81	1.66	27.2	-	-	-	-
	IK.71	-44.0	-24.8	0.32	0.88	27.2	-	-	-	-
	IK.72	-6.0	-2.2	0.16	0.35	27.2	-	-	-	-
	IK.73	-49.9	-26.3	0.23	0.53	27.0	-	-	-	-
	IK.74	10.0	64.1	0.15	0.19	26.8	-	-	-	-
	IK.75	19.7	73.3	0.17	0.27	26.6	-	-	-	-
	IK.76	-34.4	-28.6	0.12	0.17	26.4	-	-	-	-
	IK.77	20.9	34.5	0.08	0.13	25.9	-	-	-	-
	IK.78	55.8	14.6	2.37	4.67	25.7	-	-	-	-
	IK.79	6.9	-51.7	0.07	0.15	25.6	-	-	-	-
	IK.80	57.2	15.1	0.08	0.14	25.3	-	-	-	-
	IK.81	55.1	15.3	0.78	1.96	25.3	-	-	-	-
IK.82	53.8	15.6	0.30	0.88	25.1	-	-	-	-	
IK.83	50.8	15.0	0.86	2.50	25.0	-	-	-	-	
IK.84	51.2	15.7	0.90	2.18	25.0	-	-	12.15 $\pm$ 3.14	+215 $\pm$ 56	
IK.85	55.1	15.5	0.59	1.29	24.8	-	-	-	-	
RT Vir	RT.01	-19.3	-1.4	0.14	0.16	21.8	-	-	-	-
	RT.02	45.9	-67.7	0.07	0.16	21.8	-	-	-	-

Table 4.7: continued.

Source	Feature	$\alpha_{off}$ (mas)	$\delta_{off}$ (mas)	Peak Int (Jy/Beam)	Int Flux (Jy)	$V_{peak}$ (km/s)	$P_L$ (%)	EVPA ( $^\circ$ )	$P_V$ ( $\times 10^{-3}$ )	$B_{  [Gauss]}$ (mG)
RT Vir	RT.03	47.6	-64.9	0.09	0.13	21.6	-	-	-	-
	RT.04	13.4	8.5	0.03	0.04	21.3	-	-	-	-
	RT.05	41.8	-73.8	0.05	0.10	21.2	-	-	-	-
	RT.06	-15.6	-50.1	0.06	0.07	21.1	-	-	-	-
	RT.07	8.8	11.9	0.06	0.08	21.0	-	-	-	-
	RT.08	-12.7	-54.0	0.03	0.04	21.0	-	-	-	-
	RT.09	-8.1	-22.9	0.29	0.42	20.9	-	-	-	-
	RT.10	-7.2	-21.5	0.22	0.30	20.8	-	-	-	-
	RT.11	-28.0	2.2	0.04	0.06	20.8	-	-	-	-
	RT.12	-9.2	-21.6	0.12	0.21	20.5	-	-	-	-
	RT.13	-10.4	-22.4	0.26	0.37	20.4	-	-	-	-
	RT.14	-12.4	-77.2	0.04	0.09	20.4	-	-	-	-
	RT.15	-14.5	-34.0	0.64	1.44	20.1	-	-	-	-
	RT.16	-36.4	-60.4	0.07	0.09	20.1	-	-	-	-
	RT.17	-10.5	-22.4	0.21	0.29	19.9	-	-	-	-
	RT.18	52.6	-72.5	0.29	0.40	18.1	-	-	-	-
	RT.19	52.8	-55.5	0.33	0.61	18.1	-	-	-	-
	RT.20	49.1	-51.8	0.74	1.13	18.1	-	-	-	-
	RT.21	53.1	-49.9	4.65	5.42	18.1	-	-	-	-
	RT.22	-26.1	-15.8	0.25	0.40	18.1	-	-	-	-
	RT.23	-25.3	6.0	3.13	5.03	18.1	-	-	-	-
	RT.24	-23.5	6.0	0.77	0.99	18.0	-	-	-	-
	RT.25	53.5	60.1	0.18	0.34	18.0	-	-	-	-
	RT.26	-16.7	-3.1	0.90	0.97	17.7	-	-	-	-
	RT.27	-29.8	27.2	2.34	3.73	17.6	-	-	-	-
	RT.28	-32.4	27.1	0.62	0.66	17.5	-	-	-	-
	RT.29	-37.1	-50.0	0.56	0.72	17.1	-	-	-	-
	RT.30	-31.4	25.6	7.83	9.24	17.0	-	-	-	-
	RT.31	-35.8	25.9	20.96	25.07	17.0	0.22 $\pm$ 0.02	-46 $\pm$ 5	-	-
	RT.32	-35.0	28.0	2.83	3.55	17.0	-	-	-	-
	RT.33	-9.6	-28.8	0.60	0.90	17.0	-	-	-	-

Table 4.7: continued.

Source	Feature	$\alpha_{off}$ (mas)	$\delta_{off}$ (mas)	Peak Int (Jy/Beam)	Int Flux (Jy)	$V_{peak}$ (km/s)	$P_L$ (%)	EVPA ( $^\circ$ )	$P_V$ ( $\times 10^{-3}$ )	$B_{  [Gauss]}$ (mG)
RT Vir	RT.34	-17.0	-5.4	1.21	1.38	16.7	1.41 $\pm$ 0.04	-59 $\pm$ 3	-	-
	RT.35	-30.8	28.4	0.79	0.86	16.6	-	-	-	-
	RT.36	-32.3	25.1	1.32	3.13	16.4	-	-	-	-
	RT.37	39.8	-41.5	0.32	0.51	16.3	-	-	-	-
	RT.38	-21.8	10.7	0.28	0.35	16.3	-	-	-	-
	RT.39	29.7	-75.6	0.48	0.75	15.9	-	-	-	-
	RT.40	90.7	18.0	0.68	1.08	15.6	-	-	-	-
	RT.41	79.5	36.2	0.48	0.89	15.6	-	-	-	-
	RT.42	86.2	89.1	0.44	0.54	15.6	-	-	-	-
	RT.43	-14.3	-7.5	0.59	1.58	15.4	-	-	-	-
	RT.44	87.8	-2.1	0.64	1.21	15.4	-	-	-	-
	RT.45	-15.4	-7.4	1.15	1.62	15.3	-	-	-	-
	RT.46	23.6	-51.0	0.22	0.48	15.2	-	-	-	-
	RT.47	44.3	-44.3	0.28	0.36	15.2	-	-	-	-
	RT.48	31.7	-82.4	0.39	0.59	14.9	-	-	-	-
	RT.49	-6.7	-8.0	0.26	0.56	14.8	-	-	-	-
	RT.50	-31.3	27.6	0.12	0.12	14.8	-	-	-	-
	RT.51	-39.3	20.4	0.10	0.13	14.8	-	-	-	-
	RT.52	33.9	-90.5	0.25	0.36	14.6	-	-	-	-
	RT.53	31.8	-36.2	0.32	0.35	14.5	-	-	-	-
	RT.54	58.5	-16.8	1.20	1.33	14.3	-	-	-	-
	RT.55	58.2	-50.3	0.08	0.11	14.3	-	-	-	-
	RT.56	-22.9	-22.1	0.08	0.18	14.3	-	-	-	-
	RT.57	-20.9	-20.9	0.23	0.41	14.2	-	-	-	-
	RT.58	2.8	-18.3	0.13	0.15	14.0	-	-	-	-
	RT.59	29.4	-15.8	0.34	0.46	13.9	-	-	-	-
	RT.60	3.6	4.2	0.58	0.97	13.8	-	-	-	-
	RT.61	30.6	-16.4	0.15	0.20	13.8	-	-	-	-
	RT.62	29.9	-14.0	0.35	0.39	13.7	-	-	-	-
	RT.63	2.2	1.8	0.42	0.48	13.7	-	-	-	-
	RT.64	2.4	19.0	0.36	0.40	13.7	-	-	-	-

Table 4.7: continued.

Source	Feature	$\alpha_{off}$ (mas)	$\delta_{off}$ (mas)	Peak Int (Jy/Beam)	Int Flux (Jy)	$V_{peak}$ (km/s)	$P_L$ (%)	EVPA ( $^\circ$ )	$P_V$ ( $\times 10^{-3}$ )	$B_{  [Gauss]}$ (mG)
RT Vir	RT.65	-1.9	-1.0	0.57	0.71	13.6	-	-	-	-
	RT.66	5.2	-54.0	0.36	0.49	13.4	-	-	-	-
	RT.67	-1.0	-1.8	2.08	2.71	13.1	$0.56\pm 0.26$	$-44\pm 16$	-	-
	RT.68	0.0	0.0	54.53	63.13	12.9	$0.48\pm 0.19$	$-38\pm 12$	-	-
	RT.69	8.0	-85.1	1.30	1.60	12.9	-	-	-	-
	RT.70	30.9	-10.6	7.92	8.45	12.9	$1.12\pm 0.28$	$+49\pm 26$	$10.50\pm 0.86$	$-143\pm 12^e$
	RT.71	-0.3	55.2	0.93	1.29	12.9	-	-	-	-
	RT.72	-7.5	12.0	4.23	5.28	12.4	$0.38\pm 0.29$	$-51\pm 41$	-	-
	RT.73	-0.9	-1.6	6.94	7.53	12.0	$0.49\pm 0.36$	$-45\pm 24$	-	-
	RT.74	57.2	-64.0	1.19	1.72	11.8	-	-	-	-
	RT.75	31.0	-9.1	39.52	48.67	11.7	$0.63\pm 0.12$	$+64\pm 7$	$6.05\pm 0.19$	$-188\pm 6$
	RT.76	28.3	-6.4	4.08	5.32	10.7	-	-	-	-
	RT.77	25.2	-61.4	0.31	0.69	10.7	-	-	-	-
	RT.78	24.0	-60.4	0.32	0.67	10.7	-	-	-	-
	RT.79	28.0	-27.4	0.29	0.41	10.6	-	-	-	-
	RT.80	-34.5	8.4	0.21	0.64	10.6	-	-	-	-
	RT.81	26.8	-41.0	0.06	0.08	10.2	-	-	-	-
	RT.82	29.3	-1.6	0.11	0.13	9.9	-	-	-	-
	RT.83	29.9	4.0	0.45	0.49	9.7	-	-	-	-
	RT.84	28.9	19.1	0.14	0.14	9.7	-	-	-	-
	RT.85	21.7	7.7	2.72	3.09	9.6	-	-	-	-
RT.86	23.8	2.1	0.53	0.88	9.4	-	-	-	-	
RT.87	26.2	0.4	0.42	0.51	9.4	-	-	-	-	
RT.88	21.3	3.1	3.02	3.57	9.3	-	-	-	-	
RT.89	21.8	5.2	0.64	0.80	9.2	-	-	-	-	
RT.90	24.7	3.8	23.27	28.03	8.9	$0.11\pm 0.01$	$+38\pm 3$	$1.80\pm 0.48$	$-84$ & $+63^b$	
RT.91	50.8	-51.2	0.52	0.61	8.8	-	-	-	-	
IRC+60370	IRC.01	-6.5	14.5	0.12	0.13	-39.7	-	-	-	-
	IRC.02	-5.7	16.1	0.11	0.12	-40.0	-	-	-	-
	IRC.03	33.2	-35.7	0.89	1.10	-40.2	-	-	-	-
	IRC.04	-8.4	13.7	0.18	0.29	-40.5	-	-	-	-

Table 4.7: continued.

Source	Feature	$\alpha_{off}$ (mas)	$\delta_{off}$ (mas)	Peak Int (Jy/Beam)	Int Flux (Jy)	$V_{peak}$ (km/s)	$P_L$ (%)	EVPA ( $^\circ$ )	$P_V$ ( $\times 10^{-3}$ )	$B_{  [Gauss]}$ (mG)
IRC+60370	IRC.05	4.7	-10.0	0.63	0.75	-40.6	-	-	-	-
	IRC.06	-4.7	15.8	0.20	0.24	-40.8	-	-	-	-
	IRC.07	14.3	-10.3	0.17	0.22	-40.9	-	-	-	-
	IRC.08	12.4	-9.9	0.10	0.16	-41.3	-	-	-	-
	IRC.09	-3.8	16.3	0.05	0.07	-41.3	-	-	-	-
	IRC.10	5.0	-9.4	0.16	0.22	-41.4	-	-	-	-
	IRC.11	17.2	-8.8	0.05	0.06	-43.6	-	-	-	-
	IRC.12	5.6	13.2	0.77	1.00	-43.7	-	-	-	-
	IRC.13	34.6	-24.3	0.08	0.08	-43.7	-	-	-	-
	IRC.14	28.1	13.0	0.08	0.12	-43.8	-	-	-	-
	IRC.15	-17.2	-6.0	0.11	0.14	-44.2	-	-	-	-
	IRC.16	18.6	-10.5	0.05	0.05	-44.2	-	-	-	-
	IRC.17	27.9	12.3	0.09	0.16	-44.4	-	-	-	-
	IRC.18	35.4	-23.4	0.11	0.11	-44.4	-	-	-	-
	IRC.19	6.5	13.0	1.03	1.24	-44.5	-	-	-	-
	IRC.20	3.9	13.7	0.10	0.14	-44.8	-	-	-	-
	IRC.21	15.6	-7.2	0.17	0.21	-45.2	-	-	-	-
	IRC.22	33.2	-43.1	0.06	0.06	-45.2	-	-	-	-
	IRC.23	29.6	9.9	0.13	0.21	-45.3	-	-	-	-
	IRC.24	2.8	13.1	0.08	0.11	-45.3	-	-	-	-
	IRC.25	4.8	11.0	0.10	0.14	-45.6	-	-	-	-
	IRC.26	4.0	9.6	0.11	0.31	-45.8	-	-	-	-
	IRC.27	3.7	8.4	2.04	3.29	-47.0	-	-	-	-
	IRC.28	4.5	10.0	0.05	0.08	-47.4	-	-	-	-
	IRC.29	-7.6	4.5	0.15	0.19	-47.9	-	-	-	-
	IRC.30	-8.9	4.4	0.20	0.35	-48.0	-	-	-	-
	IRC.31	-0.8	5.9	0.10	0.10	-48.0	-	-	-	-
	IRC.32	-5.6	4.4	0.08	0.15	-48.0	-	-	-	-
	IRC.33	2.8	8.0	0.05	0.06	-48.0	-	-	-	-
	IRC.34	27.8	7.2	1.14	3.31	-48.9	$1.51 \pm 0.10$	$-132 \pm 2$	-	-
	IRC.35	28.3	6.8	6.29	11.16	-49.1	$0.61 \pm 0.07$	$-67 \pm 7$	-	-

Table 4.7: continued.

Source	Feature	$\alpha_{off}$ (mas)	$\delta_{off}$ (mas)	Peak Int (Jy/Beam)	Int Flux (Jy)	$V_{peak}$ (km/s)	$P_L$ (%)	EVPA ( $^\circ$ )	$P_V$ ( $\times 10^{-3}$ )	$B_{  [Gauss]}$ (mG)
IRC+60370	IRC.36	28.3	-5.7	1.29	1.47	-49.3	-	-	-	-
	IRC.37	3.6	2.8	1.19	1.52	-49.7	-	-	-	-
	IRC.38	27.2	6.5	3.03	4.35	-49.8	0.58 $\pm$ 0.03	-74 $\pm$ 2	-	-
	IRC.39	5.6	5.8	0.17	0.24	-49.9	-	-	-	-
	IRC.40	30.6	5.8	0.22	0.34	-50.1	-	-	-	-
	IRC.41	-1.1	-0.4	1.96	2.54	-50.3	1.58 $\pm$ 0.30	-39 $\pm$ 7	-	-
	IRC.42	-0.9	0.2	11.91	20.83	-51.4	0.65 $\pm$ 0.30	-58 $\pm$ 16	-	-
	IRC.43	4.4	-8.6	1.65	2.05	-51.8	-	-	-	-
	IRC.44	0.0	0.0	51.23	67.03	-52.0	0.57 $\pm$ 0.02	-77 $\pm$ 2	2.10 $\pm$ 0.13	+47 $\pm$ 3 <sup>e</sup>
	IRC.45	-0.6	2.0	5.21	8.88	-52.3	0.45 $\pm$ 0.07	-93 $\pm$ 5	10.71 $\pm$ 1.21	+266 $\pm$ 30 <sup>e</sup>
	IRC.46	-1.3	2.0	1.68	3.06	-52.7	-	-	-	-
	IRC.47	-2.0	0.9	1.65	2.24	-53.0	-	-	15.52 $\pm$ 4.05	+331 $\pm$ 82 <sup>e</sup>
	IRC.48	-0.8	0.6	11.26	15.17	-53.3	0.46 $\pm$ 0.18	-75 $\pm$ 14	10.38 $\pm$ 0.61	+273 $\pm$ 18 <sup>e</sup>
	IRC.49	23.2	12.6	0.34	0.48	-53.8	-	-	-	-
	IRC.50	23.3	12.8	0.33	0.51	-54.0	-	-	-	-
	IRC.51	-1.6	2.8	9.08	9.43	-54.2	0.19 $\pm$ 0.02	-97 $\pm$ 6	-	-
	IRC.52	-20.0	13.0	0.14	0.26	-54.6	-	-	-	-
	IRC.53	16.7	20.4	0.06	0.07	-55.8	-	-	-	-
	IRC.54	29.6	3.9	0.40	0.49	-55.9	-	-	-	-
	IRC.55	29.2	4.0	0.09	0.14	-56.8	-	-	-	-
	IRC.56	26.4	21.2	0.03	0.04	-57.4	-	-	-	-
	IRC.57	28.8	4.0	0.23	0.53	-57.6	-	-	-	-
	IRC.58	28.5	4.6	4.89	5.48	-58.3	-	-	8.34 $\pm$ 1.40	-130 $\pm$ 22
	IRC.59	28.7	3.7	0.20	0.29	-59.0	-	-	-	-
IRC.60	14.6	-4.8	0.53	0.57	-59.5	-	-	-	-	
IRC.61	14.4	-4.5	0.76	0.81	-60.6	-	-	-	-	
IRC.62	7.0	14.4	0.07	0.09	-63.2	-	-	-	-	

<sup>e</sup> Edge/higher noise effects<sup>b</sup> Blended feature



## Chapter 5

# Asymmetric circumstellar dust envelopes around evolved stars

*We aim to investigate the circumstellar dust envelope of the evolved stars IK Tau and VY CMa, and search for asymmetries that might be present already during the current evolutionary stage of these sources. We observed our sample with the ESO 3.6 m Telescope at La Silla Observatory and the visitor instrument PolCor in the R and V bands. The PolCor uses the “lucky imaging” method, which decreases the seeing effect on the data. We observed the emission polarized by scattering on the dust in the envelopes of the sources. From that we determined the polarization degree, the direction of polarization, and the dust distribution around the sources. We detected asymmetries in the circumstellar envelope of both sources. Elongations were detected in the polarized image of IK Tau in the R band, where the CSE around the source shows an elliptical morphology, and the presence of a waist is discussed. The CSE around IK Tau was not detected in polarized light in the V band, but the total intensity image in this band also shows signs of asymmetry. The images of VY CMa confirm the complex morphology of the nebula around this source. Our images show that the dust nebula extends to more than 20" from the star. In contrast to IK Tau, the polarization vectors around VY CMa do not follow a centrosymmetric pattern.*

*The results reported in this chapter are currently in preparation for publication by Leal-Ferreira et al. The observations presented in this chapter are part of an observing campaign led by Dr. M. Maercker and Dr. S. Ramstedt. The observations were performed by Dr. S. Ramstedt, myself, and collaborators.*

## 5.1 Introduction

The study of the circumstellar envelope of evolved stars is crucial for the understanding of stellar evolution. By imaging the CSE of evolved stars, we can look for emerging signs of asymmetry and, from the dust scattered light of the sources, investigate the structure and physical extension of the circumstellar dust envelope, as described in details by Ramstedt et al. (2011). Note that, by assuming that the incident radiation from the star is unpolarized, the observed light will only be strongly polarized when the scattering angle is  $\sim 90^\circ$ . Therefore, the polarized scattered light actually maps the dust distribution in the plane of the sky that passes through the star.

The low- and intermediate-mass stars (with initial mass between 0.8 and 8  $M_\odot$ ) will evolve into an asymptotic giant branch star and, later, into a planetary nebula. The mass loss from these stars maintains spherical symmetry at least until they reach the AGB phase. However, most of the observed PNe are asymmetrical (e.g., Manchado 2003) and it is not yet clear when exactly these sources lose their symmetry, nor which mechanisms are responsible for the change of morphology. The investigation of the CSE around AGB stars can help us to understand this metamorphosis as it allows us to search for upcoming asymmetries already during the AGB phase. In this chapter, we use the AGB star IK Tau to illustrate the analysis of an asymmetrical dust CSE.

High-mass stars, on the other hand, evolve quickly, making their observation more challenging. Like all stars, their evolution depends on their initial mass and they might evolve into red supergiants (RSG), blue supergiants, Cepheids, Wolf-Rayet stars, Of stars, or luminous blue variables before turning into a supernova and a neutron star or a black hole (Peters & Hirschi 2013). One such high-mass evolved star is VY CMa, a red supergiant with a high mass-loss rate which is surrounded by an asymmetric nebula. This is a well-studied source and the inner region of its CSE was analyzed before with observations from the Hubble Space Telescope (Jones et al. 2007). In this chapter we analyze the most extended region of its envelope, which is more than twice as extended as previously known.

This chapter presents the techniques, the data reduction process, and the data

details in Section 5.2. The results are reported in Section 5.3 and discussed in Section 5.4. The conclusions are given in Section 5.5.

## 5.2 Observations and Data Reduction

We used the ESO 3.6 m Telescope at the La Silla Observatory, Chile, together with the Polarimeter and Coronagraph (PolCor) instrument to observe the CSE of our sample, which is composed by 14 evolved stars. The observations were carried out between October 18<sup>th</sup> and November 2<sup>nd</sup>, 2011, when ten nights of that period were dedicated to the project. In this chapter we present the results of two sources from the sample, observed in the dates presented in Table 5.1: IK Tau and VY CMa. The AGB star IK Tau was observed in three nights in the  $R$  band and for this case the data were combined together in the data reduction process, so that the signal to noise ratio (SNR) was increased. In order to block the direct light of the star in the observations and make the detection of the faint circumstellar light possible, we used a coronagraph of 6'' of diameter in the observations. We obtained images of the total intensity and of the linear polarized light scattered by dust for each source and band with a field of view of  $\sim 58'' \times 58''$ . The pixel scale of the observations is  $0.114'' \text{ pixel}^{-1}$ .

The PolCor instrument is capable of observing individual images at a high frame rate. As a consequence, individual snapshots with short exposure time in each one of the four polarization positions ( $A0$ ,  $A45$ ,  $A90$ ,  $A135$ ) are obtained. Each snapshot is stored, so the “lucky imaging” technique can be applied during the data reduction process. The goal of this process is to decrease the effective seeing. It consists of selecting only the sharpest frames to combine to the final image. The selected frames are shifted and added together, creating new  $0^\circ$ ,  $45^\circ$ ,  $90^\circ$ , and  $135^\circ$  images, and the effective seeing in these new images is usually improved by a factor of 20-30% if compared with the seeing of the night of observation. The output images are then

used to derive the Stokes parameters:

$$I = A0 + A45 + A90 + 135 , \quad (5.1)$$

$$Q = A0 - A90 , \quad (5.2)$$

$$U = A45 - A135 . \quad (5.3)$$

We searched for background stars in the  $I$  images and measured their Full Width at Half Maximum (FWHM) to determine the effective seeing in the final images. For the VY CMa images we derived an effective seeing of 1.1" in both bands (which were observed in the same night). This value can be compared with the seeing during the night in which VY CMa was observed, which varied between 0.9" and 1.5". In the images of IK Tau, however, we could not identify background stars that could be used to estimate the seeing. In this case we can only estimate an improvement over the seeing of the night, that varied between 0.6" and 2.5" in the three nights of observations in the  $R$  band, and between 0.5" and 0.9" in the  $V$  band.

The SNR of the  $I$ ,  $Q$ , and  $U$  images is limited by the number of frames observed in each polarization position, as these frames are used to derive  $I$ ,  $Q$ , and  $U$ . In Table 5.1 we show the observation details of the targets, including the number of individual frames ( $A0$ ,  $A45$ ,  $A90$ ,  $A135$ ) that were observed and used in Eqs. 5.1, 5.2, and 5.3.

After deriving the Stokes parameter images, we measured and subtracted the background level in the  $Q$  and  $U$  images. We then smoothed the images with a Gaussian kernel to decrease the noise and derived images of the polarized power ( $P$ ), polarization degree ( $P_{deg}$ ), and polarization angle ( $\Psi$ ) according to the following equations:

$$P = \sqrt{Q^2 + U^2} , \quad (5.4)$$

$$P_{deg} = \frac{P}{I} , \quad (5.5)$$

$$\Psi = 0.5 \times \arctan \left( \frac{U}{Q} \right) . \quad (5.6)$$

Smoothing the images degrades the effective seeing, but since we are not analyzing small scale structures, this approach does not limit our analysis.

We assume that the radiation emitted by the star is initially unpolarized, and that the interstellar medium and atmosphere of the Earth, through which the light travels, does not have a significant effect on the observations. We also assume that no significant degree of polarization is introduced by the telescope. Polarization standard stars were observed in order to obtain the absolute polarization angles of the targets and to determine the accuracy of the polarization measurements. Based on the observations of these calibrators, we subtracted  $185^\circ$  due to the orientation of the instrument from the results given by Eq. 5.6 to obtain the absolute polarization angles.

Note that, despite the usage of the coronagraph, a contribution from the star is still present in the total intensity images. As a consequence, a stellar point spread function (PSF) spreads throughout the entire field of view. In order to derive an image of  $I$  which is free from this contribution, one needs to assume a PSF model and subtract it from the observed  $I$  image. With this aim, we observed template stars of similar magnitude and with the same set up as the targets. However, after further investigating the data, we concluded that the PSF shape is significantly affected by the position of the star behind the coronagraph. Since the template stars and the targets cannot be guaranteed to reside at the same position in reference to the coronagraph, we decided that subtracting a PSF model would do more harm than good by introducing spurious structures to the data. Therefore, we did not subtract a PSF model from  $I$ . As a result, we can only derive lower limits on  $P_{deg}$  for all targets.

We performed the data reduction process using the Data Reduction Software for PolCor. This software performs the “lucky imaging” technique and derives the  $I$ ,  $Q$ , and  $U$  images as described. The Data Reduction Software for PolCor is briefly described by Olofsson et al. (2012), and discussed in details by Ramstedt et al. (2011).

Table 5.1: Observation details

Source	Class	F	MD (")	TFram	Sharp	Fr0	Fr45	Fr90	Fr135	Exp (s)	Date (dd/mm/2011)
IK Tau	AGB	<i>R</i>	6	13500	80%	9089	9369	8829	8830	0.1	22/10 & 23/10 & 30/10
IK Tau	AGB	<i>R</i>	6	13500	85%	11685	11930	11507	11472	0.1	22/10 & 23/10 & 30/10
IK Tau	AGB	<i>V</i>	6	3150	90%	2301	2328	2268	2264	0.1	31/10
VY CMa	RSG	<i>R</i>	6	1500	90%	1352	1359	1351	1371	0.05	18/10
VY CMa	RSG	<i>V</i>	6	1500	90%	1178	1211	1180	1202	0.05	18/10

From column 1 to column 6: Source name (Source), object class (Class), filter band (F), mask diameter (MD), number of observed frames (TFram), number of selected frames in each polarization directions (Fr0, Fr45, Fr90, Fr135), exposition time of a single frame (Exp), and date of observation (Date).

## 5.3 Results

We derived and analyzed  $I$ ,  $P$ , and  $P_{deg}$  for each source and band. The total intensity and polarized images of IK Tau and VY CMa are presented in Figs. 5.1, 5.2, 5.4, and 5.5, where north is up and east is left. Masks based on SNR were applied to the images, and the IK Tau ( $R$  and  $V$ ) and VY CMa ( $V$ ) images are filtered to only display the emission with  $\text{SNR} > 5$ , while the VY CMa ( $R$ ) images are filtered to show the emission with  $\text{SNR} > 7$ . We also masked out a center region with  $8''$  of diameter to avoid not only the coronagraph region itself, but also a region that might have suffered from distortions due to border effects of the coronagraph. We also show the polarization vectors overplotted on the polarized intensity images, where the vector sizes are scaled with the lower limit of the polarization degree, and their directions were obtained from Eq. 5.6 (and corrected by the instrumental offset of  $185^\circ$ ). Although the PolCor instrument contains a Lyot stop (Lyot 1939) designed to remove spider effects, we have avoided the spider region when plotting the polarization vectors. This was done to make absolutely sure not to introduce potential artifacts caused by the spider vane in the weak signal from the CSE distribution. The spider region is the area plotted in gray-scale in all polarized light images.

In Figs. 5.3 and 5.6, we present the azimuthal averaged radial profile (AARP) of the total intensity, polarized and polarization degree images. Each plot shows five curves, where the red, blue, green, and magenta curves correspond to AARPs over individual angle ranges, each one derived from a different quadrant of the image. In black we show the curve derived from the average of the previous four. We avoided contamination of the spider mask and bright background stars when selecting the angle ranges. The definition of each angle range is shown in Table 5.2, where  $0^\circ$  is defined to be in between quadrants Q1 and Q4, and the angles increase counterclockwise. Quadrants Q1, Q2, Q3, and Q4 are defined respectively as top right, top left, low left, and low right in the images. We highlight that artifacts in the images (e.g., diffraction spikes) and clumps within the circumstellar envelope may affect the AARPs, in particular for zones with smaller radii.

Table 5.2: Quadrant angle ranges

Source	FB	Q1 ( $^{\circ}$ )	Q2 ( $^{\circ}$ )	Q3 ( $^{\circ}$ )	Q4 ( $^{\circ}$ )
IK Tau	<i>R</i>	35–55	125–145	240–250	305–325
IK Tau	<i>V</i>	35–55	125–145	240–250	305–325
VY CMa	<i>R</i>	30–60	110–125	205–230	295–315
VY CMa	<i>V</i>	30–60	110–130	205–230	295–315

From column 1 to column 6: Source name (Source), filter band (FB), and the angle ranges of quadrants Q1, Q2, Q3, and Q4.

### 5.3.1 IK Tau

IK Tau is a Mira-type variable with a period of 470 days (Wing & Lockwood 1973). This oxygen-rich AGB star has a mass-loss rate between  $4.5 \times 10^{-6}$  and  $10^{-5} M_{\odot} \text{ yr}^{-1}$  (Ramstedt et al. 2008; De Beck et al. 2010; Decin et al. 2010), and is located at a distance of 250–265 pc from us (Hale et al. 1997; Olofsson et al. 1998).

We derived two sets of images for IK Tau in the *R* band. These images were obtained from the same data set, but different sharpness criteria were adopted in the data reduction process. The sharpness criteria is defined by the fraction of frames that are selected to compose the images *A0*, *A45*, *A90*, and *A135*. For the first case of IK Tau in the *R* band, we selected 85% of the frames (Figs. 5.1 top and 5.2 top) and in the second case 80% (Figs. 5.1 center and 5.2 center) of the data were used. Using the 85% sharpest frames, the signal to noise ratio is higher than when 80% of the frames are selected, and the fainter extended emission is enhanced. However, we expect the 80% case to be sharper than the 85% case. Although the difference in the sharpness criteria is of only 5% between the cases (see Table 5.1 for the total number of frames that were actually used in each case), some structures are more apparent in one case compared to the other. But, we note that the global morphology of the source is similar, regardless of the sharpness criteria, i.e., a fairly spherical morphology is seen in the total intensity images and an elliptical shape is seen in the images of the dust scattered light.

In Figure 5.1 (left and middle), we show the total intensity image of IK Tau in



the  $R$  band, which reveals a fairly spherical shape. The faint CSE emission in the  $V$  band total intensity image, however, shows signs of asymmetry (Figure 5.1, bottom). This asymmetry has an elongation up to about  $12''$  (or about 3000–3200 AU) from the center of the source in quadrant Q4. The AARPs presented in the first column of Figure 5.3 depict these results more clearly. In the  $R$  band, the AARPs of the four quadrants of the total intensity images (both the 80% and 85% sharpness criteria images) are overlaid on each other, indicating that the source has a spherical morphology. From the AARP of the  $V$  filter total intensity image (Figure 5.3, right) one can notice that the emission in the quadrant Q4 is indeed higher than in the other quadrants from about  $6''$  to  $11.5''$  from the star center.

The images of the polarized light in the  $R$  band (Figure 5.2 top and center, for sharpness criteria equals to 85% and 80%, respectively) show that the dust distribution around the source has an elliptical shape (which is more accentuated in the 85% case). In the 80% case a waist is seen in quadrants Q1 and Q3 and an elongation is seen in quadrant Q4 (the same quadrant where an elongation is also seen in the  $V$  band total intensity image). In the 85% image, which is less sharp, the waist is not obvious but a hint of its presence can be noticed in quadrant Q3. We interpret that the waist is real and that it is not as prominent in the 85% case because it becomes blurred when more data are added to derive the image. The elongation in quadrant Q4 can be seen in the both, the 80% and the 85% cases. However, in the 85% image such elongation extends also into quadrant Q3. Despite the few differences between the images derived in the 80% and in the 85% cases, we highlight that asymmetries can be seen in the dust scattered light images in both cases.

The AARPs plots of the  $R$  band polarized images show that the profiles of the different quadrants do not follow each other, what is expected in case of presence of asymmetry in the dust CSE. The level of emission in quadrants Q3 and Q4 (green and magenta) is higher than in quadrants Q1 and Q2, and the emission in quadrant Q4 (magenta) is the most extended one (Figure 5.3, top middle and center middle). The observed dust envelope in the  $R$  band extends for up to  $\sim 15''$  from the center of the source, which corresponds to about 3750–4000 AU, while we did not detect the CSE in polarized light in the  $V$  band (Figure 5.2 bottom and Figure 5.3 lower

center and lower right).

The polarization vectors are mainly centrosymmetric in the polarized image of the  $R$  band with sharpness criteria equal to 85% (Figure 5.2, top). However, in Figure 5.2 center (sharpness criteria equals to 80%), one can notice that the vectors follow a centrosymmetric shape in quadrants Q2 and Q4, but in quadrants Q1 and Q3 this pattern is not clear, as the polarization vectors are missing in the waist region. The (lower limit of the) polarization degree in the  $R$  band is up to  $\sim 4\%$  in the inner regions of the CSE and decreases outwards (Figure 5.3, right top and right center plots).

### 5.3.2 VY CMa

The supergiant VY Canis Majoris (VY CMa) is an oxygen-rich star located at a distance of  $\sim 1.2$  kpc (Choi et al. 2008; Zhang et al. 2012) with a mass-loss rate of  $3.9 \times 10^{-4} M_{\odot} \text{ yr}^{-1}$  (updated for the distance of 1.2 kpc; Danchi et al. 1994). The source is a semi-regular star with a period of  $\sim 2000$  days (Marvel 1996) and it is a well-studied object with a complex morphology (e.g., Jones et al. 2007).

Our observations trace the extended part of the envelope and the total intensity images observed in the  $R$  and  $V$  bands (Figure 5.4) already show signs of asymmetry. Elongations can be seen in both bands mainly in quadrant Q2. The AARPs of the different quadrants of these total intensity images (Figure 5.6; left) do not perfectly align each other, suggesting an asymmetric CSE. The radial profile of the quadrant Q2 in the  $R$  band shows enhanced emission between  $\sim 7.5''$  and  $\sim 15.5''$ , while the profiles of quadrants Q1 and Q4 are very similar to each other and show a decreased level of emission. The  $V$  band AARPs of the total intensity image follows a similar behavior and the emission from quadrant Q2 is enhanced from  $\sim 8''$  to  $\sim 13.5''$ .

The VY CMa polarized images (Figure 5.5) show that the dust envelope extends up to about  $20.5''$  corresponding to  $\sim 24600$  AU from the center of the source in the  $R$  band, and to about  $17''$  corresponding to  $\sim 20500$  AU in the  $V$  band. The complex morphology is also clearly seen in the polarized image, where an elongated structure with enhanced flux is seen in quadrant Q2. This, again, is clear from the AARPs of the polarized images (Figure 5.6; center). In quadrant Q2 (blue curve)

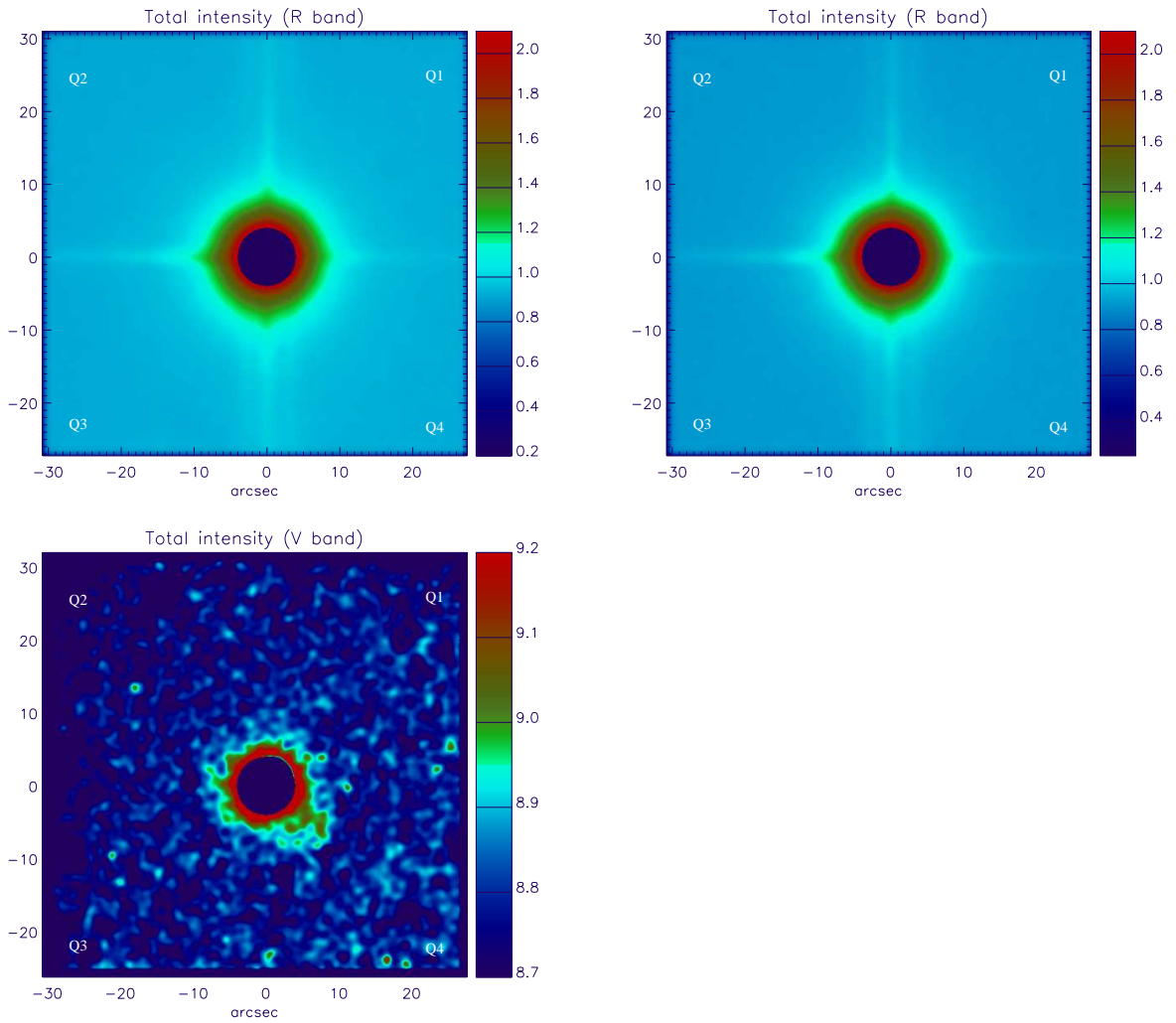


Figure 5.1: IK Tau total intensity light images. The top (sharpness criteria equals to 85%) and center (sharpness criteria equals to 80%) images correspond to the observation in the *R* band in logarithmic scale, and the bottom image corresponds to the observation in the *V* band in linear scale.

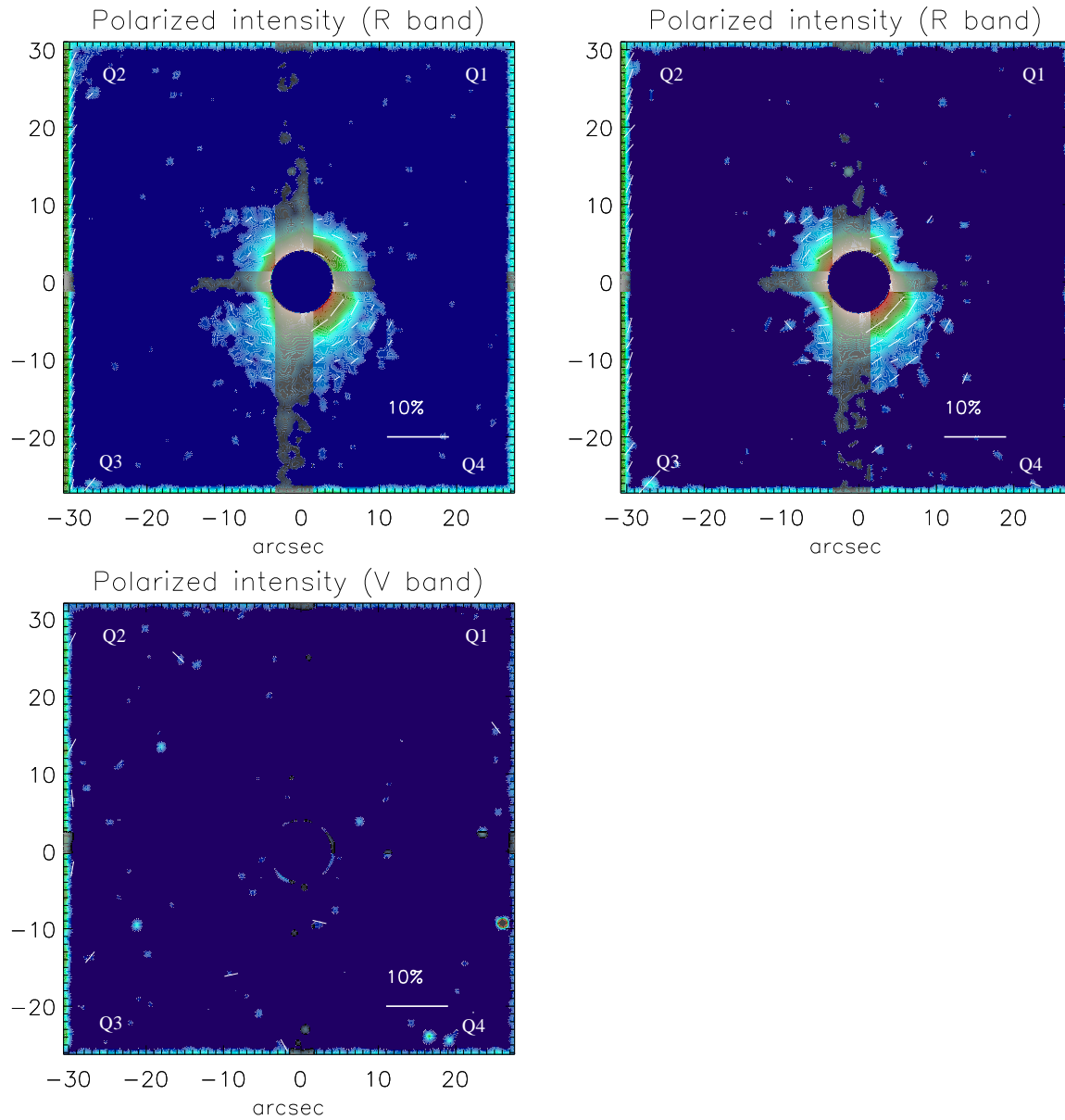


Figure 5.2: IK Tau polarized images in logarithmic scale. The white vectors show the polarization direction and their sizes are scaled with the lower limit of the polarization degree. The top and center images show the observations in the  $R$  band with sharpness criteria of 85% and 80%, and the bottom image shows the observation in the  $V$  band.

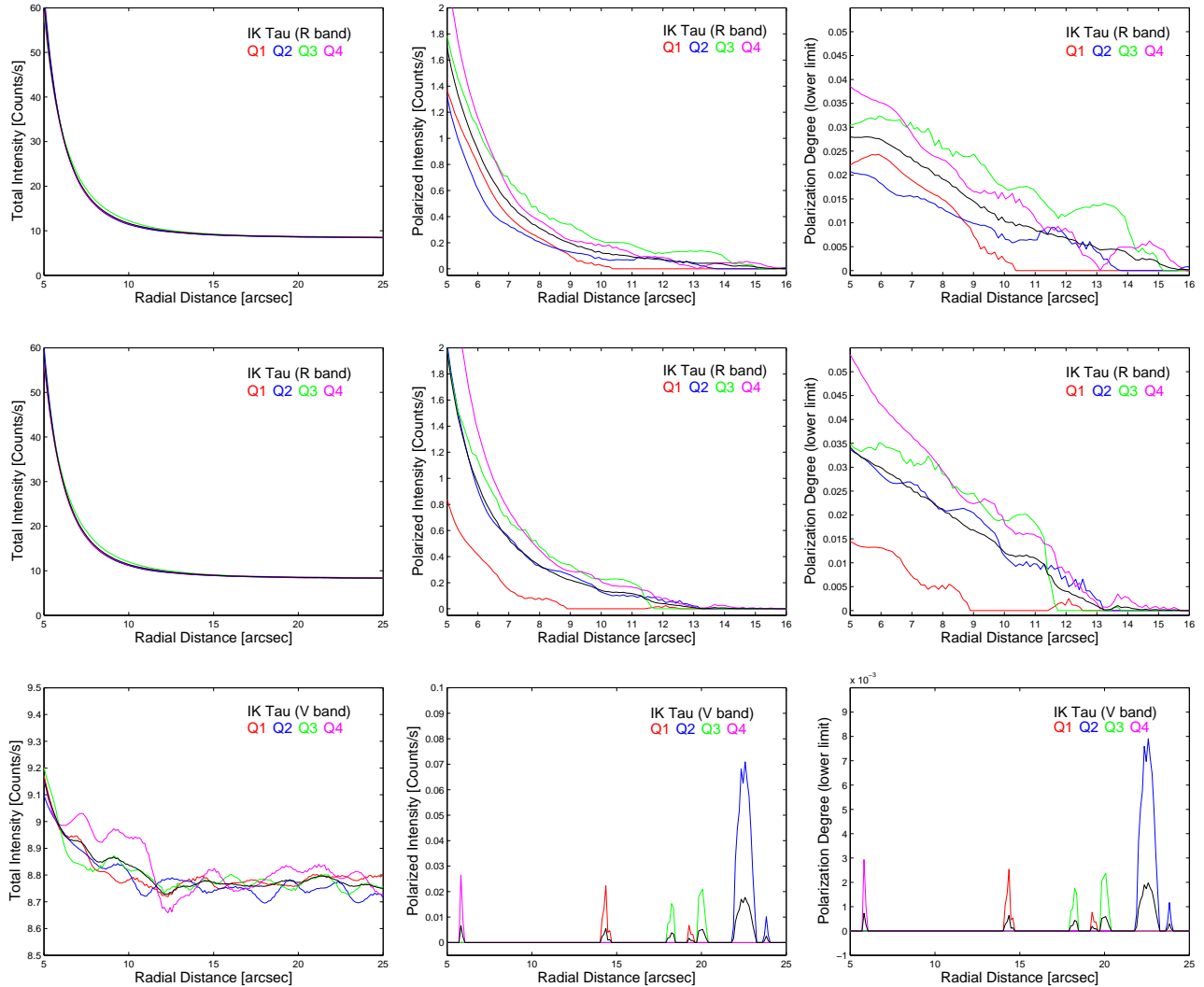


Figure 5.3: Radial profile of IK Tau observations. The colored lines refer to the profile over four different directions, averaged over a given angle aperture. Each one of these four profiles corresponds to a different quadrant. The black line is the mean of the four red lines. The top and center plots show the radial profiles in the  $R$  band, with sharpness criteria of 85% and 80%, and the ones in the bottom correspond to the  $V$  band. From left to right, the plots correspond to the total intensity, polarized intensity, and the polarization degree (lower limit) images.

the emission is enhanced mainly from  $\sim 8''$  to  $\sim 12''$  in both bands (and still higher further out in the  $R$  band). The decreased emission in quadrant Q1 (red curve) is also clear for the  $R$  band image, and in quadrant Q3 (green curve) for the  $V$  band image.

The direction of the polarization vectors are not centrosymmetric, neither in the  $R$  band nor in the  $V$  band. While the vectors in quadrants Q2 and Q4 appear tangentially to the CSE, the vectors in quadrant Q3 have a radial orientation and the vectors in quadrant Q1 show a pattern between these two cases.

The lower limit of the polarization degree for this source is of up to  $\sim 60\%$  at  $\sim 5''$  from the star, and declining to as low as  $\sim 3\%$  at  $\sim 17''$  from the center of the source (Figure 5.6; right). While the polarization degree is higher in quadrant Q1 in the inner parts of the CSE (from  $\sim 5''$  to  $\sim 7-8''$ ), it becomes higher in quadrant Q2 in outer regions, between  $\sim 8.5''$  and  $\sim 12''$ , where the elongation of the CSE is observed.

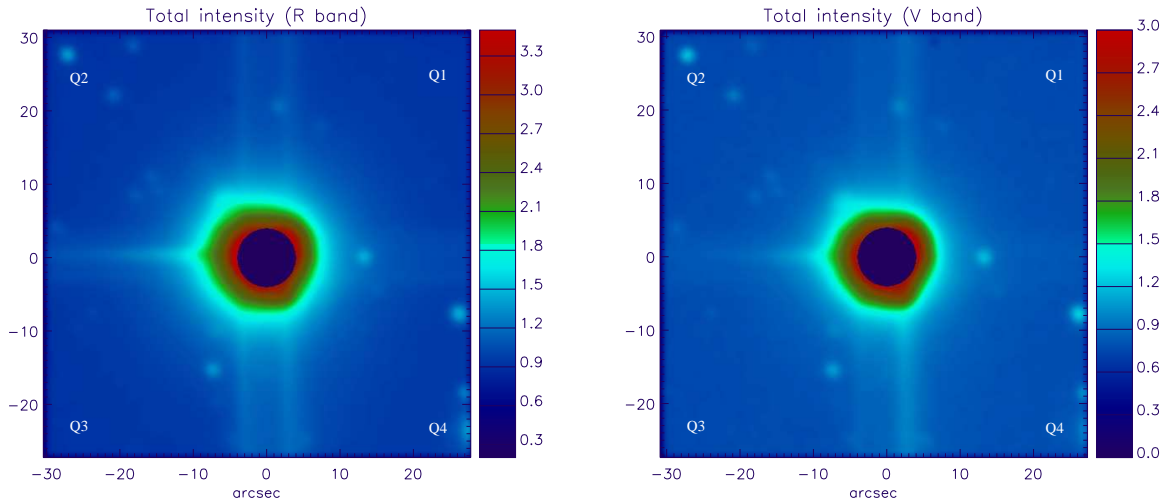


Figure 5.4: VY CMa total intensity image in logarithmic scale. The top image corresponds to the observation in the  $R$  band and the bottom image corresponds to the observation in the  $V$  band.

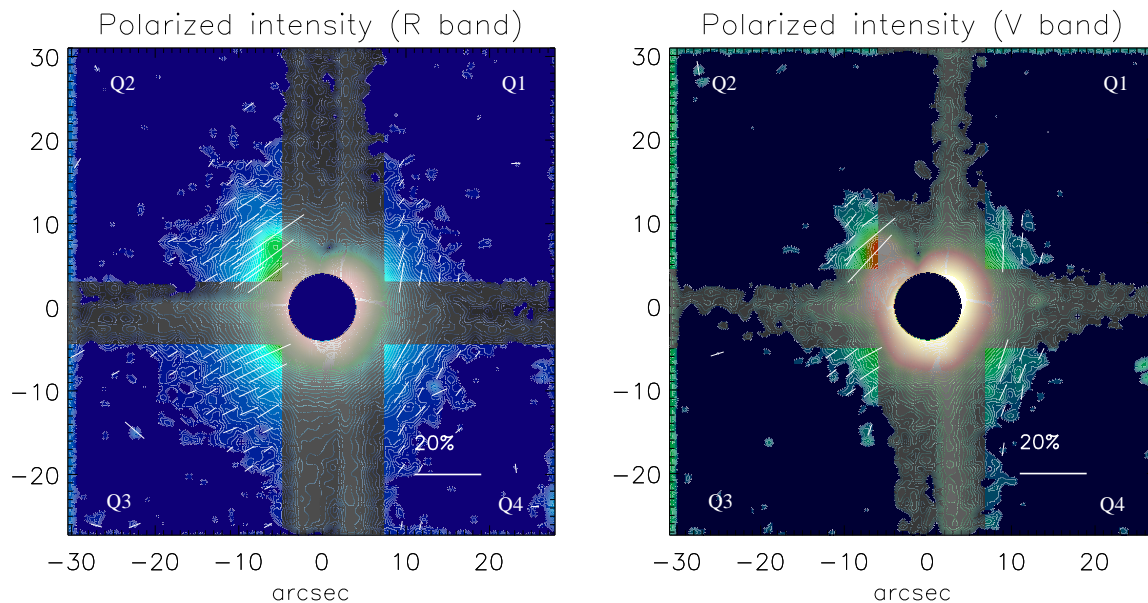


Figure 5.5: VY CMa polarized light image in logarithmic scale. The white vectors show the polarization direction and their sizes are scaled with the (lower limit of the) polarization degree. The top image corresponds to the observation in the  $R$  band and the bottom image corresponds to the observation in the  $V$  band.

## 5.4 Discussion

### 5.4.1 IK Tau

The IK Tau dust envelope was analyzed within the spatial scale of hundreds of milliarcseconds by Weiner et al. (2006). The authors derived models to fit the mid-infrared interferometry observations and concluded that asymmetries are present in the CSE of this source. They report the presence of an arc-like structure at about 200 mas northeast of IK Tau. They also showed that the dust density around the star changed considerably from the years 1993–1994 to 2003–2004. In the spatial scale of tens of arcseconds, Castro-Carrizo et al. (2010) mapped the molecular gas of IK Tau in the CO  $J=1-0$  and  $J=2-1$  transitions. They found evidence for aspherical winds in the inner region of IK Tau and reported that in both maps an elongation toward west is seen around this source.

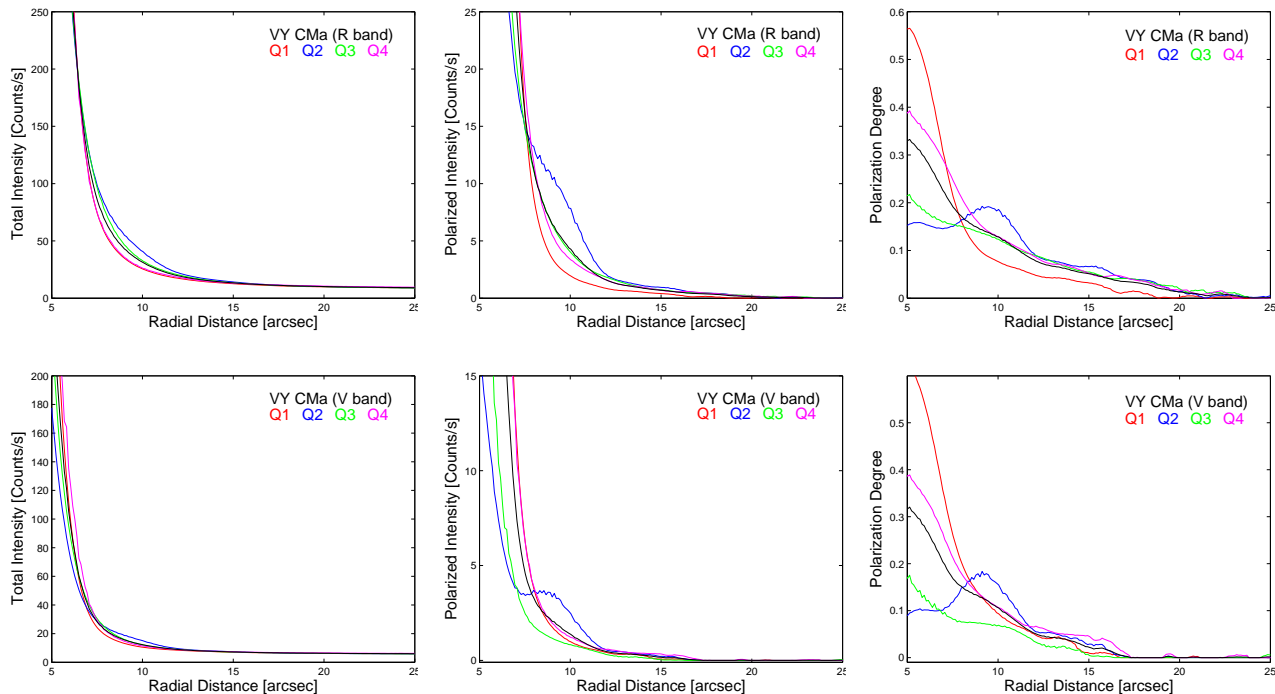


Figure 5.6: Radial profile of VY CMa observations. See caption of Figure 5.3 for details.

Our results map the CSE of IK Tau at similar spatial scales as the CO maps from Castro-Carrizo et al. (2010). As reported in Section 5.3.1, from the dust scattered light in the R band we detected a waist in the northwest-southeast direction and an elongation toward southwest. In the faint total intensity image in the V band we also detected an elongation toward southwest in the CSE. Thus, we did not find a correlation between the asymmetries detected in our work and the ones from the CO maps. However, as different types of emission are generated by different physical processes, the two observations can lead to distinct morphologies of the CSE.

Based on our results, we cannot conclude which shaping mechanisms from the ones described in Chapter 2 are acting on IK Tau. However, we highlight that Vlemmings et al. (2012) detected a magnetic field around this AGB star at distances of  $\sim 250$  and  $\sim 800$  AU and claim that the overall field geometry is either east-west or north-south oriented. Moreover, Leal-Ferreira et al. (2013) measured the field



strength to be between  $\sim 100$  and  $\sim 200$  mG at tens of AU, while Herpin et al. (2006) measured it to be between 1.9 and 6 G between  $\sim 5$  to  $\sim 10$  AU. Therefore, we suggest that the magnetic field could play a role in the shaping process of the asymmetric dust envelope we observed. Additionally, based on the dust scattered light images we observed in the  $R$  band, we highlight the possibility of the existence of a waist around IK Tau which could be the consequence of the presence of a torii or disk and be significant for the morphological evolution of this AGB star.

### 5.4.2 VY CMa

We reported a complex morphology of the nebula around VY CMa at large radius in Section 5.3.2. This adds to previous results for the innermost regions, where a complex morphology was also detected (e.g., Smith et al. 2001; Jones et al. 2007). Kastner & Weintraub (1998) suggested that this morphology is a consequence of a flattened envelope and/or that the star is surrounded by a massive circumstellar disk which would hide the star in optical wavelengths. Such nearly edge-on equatorial ring or disk of dust would have an outer radius of  $\sim 1400$ – $2000$  AU (e.g., Herbig 1970; Smith et al. 2001), and the axis of rotation of the star and disk would be oriented in the northeast-southwest direction, with the southwest lobe closer to us. However, Humphreys et al. (2007) argue that there is no strong evidence for the presence of an axis of symmetry or a bipolar axis in VY CMa and, therefore, the morphology of the nebula around the star is more consistent with a history of localized mass-loss episodes. These mass-loss events would not necessarily be aligned with the axis of rotation of the source, its equator, or any axis of symmetry. Moreover, individual arcs and knots are not only located at different distances, but also move with different velocities and toward different directions. Nevertheless, a bipolar outflow was detected from H<sub>2</sub>O maser observations at hundreds of AU from the star (Yates 1993; Yates & Cohen 1994). The authors suggest that the outflow is the result of rotation and/or a stellar magnetic field. Smith et al. (2001) also claim that a strong magnetic field combined with turbulence could be responsible for generating a rotational axis of symmetry in the star. A magnetic field with a strength up to 1.9 G at a few AU (Herpin et al. 2006), and of about 200 mG at a

few hundreds AU has indeed been reported around this source (Vlemmings et al. 2002).

The most extended emission of VY CMa detected until the present date was observed in a molecular line survey with the Submillimeter Array (SMA) between 279 GHz and 345 GHz. These observations show that the complex morphology of the nebula can be seen in the emission of many different molecules. The most extended structure that was detected was observed from the intense line of CO(3–2), which shows a hint of emission around  $7.5''$  toward northeast. However, as these observations filtered out more extended emissions, it is possible that the nebula is larger than what is shown in the SMA maps (Kaminski et al. 2013).

Jones et al. (2007) explored the three-dimensional structure of the circumstellar dust distribution in the envelope around VY CMa. Using polarimetry observations taken with the Hubble Space Telescope, they mapped the source over a region of about  $6.5'' \times 6.5''$  and derived polarization vectors with fractional polarization from 10% to 80%, with a strong centrosymmetric pattern in all directions except directly east. The polarization in this nebula was also analyzed by Herbig (1972), who mapped the nebulosity over a region of  $\sim 8'' \times 12''$  and found a radially plane-polarized emission up to 70%.

The elongation we detected toward northeast in all VY CMa images agrees with previous reports of an elongated structure in that direction in the dust distribution (e.g., Smith et al. 2001; Jones et al. 2007) and in the molecular gas distribution around the star (Kaminski et al. 2013). The elongation is located in the direction of the rotational axis of the source. If a ring or disk with radius of  $\sim 1400\text{--}2000$  AU is indeed present around VY CMa, its location would be internal to the emission we report here, as our observations trace the very extended region of the nebula. We highlight that our images show that the dust distribution around VY CMa extends for more than  $20''$  or  $\sim 24600$  AU, which is more than twice as far as shown by the SMA maps of Kaminski et al. (2013).

Decin et al. (2006) investigated the mass-loss history of VY CMa in detail with radiative transfer modeling and compared their results to the observations from Smith et al. (2001), which corresponds to a maximum radius of about  $7''$ . As our

observations map the nebula up to a much larger radius, this could be used to constrain models at outer regions of the source. Furthermore, Decin et al. (2006) suggested that the asymmetries in the CSE would be more relevant to innermost regions and, as they focused their analysis on larger radii, they assumed spherical symmetry in their models. Our results not only show the extended emission of the nebula, but also confirm that asymmetries are still present at large radii. This indicates that a more realistic model needs to account for asymmetries even if only outer regions are studied. Thus, our results can be used to gain a better understanding of the mass-loss history of VY CMa.

The direction of the polarization vectors in our observations is puzzling. While it appears centrosymmetrical in the northeast and southwest, it is radial in southeast. In the northwest the orientation of the polarization vectors is neither centrosymmetrical nor radial. Herbig (1972) discusses the rotation of the polarization direction as a function of wavelength for this source. However, our results show a complex orientation of the polarization vectors within a given observing band. The same complex behavior is seen in  $R$  and  $V$  bands. Moreover, neither Herbig (1972) nor Jones et al. (2007) detected a similar pattern of polarization orientation when mapping the inner region of VY CMa. However, Jones et al. (2007) reported that the direction of the polarization vectors in the nebula is not isotropic, as they observed that the polarization vectors are not centrosymmetric in the east direction.

We can only speculate on the reason for the observed orientation of the polarization. The nebula around the star extends up to more than 20000 AU and it is inhomogeneous and anisotropic. Therefore, a possible scenario could be multiple scattering events by different nebula clumps. However, further observations are needed to confirm the results.

## 5.5 Conclusions

We observed the AGB star IK Tau and the RSG VY CMa in the  $R$  and  $V$  bands. The observations were performed with the ESO 3.6 m Telescope and the visitor instrument PolCor.

In IK Tau we detected a dust polarized circumstellar envelope that extends up to  $\sim 15''$  in the  $R$  band and up to  $\sim 12''$  in the  $V$  band. By applying different sharpness criteria in the data reduction process, we produced two sets of images of this source in the  $R$  band. No significant differences are seen in the total intensity images and both sharpness criteria give overall spherical symmetric images as a result. However, the dust polarized images derived with these different sharpness criteria show some different structures. While the global elliptical morphology is consistent in both cases, the presence of a waist is more clear in the sharper case (with lower SNR). Moreover, while in the higher SNR case the polarization vectors have a centrosymmetric pattern all around the source, they are missing in the waist region in the lower SNR case. In the  $V$  band the IK Tau total intensity image shows that the faint CSE has an elongation in the southwest region. The CSE was not detected in the polarized light in the  $V$  band.

The VY CMa dust polarized images show an extended envelope up to  $\sim 20.5''$  in the  $R$  band, and up to  $\sim 17''$  in the  $V$  band. Our observations show that the nebula around the star extends more than twice as far as shown by previous observations of this source. The complex morphology of the nebula is clear even at large radii, both from the polarized images and from the total intensity images, and its shape agrees with previous observations of inner regions of the object. The polarization vectors around this source show a puzzling pattern and while they are centrosymmetric in the northeast and southwest they are radial in the southeast. In the northwest the orientation of the vectors is neither centrosymmetric nor radial. Such behavior is seen in  $R$  and  $V$  bands. We suggest that new observations should be performed to confirm if, in fact, this behavior is real.

## Chapter 6

# Detached shells around the AGB stars R Scl and V644 Sco

*In this chapter we present the first results of observations of the detached shells around R Scl and V644 Sco with the ESO 3.6 m Telescope and the visitor instrument PolCor. The complete analysis of this work is in preparation for publication by Maercker et al. The data analyzed here were observed by collaborators and myself, and correspond to a sub-sample observed in a mission led by Dr. M. Maercker and Dr. S. Ramstedt.*

*We detected a shell around R Scl that is brighter in the north than in the south, and observed that the region between the shell and the star does not look empty in dust scattered polarized light. Our images match well previous observations taken with the Hubble Space Telescope and with the Atacama Large Millimeter/submillimeter Array. The derived radius of about 5250 AU of the shell implies the age of the shell to be  $\sim 1750$  years. We fitted a Gaussian to the radial profile of the shell and estimated from its FWHM the width of the shell to be  $\sim 4.7''$ . However, the derived radius is likely underestimated by  $\sim 8\%$  and the shell width is likely overestimated by  $\sim 20\%$ .*

*For the first time an image of the dust detached shell around V644 Sco is reported and the observations show a shell that is sharper than the one around R Scl. The region between the star and the shell appears more empty in dust polarized light than the corresponding region in R Scl. The detached shell surrounding V644 Sco is brightest in the northwest, and the derived radius of about 6400 AU implies that the shell is  $\sim 1300$  years old. The width of the shell was estimated to be  $\sim 3.9''$ . Again, we expect the derived radius*

*to be underestimated by  $\sim 8\%$  and the shell width to be overestimated by  $\sim 20\%$ .*

## 6.1 Introduction

Geometrically thin (width/radius  $< 0.1$ ) detached shells around AGB stars were first detected by Olofsson et al. (1988) from CO line emission. The mechanism of how these shells are formed is not yet fully understood, but the widely accepted model for their formation predicts that, as a consequence of a helium shell flash, an intense and short ( $\lesssim 500$  years) mass-loss event can take place. In the moment after this eruption and until the stable wind blows again, the mass loss would be interrupted or be very low. The high density expanding shell related to the He shell flash mass-loss event would expand faster than the material expelled previously to the He shell flash. Therefore, the faster wind would sweep the slower one, forming the detached shell (Steffen & Schönberner 2000; Mattsson et al. 2007). The velocities associated with the fast and the slow expanding shells are not yet well determined, but a model presented by Mattsson et al. (2007) predicts wind velocities of  $\sim 20$  km/s and  $\sim 10$  km/s for the fast and slow winds, respectively.

So far, only the following AGB stars are known to be surrounded by detached shells of dust and gas: S Sct (Olofsson et al. 1988), R Scl, V644 Sco, U Ant, TT Cyg (Olofsson et al. 1996), U Cam (Lindqvist et al. 1999), and DR Ser (Schöier et al. 2005). These seven sources are unique for the investigation of mass-loss events of evolved stars, as the shells give us the chance to learn about the temporal evolution and the direction dependence of such events.

González Delgado et al. (2001, 2003) were the first to image detached shells around AGB stars from dust scattered light. They observed R Scl to have an almost perfectly spherical shell of  $\sim 21''$  in radius, with its intensity dropping sharply in total intensity light. From the dust scattered image and a model of the dust scattering they concluded that the shell is  $\sim 2''$  wide. In an analysis complemented by data from the literature, González Delgado et al. (2003) also discuss that three different regions are likely to compose the CSE of R Scl: the present-day mass-loss material

located in the inner region ( $< \sim 10''$ ), the matter responsible for the CO radio line emission in an intermediate location ( $> \sim 10''$  and  $< \sim 19''$ ), and the dust component located further out ( $> \sim 19''$  and  $< \sim 21''$ ). The detached shell dust mass is derived to be of about  $2 \times 10^{-6} M_{\odot}$ , and the shell age is found to be of about 2200 years with a formation period of about 220 years.

Observations with the Hubble Space Telescope (HST) reported by Olofsson et al. (2010) also detected the spherically symmetric dust shell around R Scl, confirming that the mass loss responsible for creating the shell must have been remarkably isotropic. These observations do not cover the full detached shell, but a circular arc fitted to the bright limb suggests it not to be centered at the stellar position, with an offset of  $\sim 0.7''$  which would be justified by the presence of a binary companion. From the HST observations the shell has a radius of  $19.2''$  and a width of  $1.2''$ , which is consistent with a 1700 years old shell with a formation period of 100 years and a dust mass of  $3 \times 10^{-6} M_{\odot}$ .

Atacama Large Millimeter/submillimeter Array (ALMA) CO emission observations of R Scl, reported by Maercker et al. (2012), show a shell with a radius of  $18.5''$ , containing a spiral structure in its interior. The spiral is suggested to be generated by the presence of a binary companion. From the analysis of these data, no evidence for a deceleration of the shell was found, which is contrary to the current theory for the formation of the detached shells.

In this chapter we report the results from observations of the dust scattered light of the AGB stars R Scl and V644 Sco. As previously presented, the first one is a well-studied source, believed to be located at  $\sim 290$  pc from us (Knapp et al. 2003). It has a luminosity of  $4300 L_{\odot}$ , a present-day mass-loss rate of  $3 \times 10^{-7} M_{\odot} \text{ yr}^{-1}$  (Schöier et al. 2005), and the expansion velocity of the shell is found to be  $14.3$  km/s (Maercker et al. 2012). For the second case of our study, V644 Sco is reported to be at a distance of  $700$  pc if a luminosity of  $4000 L_{\odot}$  is adopted. Its mass-loss rate is  $5 \times 10^{-8} M_{\odot} \text{ yr}^{-1}$  and the expansion velocity of the shell is  $23$  km/s (Schöier et al. 2005). Although the existence of a detached shell around V644 Sco has been known since 1996 (Olofsson et al. 1996), it has never been imaged before and is much less well investigated than the shell surrounding R Scl. From models presented by

Schöier et al. (2005), the shell dust mass was estimated to be  $1.4 \times 10^{-4} M_{\odot}$ . The authors also derived that the radius of the shell is  $10.5''$ .

In Section 6.2, we present the details of our observations and in Section 6.3 the results. A discussion is made in Section 6.4 and the conclusions are shown in Section 6.5.

## 6.2 Observations and Data Reduction

We observed the AGB stars R Scl and V644 Sco with the ESO 3.6 m Telescope at the La Silla Observatory (Chile) and the visitor instrument PolCor. The observations were carried out in the same mission as described in Chapter 5. For a general description of the observations and data reduction process, see Section 5.2.

The targets were observed with a coronagraph of  $3''$  and  $6''$  in diameter in three optical bands:  $R$ ,  $V$ , and  $B$ . The observation details are shown in Table 6.1. The effective seeing, shown in the last column of this table, was derived from the FWHM of background stars in the total intensity images of V644 Sco. As no background stars are present in the images of R Scl, we present the maximum value of the seeing during the observations of that source. An improvement of 20%-30% over that value is expected in the images we present due the usage of the “lucky imaging” method.

## 6.3 Results

The AGB stars R Scl and V644 Sco are known to be surrounded by detached shells (e.g., Olofsson et al. 1996; Schöier et al. 2005). We observed these sources aiming to image the total intensity (Figs. 6.1 and 6.4 for R Scl and V644 Sco, respectively) and the dust scattered light (Figs. 6.2 and 6.5 for R Scl and V644 Sco, respectively) of the shells. These images were derived following the routine described in Chapter 5. The figures show the emission with  $\text{SNR} > 5$  (V644 Sco;  $B$  and  $V$  bands) and  $\text{SNR} > 7$  (R Scl;  $B$ ,  $V$ , and  $R$  bands and V644 Sco;  $R$  band). We masked out a region with  $4''$  of diameter in the center of the images observed with the coronagraph of  $3''$ , and a region with  $8''$  of diameter in the center of the



Table 6.1: Observation details

Source	F	CD (")	TFram	Sharp	FR0	Fr45	Fr90	Fr135	Exp (s)	EfS (")	Date (dd/mm/2011)
R Scl	<i>B</i>	3	3000	80%	2933	2952	2956	2920	0.1	<1.1	27/10
R Scl	<i>V</i>	3	3000	80%	2892	2440	1909	1918	0.04	<1.3	19/10
R Scl	<i>V</i>	6	6000	80%	5973	5983	5994	5997	0.04	<1.3	19/10
R Scl	<i>R</i>	3	3000	80%	2954	2978	2988	2984	0.04	<1.3	19/10
V644 Sco	<i>B</i>	3	1500	95%	1500	1500	1500	1500	0.1	1.0	27/10
V644 Sco	<i>V</i>	3	7500	80%	7420	7406	7377	7426	0.1	1.3	24/10 & 26/10
V644 Sco	<i>R</i>	3	15000	80%	11151	11137	11187	10831	*	1.3	24/10 & 26/10 & 27/10
V644 Sco	<i>R</i>	6	3000	80%	2887	2925	2881	2891	0.1	1.8	23/10

From left to right: Source name (Source), filter band (F), coronagraph diameter (CD), number of observed frames (TFram), sharpness criteria (Sharp), number of selected frames in each polarization direction (Fr0, Fr45, Fr90, Fr135), exposure time of a single frame (Exp), effective seeing (EfS), and date of observation (Date).

\*Observations with 0.04 s and 0.1 s were combined for this data set.

Table 6.2: AARP angle ranges

Source	FB	CD ( $''$ )	Q1 ( $^{\circ}$ )	Q2 ( $^{\circ}$ )	Q3 ( $^{\circ}$ )	Q4 ( $^{\circ}$ )
R Scl	<i>B</i>	3	35–55	125–145	240–250	305–325
R Scl	<i>V</i>	3	35–55	125–145	240–250	305–325
R Scl	<i>V</i>	6	35–55	125–145	240–250	305–325
R Scl	<i>R</i>	3	35–55	125–145	240–250	305–325
V644 Sco	<i>B</i>	3	26.5–30	126–128	203–210	293–300
V644 Sco	<i>V</i>	3	26.5–30	126–128	203–210	293–300
V644 Sco	<i>R</i>	3	26.5–30	126–128	203–210	293–300
V644 Sco	<i>R</i>	6	26.5–30	126–128	203–210	293–300

From column 1 to column 7: Source name (Source), filter band (FB), coronagraph diameter (CD), and the angle ranges of quadrants Q1, Q2, Q3, and Q4.

images observed with the coronagraph of  $6''$ . This was done to avoid not only the coronagraph region but also the region immediately close to it, which may suffer from image distortions due to the presence of the coronagraph. Moreover, one should take special caution regarding the interpretation and reliability of any emission close to the region that has been masked out. Polarization vectors, scaled in size to the lower limit of the polarization degree (see Chapter 5 for a discussion on why we derive the lower limit only), are shown overplotted on the polarized emission images. The polarized light images show, in gray scale, the region where the spider coronagraph is located. The polarization vectors originated in this region are not shown.

The AARP plots, derived from the figures mentioned in the previous paragraph, are shown in Figs. 6.3 and 6.6. The angle range considered for each quadrant is shown in Table 6.2. The spider area and background stars were avoided when defining the angle ranges. Note that spurious structures in the images (e.g., diffraction spikes) and clumpy regions in the source may affect the AARPs, in particular for zones with smaller radii.

### 6.3.1 R Scl

The detection of the detached shell is clear in the R Scl total intensity images (Figs. 6.1) in all three observed bands. In the  $B$  band the emission level of the shell is comparatively lower than in the  $V$  and  $R$  bands, but its presence is still evident. Additionally, the detached shell can also be identified in the AARP of the total intensity images (Figure 6.3, first column). These plots show that the shell is brighter in quadrant Q2 (blue curve), while in quadrants Q3 and Q4 (green and magenta curves) the shell is less bright. In other words, the detached shell is brighter in the north than in the south. This pattern is seen in all three bands. The detached shell appears as a filled disk in the total intensity images as emission from the whole three-dimensional structure of the shell contributes to the image. As a consequence, a deviation from the stellar PSF can be identified in the corresponding AARPs from  $\sim 9.5''$  to  $\sim 21''$ . This is easier to identify from the brighter AARP (blue curve, quadrant Q2) in the B and V bands.

In dust polarized light (Figure 6.2), the detached shell is also easily identified in all three observed bands, but now it appears as a ring-like structure. This is due to the fact that the radiation is strongly polarized when the angle between the star, the shell, and the observer is  $\sim 90^\circ$ . Therefore, the polarized images map the dust in a well-defined plane of the source that passes through the star. Notice that, again, the shell is brighter in quadrants Q1 and Q2, and the structure shows some clumps along the bright limb, with some areas where the emission is lower or absent (lower than the SNR mask). Specifically, notice the apparent gap in the limb of the shell in quadrants Q3 and Q4, suggesting a lower density of dust in those regions. Moreover, despite the fact that the polarized images map a well-defined plane, they still show the presence of dust also inside the shell. This is true even not considering the region close to the zone that has been masked out. Notice that the AARPs of these images (Figure 6.3, second column) show an increase of polarized emission for radii greater than  $\sim 10''$ , while the border of the shell is located much further out than that. It is also clear that the emission is brighter in quadrant Q2 and weaker in quadrant Q4. These radial profiles point to the extension of the shell up to  $\sim 21''$ .

The radial profiles of the polarization degree (Figure 6.3, third column) show that

in the  $R$  and in the  $V$  bands the peak of polarization goes from  $\sim 20\%$  in quadrant Q4 up to  $\sim 40\%$  in quadrant Q2, decreasing smoothly inwards and outwards from the bright limb of the shell. The polarization degree in the  $B$  band is lower and it peaks at  $\sim 15\%$  in quadrant Q2. We highlight that the polarization degree values that we derived correspond to lower limits.

### 6.3.2 V644 Sco

We detected a detached shell around V644 Sco in the  $V$  and  $R$  bands. In the total intensity images (Figure 6.4) the shell is visible in these two bands as a faint disk surrounding the star. The AARPs of the total intensity images (Figure 6.6, first column) show how the shell deviates from the PSF of the star, while the location of the shell is more prominent in the polarized intensity images (Figure 6.5). In the  $V$  and  $R$  bands polarized images with the coronagraph of  $3''$  in diameter, the shell looks like a well-defined ring and not much emission is seen from the region between the shell and the star. In the polarized image with the  $6''$  coronagraph, it is possible to notice more emission from inner regions and the ring is brighter in quadrants Q1 and Q3. However, some spurious artifacts are likely to be present in this image. Notice, for example, that the bright background star in quadrant Q2 is double peaked. Several attempts to improve the data reduction process in this data set were done, but these problems could not be solved. Therefore, the results from this image should be used with caution.

The AARPs of the polarized images in the  $V$  and  $R$  bands with the coronagraph with a  $3''$  diameter (Figure 6.4, second column, second and third lines) show a more pronounced profile for the detached shell around V644 Sco. Moreover, an offset between the AARP in quadrant Q4 and the AARPs of the other quadrants is seen. This is even more evident in the  $R$  band, where the peak of emission is shifted by  $\sim 1''$  between the red and magenta curves. However, we highlight that this value is lower than the effective seeing of the image, which is  $1.3''$ . The shell is located between  $\sim 7.5''$  and  $\sim 11''$  from the star, with the peaks in the different quadrants located between  $\sim 8.5''$  and  $\sim 9.5''$ .

The lower limit of the polarization degree of the shell around V644 Sco is signifi-

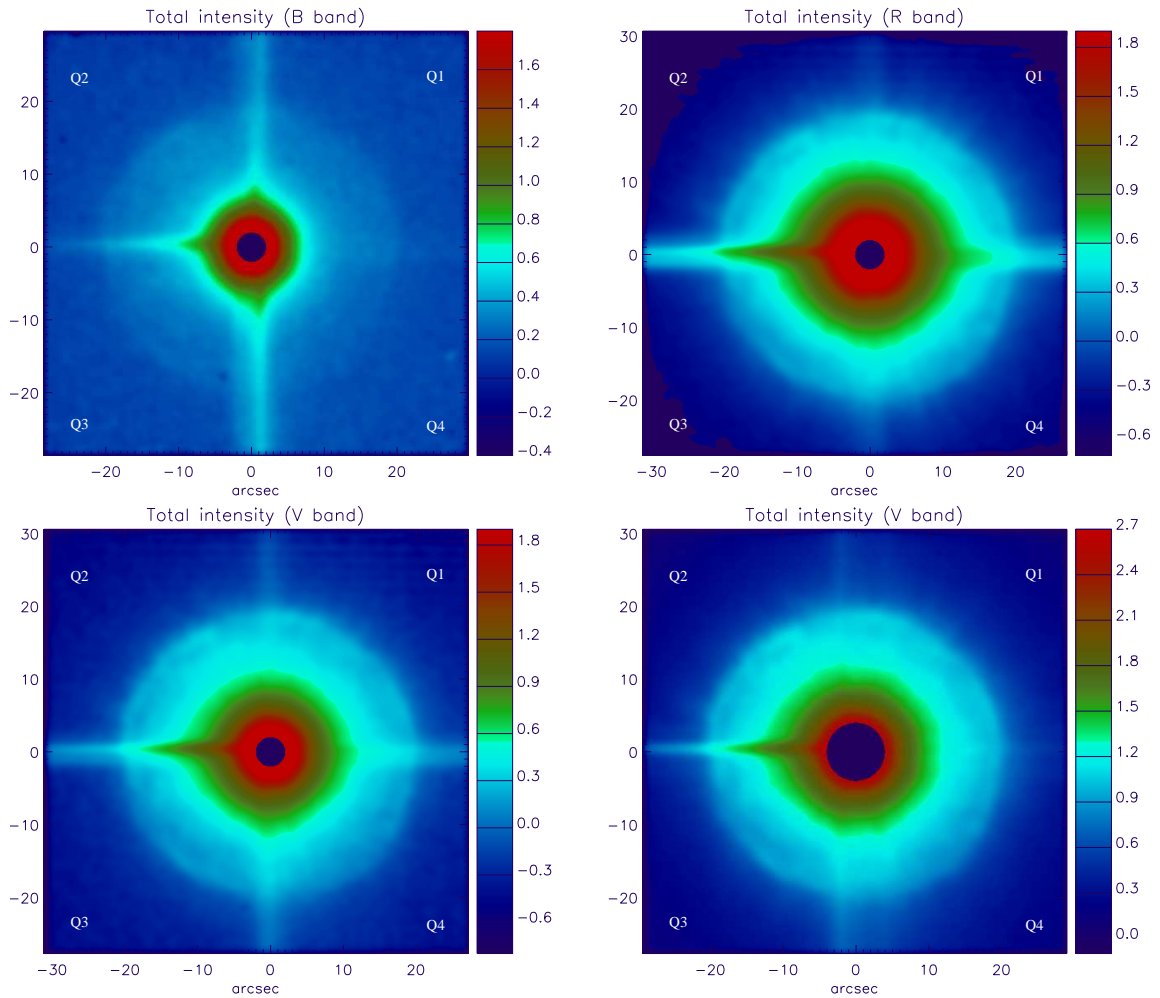


Figure 6.1: R Scl total intensity images in logarithmic scale in *B* (top left), *R* (top right), and *V* (bottom left and bottom right) bands. Both images on the top and the image on the bottom left were observed with a coronagraph with  $3''$  of diameter, and the image on the bottom right with a coronagraph of  $6''$  of diameter.

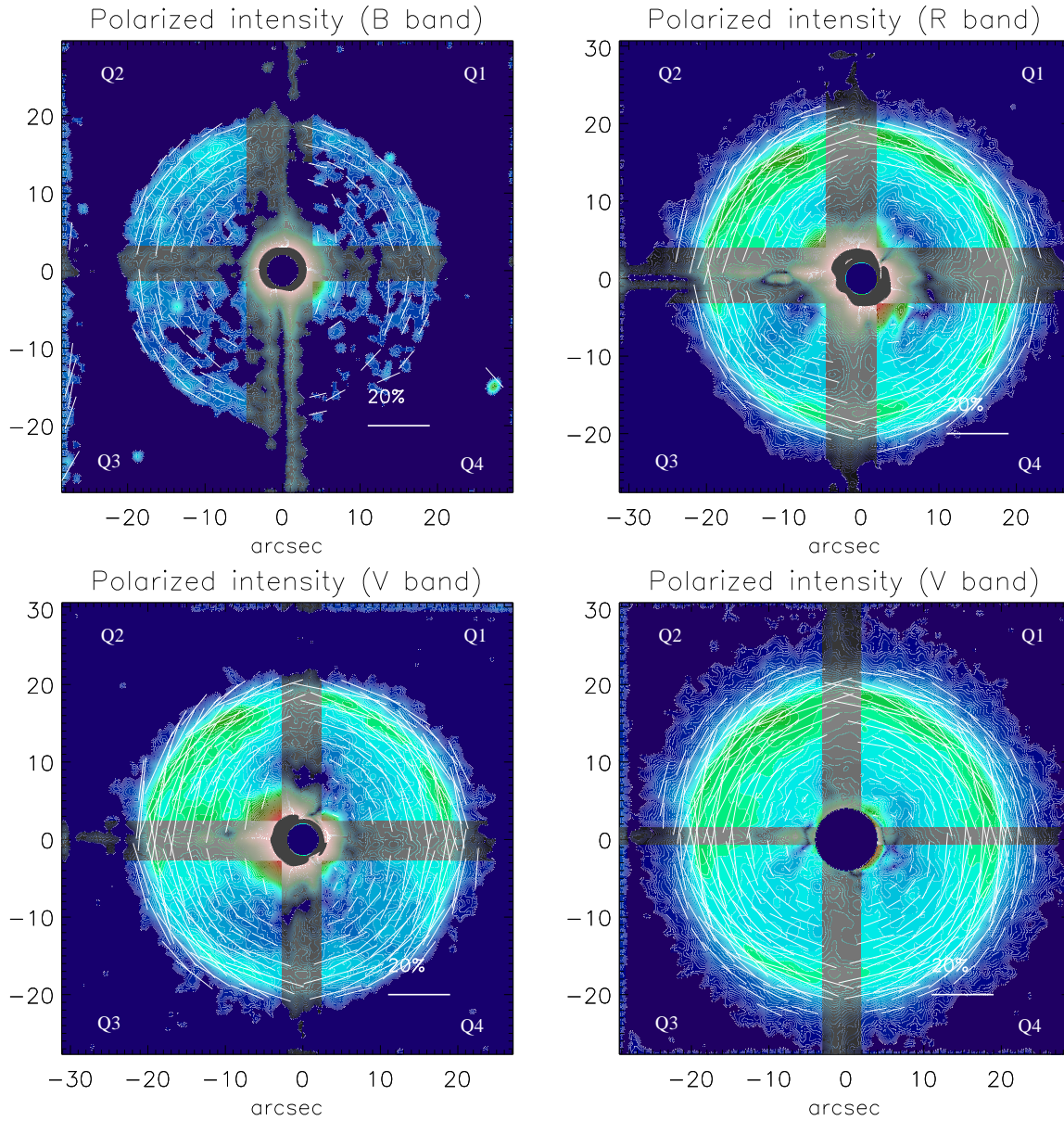


Figure 6.2: R Scl polarized light images in logarithmic scale in  $B$  (top left),  $R$  (top right), and  $V$  (bottom left and bottom right) bands. The white vectors show the polarization direction and their sizes are scaled with the lower limit of the polarization degree. Both images on the top and the image on the bottom left were observed with a coronagraph with  $3''$  of diameter, and the image on bottom right with a coronagraph of  $6''$  of diameter.

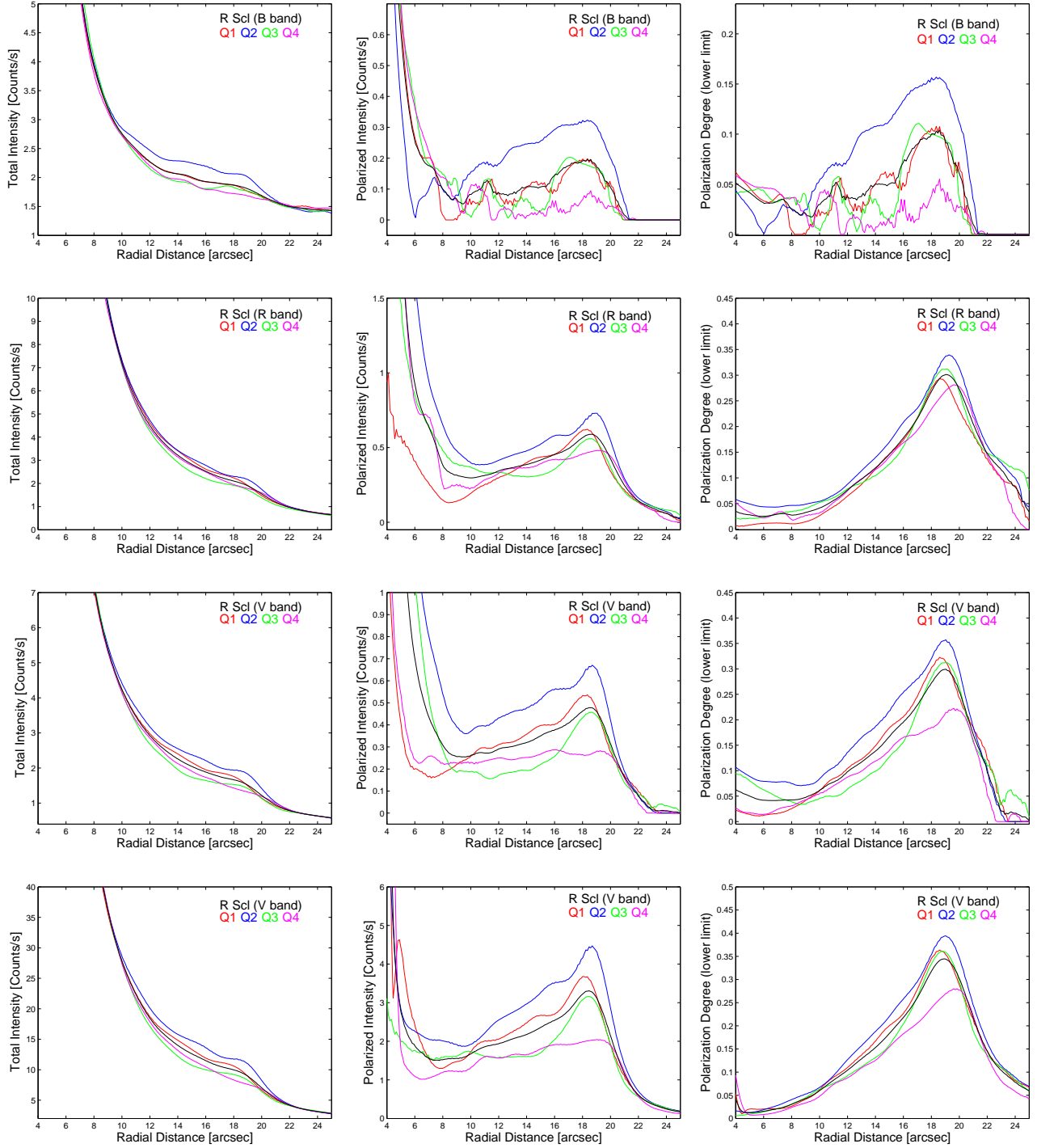


Figure 6.3: Radial profile of R Scl observations. The colored lines refer to the profiles over four different directions, averaged over a given angle aperture. Each one of these four profiles corresponds to a different quadrant. The black line is the mean of the four colored lines. The top plots show the radial profiles in the the  $B$  band, the ones in the second line correspond to the  $R$  band, and the ones on the third and last lines are from the the  $V$  band. From left to right, the plots correspond to the total intensity, polarized intensity, and the polarization degree (lower limit) images.

cantly higher in the  $R$  band than in the  $V$  band. While the peak of the polarization degree in the  $R$  band goes from  $\sim 4.5\%$  to  $\sim 8\%$  in the different quadrants, in the  $V$  band it varies from  $\sim 2.5\%$  to less than  $\sim 4.5\%$  in the different quadrants.

## 6.4 Discussion

Fitting a Gaussian to the AARP can give a reasonable result for the radius and the width of the shell, and this method is consistent with the results obtained by a model of the shell (Mauron & Huggins 2000). However, Maercker et al. (2010) claim that a Gaussian fit to the peak and tail of the shell can overestimate the width by  $\sim 20\%$  and underestimated the radius of the shell by  $\sim 8\%$  due to a limb-brightening of the inner part of the shell. Despite the fact that a more robust method to obtain these quantities would be to derive theoretical AARPs, here we simply fit a Gaussian to the mean radial profile of the shell (Figs. 6.7 and 6.8), keeping in mind that the radius and width are likely to be over/underestimated by the factors mentioned above. A more detailed investigation of the radius and width of the shell will be presented in an upcoming paper by Maercker et al. (in prep.).

### 6.4.1 R Scl

From previous works the detached shell surrounding R Scl was found to have a radius between  $18.5''$  and  $21''$ , a width of between  $1.2''$  and  $2''$ , a dust mass between  $2 \times 10^{-6} M_{\odot}$  and  $3.2 \times 10^{-5} M_{\odot}$ , an age between 1700 years and 2200 years, a formation period between 100 and 220 years, and an expansion velocity between  $14.3 \text{ km/s}$  and  $15.5 \text{ km/s}$  (González Delgado et al. 2003; Schöier et al. 2005; Olofsson et al. 2010; Maercker et al. 2012). In the following, we will assume a distance of 290 pc (Knapp et al. 2003) and a shell expansion velocity of  $14.3 \text{ km/s}$  (Maercker et al. 2012).

We fit Gaussians (Figure 6.7) to the average AARP of the polarized images in each band to identify the position of the peak emission and the width of the shell. The average result from the four images gives a radius of  $\sim 18.1''$  or  $\sim 5250 \text{ AU}$ . Such radius implies an age of  $\sim 1750$  years for the shell. We highlight that these results are



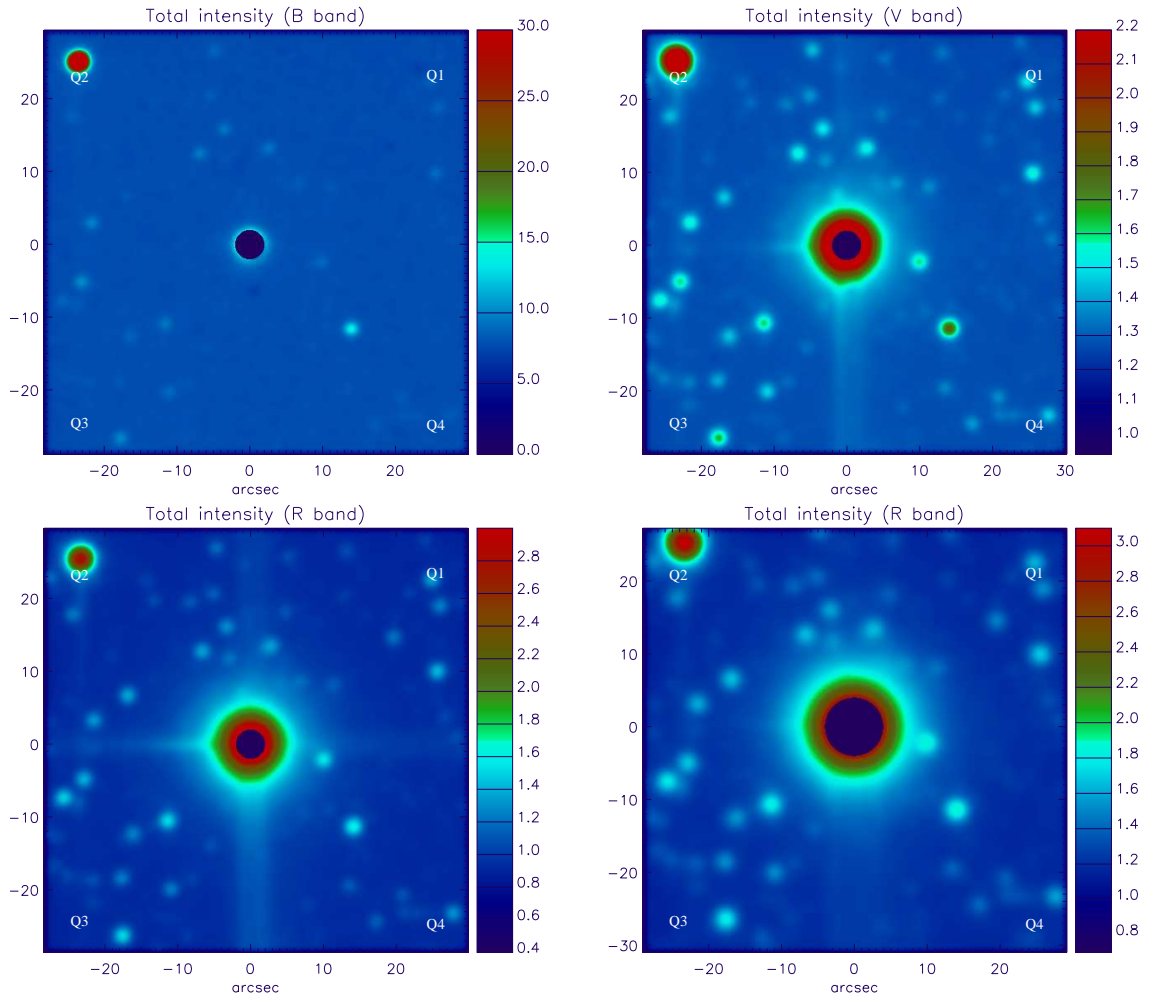


Figure 6.4: V644 Sco total intensity images. The top left image corresponds to the  $B$  band in linear scale. The other three images are shown in logarithm scale, where the  $V$  band image is shown on top right and the  $R$  images are on the bottom. The bottom right image was taken with a coronagraph of 6'' of diameter, and the remaining three with a coronagraph of 3'' of diameter.

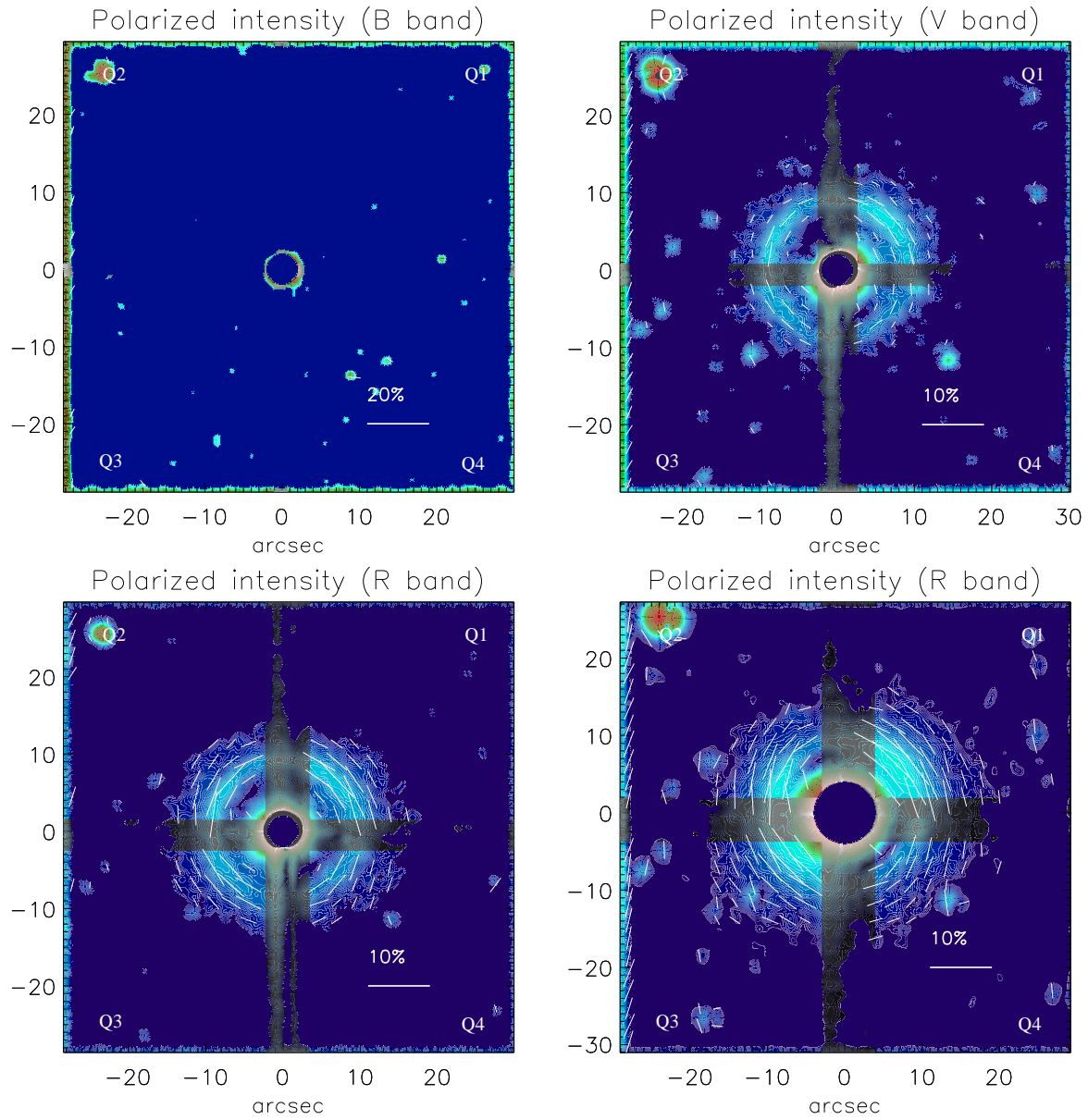


Figure 6.5: V644 Sco polarized light images in logarithmic scale. The white vectors show the polarization direction and their sizes are scaled with the lower limit of the polarization degree. The top left image corresponds to the *B* band, the *V* band image is shown on top right and the *R* band images are on the bottom. The bottom right image was taken with a coronagraph of 6'' of diameter, and the other three with a coronagraph of 3'' of diameter.

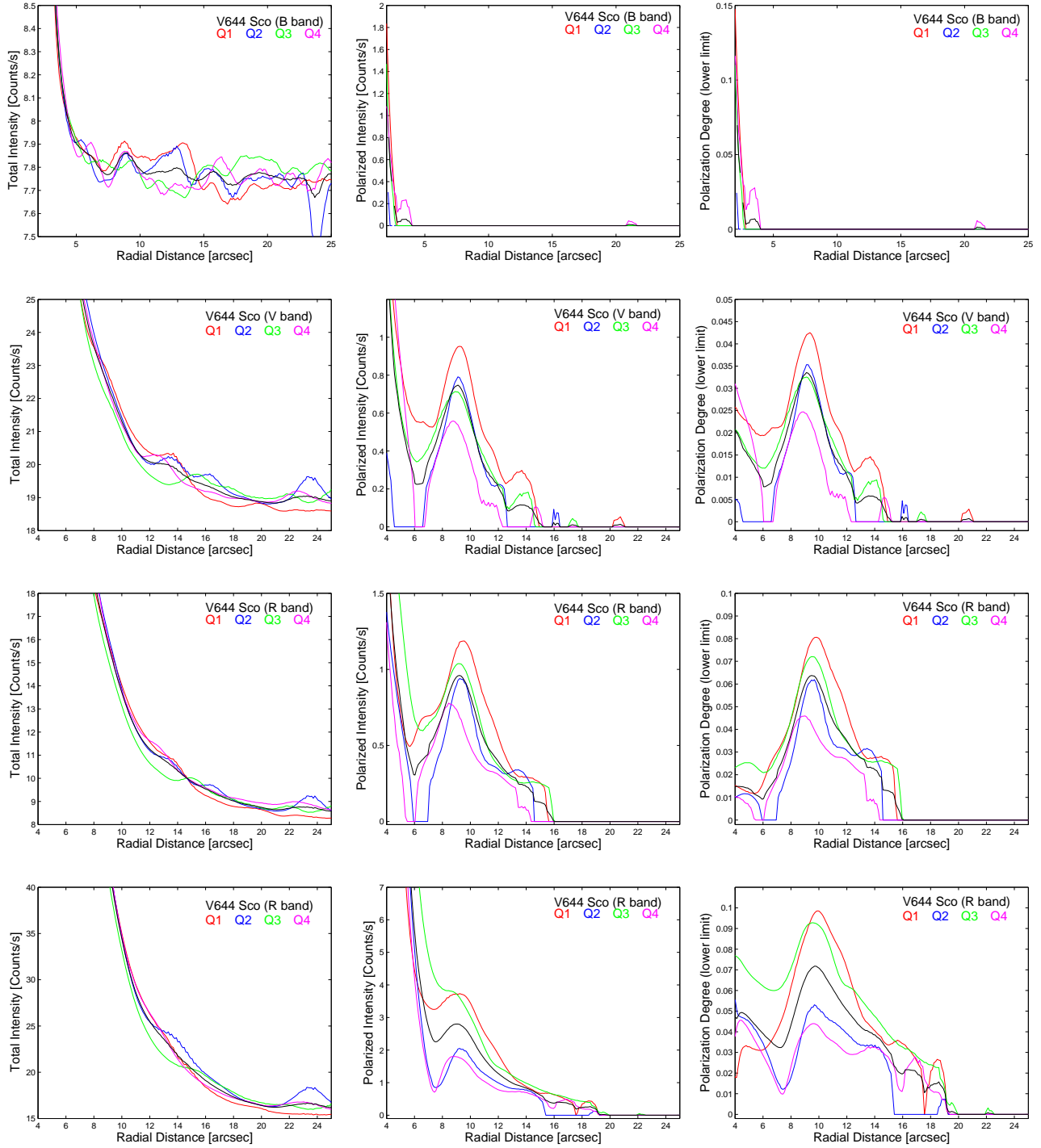


Figure 6.6: Radial profile of V644 Sco observations. The colored lines refer to the profiles over four different directions averaged over a given angle aperture. Each one of these four profiles corresponds to a different quadrant. The black line is the mean of the four colored lines. From top to bottom, we show the plots of  $B$ ,  $V$ , and  $R$  (with the 3'' and 6'' diameter coronagraphs) bands. From left to right, the plots correspond to the total intensity, polarized intensity, and the polarization degree (lower limit) images.

likely to be underestimated by a factor of  $\sim 8\%$  (Maercker et al. 2010). The results from each individual Gaussian fit are shown in Table 6.3 and, considering that they are underestimated by  $\sim 8\%$ , they are consistent with results from the literature.

The width of the shell is not constant in all directions and different values are found in the different quadrants. As we fit a Gaussian to the averaged AARP of all four quadrants, the derived FWHM is expected to be broadened, leading to an upper limit of the shell width. On top of that, the FWHM overestimates the shell width by a factor of  $\sim 20\%$  (Maercker et al. 2010). Our results point to a width of the shell of  $\sim 4.7''$ , which would correspond to a time of formation of  $\sim 450$  years (see Table 6.3 for the results from each individual Gaussian fit). However, we highlight that the creation duration is not the only aspect to influence the width of the shell (e.g. the temperature of the gas is also an important factor). Moreover, the shell width may vary along its evolution (Mattsson et al. 2007), which is not predicted by Steffen & Schönberner (2000). Therefore, the results for the time of formation of the shell should be taken as a rough estimate. Our result for the width of the shell is higher than the ones from the literature. The work that reports the smallest value for the width of the shell around R Scl is the one that uses the data from the HST. Comparing our results of the width of the shell with the observations from the HST ( $1.3''$ ; Olofsson et al. 2010), we assign the difference to (i) the different width of the shell at different positions, (ii) the fact that our Gaussian fit likely overestimates the width by  $\sim 20\%$ , (iii) the fact that the observation from Olofsson et al. (2010) only cover  $\sim 1/3$  of the shell, being dominated by a bright arc along the shell. In combination with item (iii), we highlight that our observations show an apparent flattening of the shell in the south, which could lead to a larger FWHM.

We searched for an offset between the center of the shell and the position of the star and found it to be between  $0.3''$  and  $0.5''$  in the images from the different bands. The direction of the measured offset is not the same in each one of the four images, but it is always approximately toward east. This offset can be compared with the value of  $0.7''$  found by Olofsson et al. (2010). Even though the presence of an offset is expected for this source, as the observations with ALMA suggest the presence of a binary companion to this AGB star, our measurements are not conclusive, as the value of  $0.3''$ – $0.5''$  is likely to be smaller than the effective seeing of our images.

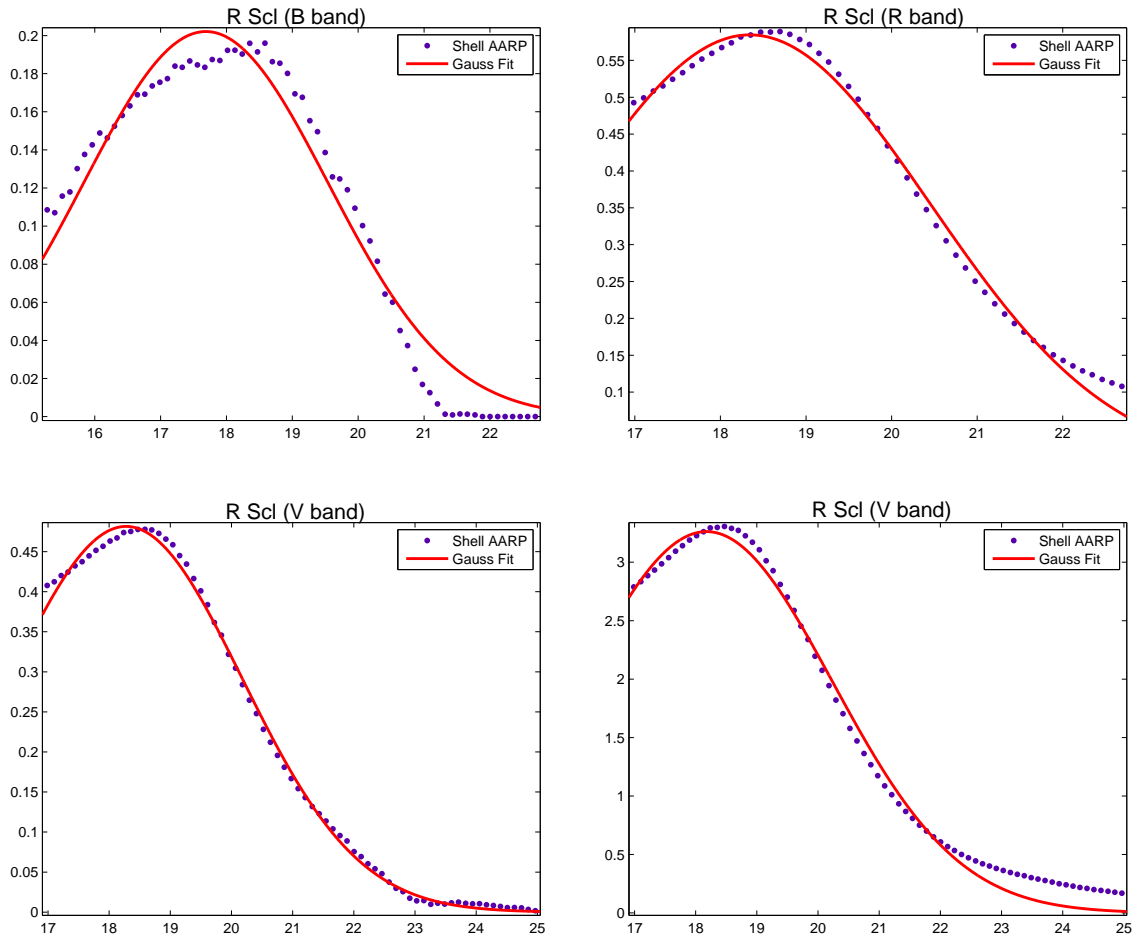


Figure 6.7: Gaussian fit (red continuous line) to the averaged AARP of the R Scl polarized images (blue dots). On the top the plots of the B and R bands are shown. In the bottom the plot of the V band with the coronagraph with 3" (left) and 6" (right) of diameter are presented.

Table 6.3: Results given by each individual Gaussian fit.

Source	FB	CD (")	Ras (")	Rau (AU)	Age (yrs)	Wd (")	Wdau (AU)	FT (yrs)
R Scl	<i>B</i>	3	17.7*	5130*	1700*	4.4**	1270**	420**
R Scl	<i>V</i>	3	18.3*	5300*	1760*	4.5**	1300**	430**
R Scl	<i>V</i>	6	18.2*	5270*	1750*	4.8**	1400**	470**
R Scl	<i>R</i>	3	18.3*	5320*	1760*	5.0**	1440**	480**
V644 Sco	<i>B</i>	3	—	—	—	—	—	—
V644 Sco	<i>V</i>	3	9.0*	6320*	1300*	3.8**	2670**	550**
V644 Sco	<i>R</i>	3	9.2*	6440*	1330*	4.0**	2790**	570**
V644 Sco	<i>R</i>	6	9.0*	6280*	1300*	5.2**	3640**	750**

From column 1 to column 7: Source name (Source), filter band (FB), coronagraph diameter (CD), radius in arcsecs (Ras) and in AU (Rau), age of the shell (Age), width of the shell in arcsecs (Wdas) and in AU (Wdau).

\* Likely to be underestimated by  $\sim 8\%$ .

\*\* Likely to be overestimated by  $\sim 20\%$ .

Finally, we highlight that the images reported here are the first images with high spatial resolution of the entire detached shell of dust around R Scl.

## 6.4.2 V644 Sco

The existence of a detached shell surrounding V644 Sco was first suggested by Olofsson et al. (1996), who performed CO observations for a sample of AGB stars. However, such a structure has never been imaged until the present date. From molecular line modeling, Schöier et al. (2005) derived that the expansion velocity of the shell is 23 km/s. We will adopt this velocity and a distance of 700 pc from us to this source for the discussion in the next paragraphs (Schöier et al. 2005).

Following the same procedure performed on the R Scl data, we fit Gaussians to the averaged AARP of the detached shell detected in the dust scattered images of V644 Sco (Figure 6.8) to identify the position of the peak emission and the width of the shell. This analysis was done only for the images in the R and V bands, as the shell was not detected in the B band. We present the results from each

individual Gaussian fit in Table 6.3. We highlight that these results are likely to be underestimated by  $\sim 8\%$  (Maercker et al. 2010), and that the results from the observation in the R band with the coronagraph with  $6''$  of diameter should be taken with caution, as discussed before. Therefore, not considering the estimates from this image, on average we estimate a radius of  $\sim 9.1''$  or 6400 AU, implying an age of  $\sim 1300$  years for the shell, which makes this shell younger than the one around R Scl.

The width of the shell, given by the average of the FWHM of the Gaussian fits is of  $\sim 3.9''$  (not considering the estimate from the R band image with the coronagraph with  $6''$  of diameter). This corresponds to a time of formation of  $\sim 560$  years, if we directly associate the shell width with the creation duration of the shell. See Table 6.3 for the results from each individual Gaussian fit. Again, notice that these results are likely to be overestimated by  $\sim 20\%$  (Maercker et al. 2010).

Finally, we emphasize that the shell is well centered on the star. We measured an offset of the detached shell of about  $0.2''$ , which is significantly smaller than the effective seeing of the images. Therefore, only further observations could confirm whether such an offset is in fact real or not. On this subject, we highlight that no signs for a binary companion were ever found for this source.

### 6.4.3 R Scl versus V644 Sco: The Region Between the Star and the Shell

The comparison of the shells around R Scl and V644 Sco is not straightforward, as the angular size of the shell around R Scl is bigger than the one around V644 Sco. This difference in angular size makes the coronagraph block and contaminate a bigger area in the images of V644 Sco than in the images of R Scl. We believe that this difference in the quality of the images may be the cause of the detection of more emission from the region between the star and the shell in the dust polarized images of R Scl, in comparison to V644 Sco.

The polarized intensity images of R Scl indicate that the region between the star and the shell is not free from emission in all three bands we observed. For V644 Sco the analysis of the polarized image in the *R* band with the coronagraph of  $6''$  of diameter is more complicated, as this image may contain spurious artifacts

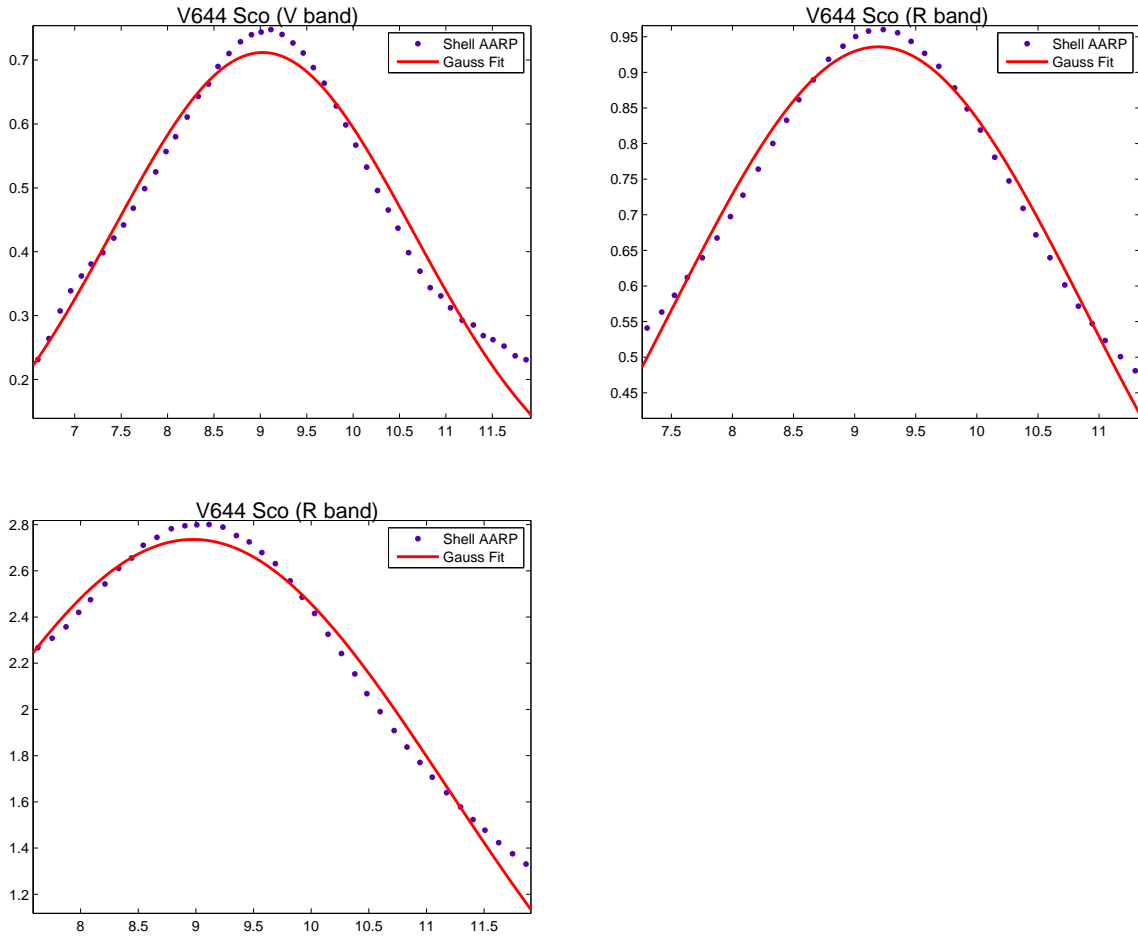


Figure 6.8: Gaussian fit (red continuous line) to the averaged AARP of the V644 Sco polarized images (blue dots). On the top the plots of the V band and of the R band with the coronagraph of 3" of diameter are shown. In the bottom the plot of the R band with the coronagraph with 6" of diameter is presented.



as discussed in Section 6.3.2. However, in the  $V$  and  $R$  bands observed with the coronagraph of  $3''$  of diameter, the region between the star and the shell looks emptier than the corresponding region in R Scl. Moreover, the AARPs of V644 Sco are significantly sharper in the shell region than the ones of R Scl.

If the non-detection of a gradual intensity decrease in the region between the star and the shell in V644 Sco is not an observing effect, but reflects an intrinsic property of the source, the immediate conclusion would be that this region is significantly more depleted of dust in V644 Sco than in R Scl. If this is true, we suggest that the spiral structure of molecular gas detected in R Scl (Maercker et al. 2012) could be related to the dust emission we detected in the inner regions of in this source. Moreover, we highlight that the present-day mass-loss rate in R Scl ( $3 \times 10^{-7} M_{\odot} \text{ yr}^{-1}$ ) is higher than in V644 Sco ( $5 \times 10^{-8} M_{\odot} \text{ yr}^{-1}$ ; Schöier et al. 2005).

## 6.5 Conclusion

We observed the AGB stars R Scl and V644 Sco with the ESO 3.6 m Telescope in the  $B$ ,  $V$ , and  $R$  bands, obtaining the total intensity and the dust scattered images of the sources and the detached shells that surround them. The detached shells were successfully detected in total intensity and dust scattered images in the  $B$ ,  $V$ , and  $R$  bands for R Scl, and in the  $V$  and  $R$  bands for V644 Sco.

The observations of R Scl show a shell that is brighter in the north than in the south. The region between the star and the shell is not free from emission and from the polarized images one can identify the presence of dust from  $\sim 10''$  to  $\sim 21''$ . The width of the shell around R Scl was derived from the FWHM of Gaussian fits to the radial profiles of the polarized image. Our results agree with a width of  $4.7''$ , implying a formation time of  $\sim 450$  years for the shell. We also used the Gaussian fits to derive the position of the peak of emission of the shell. This position was used to determine the shell radius, that we found to be of about  $18.1''$  or  $5250$  AU, implying a shell age of  $\sim 1750$  years. However, we highlight that the width of the shell is likely overestimated by  $\sim 20\%$ , and the radius is likely underestimated by  $\sim 8\%$ . The lower limit for the polarization degree was found to be from  $\sim 20\%$  and

$\sim 40\%$  in  $R$  and  $V$  bands, peaking at  $\sim 15\%$  in  $B$  band. The polarization vectors follow a centrosymmetric pattern.

It was the first time that the detached shell around V644 Sco was imaged, and the results show a well-defined shell around the star. The shell is brighter in the northwest and less bright in the southwest, and it is found to be well centered on the star. We derived the detached shell around V644 Sco to have a radius of  $9.1''$  or 6400 AU. As a consequence, the age of the shell was inferred to be 1300 years, making this structure younger than the shell around R Scl. Its width of  $3.9''$  implies a formation time of 560 years. Again we expect the results for the radius (width) of the shell to be underestimated (overestimated) by  $\sim 8\%$  ( $\sim 20\%$ ). The lower limit of the polarization degree was observed to be between  $\sim 4.5\%$  and  $\sim 8\%$  in  $R$  band, and from  $\sim 2.5\%$  up to less than  $\sim 4.5\%$  in  $V$  band. The direction of polarization was found to follow the shell in a centrosymmetric pattern.

# Chapter 7

## Conclusions and perspectives

*In this chapter the main conclusions of this work are summarized. Moreover, an overview on a research project that I plan to perform after my PhD is given. This project is in the same line of investigation as this thesis and will provide complementary results to the ones presented in Chapters 3 and 4.*

### 7.1 Conclusions

We investigated the change of morphology that takes place in the late phases of the evolution of stars with initial masses between 0.8 and 8  $M_{\odot}$ . In Chapters 1 and 2 the stellar evolution of low- and intermediate-mass stars and the state of art of theories to explain the asymmetries on evolved stars were reviewed. Also in Chapter 1, I described the observation techniques that were used in this work, and discussed the nature of the radiation investigated in this thesis. In Chapter 3 to 6 the results of my research were reported and discussed. In the following paragraphs these results are summarized.

The pre-PN OH231.8+4.2 (Rotten Egg Nebula; Calabash Nebula) is an evolved star with a binary companion. This bipolar nebula has a massive outflow with unknown origin. In Chapter 3, the detection of 30  $H_2O$  masers toward this source is reported. The masers are moving away from the stellar pair in the direction of the collimated outflow with a velocity of  $21 \pm 11$  km/s. Three of the observed masers

present linear polarization and we assign the scatter between the polarization angles to be either caused by turbulence or to trace tangent points of a toroidal magnetic field. We detected circular polarization in the two brightest masers, one of them located to the north and the other one to the south of the stellar pair. From a model fit of the Stokes V spectra of these two masers we derived magnetic field strengths of  $44\pm 7$  mG and  $-29\pm 21$  mG, respectively in the north and south regions of the source. Assuming a global toroidal field, we extrapolated the magnetic field strength to be 2.5 G on the surface of the central star. The pre-PN OH231.8+4.2 is the first evolved star known to be in a binary system in which the presence of a magnetic field is confirmed toward the circumstellar envelope.

The H<sub>2</sub>O masers around four AGB stars were also analyzed, as reported in Chapter 4. Although no masers were detected surrounding AP Lyn, several ones were observed toward IK Tau (85 features, located between 10.1 and 29.2 AU from the star), RT Vir (91 features, located between 2.4 and 18.0 AU from the star), and IRC+60370 (62 features, located between 5.5 and 53.0 AU from the star). We identified a structured spatial distribution of maser velocities around IK Tau and discussed a similar pattern in RT Vir. Linear polarization was detected in nine masers toward RT Vir, and nine more around IRC+60370. Significant circular polarization detection was reported in 11 masers of which three have been found in IK Tau and RT Vir and four in IRC+60370. From these detections we derived magnetic field strengths between  $47\pm 3$  mG and  $331\pm 82$  mG in the H<sub>2</sub>O maser region of these targets, increasing the number of AGB stars around which magnetic fields have been measured in the H<sub>2</sub>O maser region by a factor larger than two. We investigated the geometry of the observed magnetic fields by inferring their dependence with respect to the distance to the star. However, there is not enough data available in the literature for a conclusive statement. With the geometry of the field unknown, we investigated the field strength at the surface of the star assuming toroidal, poloidal, and dipole geometries. If a toroidal field is assumed, the field strength extrapolated to the surface of the stars is of a few Gauss. In case of a poloidal field our results are consistent with fields of a few tens of Gauss on the stellar surface. Finally, the dipole geometry results in fields with tens up to a couple of thousands Gauss on the surface of the stars. We also found that the measured

magnetic energy density dominates over typical values of the thermal and kinematic energy densities on evolved stars, what supports the hypothesis that the magnetic fields can indeed play a significant role in the shaping process of AGB stars and Planetary Nebulae.

We imaged the dust CSE of four AGB stars and one red supergiant by observing the light scattered by the dust in the envelopes of the stars. In Chapter 5, the asymmetries that we detected in the circumstellar envelope of IK Tau, and the complex morphology observed in the nebula that surrounds the RSG VY CMa are reported. The images of IK Tau show a CSE that extends up to  $\sim 15''$  in the R band, and the image of the dust scattered light reveals a global elliptical morphology. The presence of a central waist is discussed. An elongation with an extension of  $\sim 12''$  is reported from the faint total intensity image in the V band. The nebula around VY CMa extends up to  $20.5''$  in the R band and up to  $17''$  in the V band. These results show that the nebula around VY CMa is more than twice as extended as it was previously reported. A puzzling pattern was found for the direction of the polarization vectors in the envelope of this source. Such pattern is seen in both, the R and the V bands.

In Chapter 6 the observations of the circumstellar envelopes of the AGB stars R Scl and V644 Sco are discussed. These two sources present detached shells surrounding the stars and we imaged the shells in total intensity and in dust scattered light in the B, V, and R bands. We observed the shell surrounding R Scl to be brighter in the north than in the south. The region between the shell and the star is not free from emission in the dust scattered images, suggesting that dust might be present from  $\sim 10''$  to  $\sim 21''$  from the star. We derived an average shell radius of  $\sim 18.1''$  corresponding to 5250 AU, implying the shell to be  $\sim 1750$  years old. We discuss that these results are likely underestimated by  $\sim 8\%$ . From the FWHM of Gaussian fits to the averaged shell radial profiles of the dust scattered images we derived an averaged shell width of  $4.7''$ , suggesting a shell formation time of about 450 years. We highlight that the FWHM of a Gaussian fit is likely to overestimate the width of the shell by  $\sim 20\%$ . Moreover, the average of the radial profile of the shell over different directions might cause the shell to be smudged out and, since the width is not constant throughout the shell, it would also act to overestimate

the shell width. For the first time, the shell around V644 Sco was imaged and the results show a well-centered shell. The dust polarized images show that the region between the star and the shell in this source is significantly less bright than the corresponding region in R Scl. Although a comparison between the sources is not straightforward due to the different size scales of the shell on the sky, we suggest that V644 Sco could be depleted of dust in the region between the star and the shell. The measured radius of the shell is  $\sim 9.1''$  or 6400 AU, suggesting a shell age of about 1300 yrs. From the FWHM of Gaussian fits we derived that the shell width is  $3.9''$ , suggesting a shell formation time of 560 years. Also for V644 Sco, we highlight that our result for the radius is likely underestimated by  $\sim 8\%$  and the width result is likely overestimated by  $\sim 20\%$ .

## 7.2 Perspectives

In Section 4.4.5 the geometry of magnetic fields around AGB stars is discussed. To further investigate that topic it is necessary to infer the dependence of the magnetic field with respect to the distance to the star. This analysis requires the observation of different maser species from which we can derive the field strength in different distances to the star. I prepared an observing proposal to the e-MERLIN interferometer, aiming to detect linear and circular polarization in OH masers around five AGB stars: IK Tau, RT Vir, U Ori, W Hya, and U Her. This investigation will add data points to Figure 4.5 of this thesis, helping us to have a more complete view on the geometry of magnetic fields around AGB stars. The e-MERLIN observing proposal, under the code CY1025, was granted with observing time, and the observations are planned to be carried out in the second semester of 2014.

# Bibliography

- Amiri, N., Vlemmings, W., van Langevelde, H. J. 2011, *A&A*, 532, 149
- Bains, I., Cohen, R. J., Louridas, A., Richards, A. M. S., Rosa-González, D., Yates, J. A. 2003, *MNRAS*, 342, 8
- Balick, B., Frank, A. 2002, *ARA&A*, 40, 439
- Bjorkman, J. E., Cassinelli, J. P. 1993, *ApJ*, 409, 429
- Blackman, E. G. 2009, *IAUS*, 259, 35
- Boboltz, D. A., Diamond, P. J. 2005, *ApJ*, 625, 978
- Bond, H. E. 1979, *IAU Colloquium 53, White Dwarfs and Variable Degenerate Stars*, ed. H. M. Van Horn & V. Weidemann, 266
- Bond, H. E., Ciardullo, R., Meakes, M. G. 1992, *IAUS*, 151, 517
- Bond, H. E. 1995, *Annals of the Israel Physical Society*, vol. 11, ed. A. Harpaz & N. Soker, 61
- Bond, H. E. 2000, *ASP Conference Series*, 199, ed. J. H. Kastner, N. Soker, & S. Rappaport, 115
- Bowers, P. F., Johnston, K. J., de Vegt, C. 1989, *ApJ*, 340, 479
- Bujarrabal, V., Castro-Carrizo, A., Alcolea, J., Sánchez Contreras, C. 2001, *A&A*, 377, 868
- Cantiello, M., Mankovich, C., Bildsten, L., Christensen-Dalsgaard, J., Paxton, B. 2014, *ApJ*, 788, 93

- Castro-Carrizo, A., Quintana-Cacaci, G., Neri, R., Bujarrabal, V., Schöier, F. L., Winters, J. M., Olofsson, H., Lindqvist, M., Alcolea, J., Lucas, R., Grewing, M. 2010, *A&A*, 523, 59
- Choi, Y., Hirota, T., Honma, M., Kobayashi, H., Bushimata, T., Imai, H., Iwadate, K., Jike, T., Kamenno, S., Kameya, O., Kamohara, R., Kan-Ya, Y., Kawaguchi, N., Kijima, M., Kim, M. K., Kuji, S., Kurayama, T., Manabe, S., Maruyama, K., Matsui, M., Matsumoto, N., Miyaji, T., Nagayama, T., Nakagawa, A., Nakamura, K., Oh, C. S., Omodaka, T., Oyama, T., Sakai, S., Sasao, T., Sato, K., Sato, M., Shibata, K. M., Tamura, Y., Tsushima, M., Yamashita, K. 2008, *PASJ*, 60, 1007
- Choi, Y. K., Brunthaler, A., Menten, K. M., Reid, M. J. 2011, *IAUS*, 287, 407
- Clayton, D. 1983, *Principles of Stellar Evolution and Nucleosynthesis*, University of Chicago Press
- Colomer, F., Reid, M. J., Menten, K. M., Bujarrabal, V. 2000, *A&A*, 355, 979
- Cohen, R. J., 1987, *IAUS*, 122, 229
- Corradi, R. L. M., Schwarz, H. E. 1995, *A&A*, 293, 871
- Danchi, W. C., Bester, M., Degiacomi, C. G., Greenhill, L. J., Townes, C. H. 1994, *AJ*, 107, 1469
- De Beck, E., Decin, L., de Koter, A., Justtanont, K., Verhoelst, T., Kemper, F., Menten, K. M. 2010, *A&A*, 523, 18
- De Marco, O. 2006, *IAUS*, 234, 111
- De Marco, O., Hillwig, T. C., Smith, A. J. 2008, *AJ*, 136, 323
- De Marco, O. 2009, *PASP*, 121, 316
- De Marco, O., Soker, N. 2011, *PASP*, 123, 402
- Decin, L., Hony, S., de Koter, A., Justtanont, K., Tielens, A. G. G. M., Waters, L. B. F. M. 2006, *A&A*, 456, 549
- Decin, L., De Beck, E., Brünken, S., Müller, H. S. P., Menten, K. M., Kim, H., Willacy, K., de Koter, A., Wyrowski, F. 2010, *A&A*, 516, 69
- Dennis, T. J., Frank, A., Blackman, E. G., De Marco, O., Balick, B., Mitran, S. 2009, *ApJ*, 707, 1485



- Desmurs, J. -F., Alcolea, J., Bujarrabal, V., Sánchez Contreras, C., Colomer, F. 2007, *A&A*, 468, 189
- Dorfi, E. A., Hoefner, S. 1996, *A&A*, 313, 605
- Draine, B. T. 2003, *ApJ*, 598, 1017
- Elitzur, M. 1992, *ARA&A*, 30, 75
- Etoka, S., Lagadec, E., Zijlstra, A. A., Chesneau, O., Richards, A. M. S., Matsuura, M. 2008, *Proceedings of Science*, 63
- Etoka, S., Zijlstra, A., Richards, A. M., Matsuura, M. Lagadec, E. 2009, *ASPC*, 404, 311
- Faraday, M. 1845, *Faraday's Diary of Experimental Investigation*, IV
- Frank, A. 1995, *AJ*, 110, 2457
- Frank, A., De Marco, O., Blackman, E., Balick, B. 2007, *arXiv:0712.2004*
- Gail, H.-P., Sedlmayr, E. 1986, *A&A*, 166, 225
- Gail, H.-P., Sedlmayr, E. 1987, In: *Physical processes in interstellar clouds*, *Proceedings of the NATO Advanced Study Institute*, Dordrecht, D. Reidel Publishing Co., 275
- García-Díaz, M. T., López, J. A., Richer, M. G., Steffen, W. 2008, *ApJ*, 676, 402
- García-Segura, G., Langer, N., Różyczka, M., Franco, J. 1999, *ApJ*, 517, 767
- García-Segura, G., López, J. A., Franco, J. 2005, *ApJ*, 618, 919
- García-Segura, G. 2006, *IAUS*, 234, 297
- García-Segura, G., Villaver, E., Langer, N., Yoon, S.-C., Manchado, A. 2014, *ApJ*, 783, 74
- Goldreich, P., Keeley, D. A., & Kwan, J. Y. 1973, *ApJ*, 179, 111
- Gómez, Y., Rodríguez, L. F. 2001, *ApJ*, 557, 109
- González Delgado, D., Olofsson, H., Schwarz, H. E., Eriksson, K., Gustafsson, B. 2001, *A&A*, 372, 885
- González Delgado, D., Olofsson, H., Schwarz, H. E., Eriksson, K., Gustafsson, B., Gledhill, T. 2003, *A&A*, 399, 1021

- Gorny, S. K., Stasińska, G., Tyłenda, R. 1997, *A&A*, 318, 256
- Habing, H. J., Olofsson, H. 2004, *Asymptotic Giant Branch Stars*, Springer
- Hale, D. D. S., Bester, M., Danchi, W. C., Hoss, S., Lipman, E., Monnier, J. D., Tuthill, P. G., Townes, C. H., Johnson, M., Lopez, B., Geballe, T. R. 1997, *ApJ*, 490, 407
- Han, Z., Podsiadlowski, P., Eggleton, P. P. 1995, *MNRAS*, 272, 800
- Hecht, E. 2001, *Optics*, Addison-Wesley Publishing Company
- Herbig, G. H. 1970, *ApJ*, 162, 557
- Herbig, G. H. 1972, *ApJ*, 172, 375
- Herpin, F., Baudry, A., Thum, C., Morris, D., Wiesemeyer, H. 2006, *A&A*, 450, 667
- Herwig, F. 2005, *ARA&A*, 43, 435
- Hipparcos Catalogue, 1997, ESA SP-1200, CDS-VizieR (<http://vizier.u-strasbg.fr/viz-bin/Cat?I/239>)
- Huggins, P. J. 2007, *ApJ*, 663, 342
- Humphreys, R. M., Helton, L. A., Jones, T. J. 2007, *AJ*, 133, 2716
- Imai, H., Sasao, T., Kameya, O., Miyoshi, M., Shibata, K. M., Asaki, Y., Omodaka, T., Morimoto, M., Mochizuki, N., Suzuyama, T., Iguchi, S., Kameno, S., Jike, T., Iwadate, K., Sakai, S., Miyaji, T., Kawaguchi, N., Miyazawa, K. 1997, *A&A*, 317, 67
- Imai, H., Obara, K., Diamond, P. J., Omodaka, T., Sasao, T. 2002, *Natur*, 417, 829
- Imai, H., Fujii, T., Omodaka, T., Deguchi, S. 2008, *PASJ*, 60, 55
- Jacoby, G. H., 1980, *ApJS*, 42, 1
- Jones, T. J., Humphreys, R. M., Helton, L. A., Gui, C., Huang, X. 2007, *AJ*, 133, 2730
- Jordan, S., Werner, K., O'Toole, S. J. 2005, *A&A*, 432, 273
- Jordan, S., Bagnulo, S., Werner, K., O'Toole, S. J. 2012, *A&A*, 542, 64
- Jura, M. 1986, *IrAJ*, 17, 322
- Kaminski, T., Gottlieb, C. A., Young, K. H., Menten, K. M., Patel, N. A. 2013, *ApJS*, 209, 38

- Kastner, J. H., Weintraub, D. A., Zuckerman, B., Becklin, E. E., McLean, I., Gatley, I. 1992, *ApJ*, 398, 552
- Kastner, J. H., Weintraub, D. A. 1998, *AJ*, 115, 1592
- Kemball, A. J., Diamond, P. J., Cotton, W. D. 1995, *A&AS*, 110, 383
- Kim, J., Cho, S.-H., Oh, C. S., Byun, D.-Y. 2010 *ApJS*, 188, 209
- Kirrane T.-M., 1987, PhD thesis, University of Manchester
- Knapp, G. R., Pourbaix, D., Platais, I., Jorissen, A. 2003, *A&A*, 403, 993
- Kwok, S., Purton, C. R., Fitzgerald, P. M. 1978, *ApJ*, 219, 125
- Kwok, S. 1994, *PASP*, 106, 344
- Lafon, J.-P. J., Berruyer, N. 1991, *A&ARv*, 2, 249
- Leal-Ferreira, M. L., Vlemmings, W. H. T., Diamond, P. J., Kemball, A., Amiri, N., Desmurs, J.-F. 2012, *A&A*, 540, 42
- Leal-Ferreira, M. L., Vlemmings, W. H. T., Kemball, A., Amiri, N. 2013, *A&A*, 554, 134
- Leal-Ferreira, M. L., Ramstedt, S., Maercker, M., Olofsson, G., Vlemmings, W. H. T., Florén, H.-G. in preparation
- Leppänen, K. J., Zensus, J. A., Diamond, P. J. 1995, *AJ*, 110, 2479
- Lindqvist, M., Olofsson, H., Lucas, R., Schöier, F. L., Neri, R., Bujarrabal, V., Kahane, C. 1999, *A&A*, 351, 1
- Litvak, M. M. 1974, *ARA&A*, 12, 97
- Livio, M., Pringle, J. E. 1996, *ApJ*, 465, 55
- Livio, M., Pringle, J. E. 1997, *ApJ*, 486, 835
- Lyot, B. 1939, *MNRAS*, 99, 580
- Maciel, W. J. 1999, *Introdução à Estrutura e Evolução Estelar*, Editora da Universidade de São Paulo
- Maercker, M., Olofsson, H., Eriksson, K., Gustafsson, B., Schöier, F. L. 2010, *A&A*, 511, 37

- Maercker, M., Mohamed, S., Vlemmings, W. H. T., Ramstedt, S., Groenewegen, M. A. T., Humphreys, E., Kerschbaum, F., Lindqvist, M., Olofsson, H., Paladini, C., Wittkowski, M., de Gregorio-Monsalvo, I., Nyman, L.-A. 2012, *Natur*, 490, 232
- Maercker, M., Ramstedt S., Leal-Ferreira, M. L., Olofsson, G., Florén, H.-G. in preparation
- Maitland, A., Dunn, M. H. 1969, *Laser Physics*, North-Holland Publishing Company
- Manchado, A. 2003, *IAUS*, 209, 431
- Manchado A. 2012, *IAUS*, 283, 83
- Marvel, K. B. 1996, *PhDT*, 82
- Matt, S., Balick, B., Winglee, R., Goodson, A. 2000, *ApJ*, 545, 965
- Matt, S., Frank A., Blackman, E. G. 2006, *ApJ*, 647, 45
- Mattsson, L., Höfner, S., Herwig, F. 2007, *A&A*, 470, 339
- Mauron, N., Huggins, P. J. 2000, *A&A*, 359, 707
- Meixner, M., Ueta, T., Dayal, A., Hora, J. L., Fazio, G., Hrivnak, B. J., Skinner, C. J., Hoffmann, W. F., Deutsch, L. K. 1999, *ApJS*, 122, 221
- Migenes, V., Horiuchi, S., Slysh, V. I., Val'tts, I. E., Golubev, V. V., Edwards, P. G., Fomalont, E. B., Okayasu, R., Diamond, P. J., Umamoto, T., Shibata, K. M., Inoue, M. 1999, *ApJS*, 123, 487
- Miszalski, B., Acker, A., Moffat, A. F. J., Parker, Q. A., Udalski, A. 2009, *A&A*, 496, 813
- Moe, M., De Marco, O. 2006, *ApJ*, 650, 916
- Monnier, J. D., Millan-Gabet, R., Tuthill, P. G., Traub, W. A., Carleton, N. P., Coudé du Foresto, V., Danchi, W. C., Lacasse, M. G., Morel, S., Perrin, G., Porro, I. L., Schloerb, F. P., Townes, C. H. 2004, *ApJ*, 605, 436
- Morris, M., Bowers, P. F., Turner, B. E. 1982, *ApJ*, 259, 625
- Morris, M. 1987, *PASP*, 99, 1115
- Nordhaus, J., Blackman, E. G. 2006, *MNRAS*, 370, 2004
- Nordhaus, J., Blackman, E. G., Frank, A. 2007, *MNRAS*, 376, 599
- Nyman, L.-A., Johansson, L. E. B., Booth, R. S. 1986, *A&A*, 160, 352

- Olofsson, H., Eriksson, K., Gustafsson, B. 1988, A&A, 196, 1
- Olofsson, H., Bergman, P., Eriksson, K., Gustafsson, B. 1996, A&A, 311, 587
- Olofsson, H.; Lindqvist, M.; Nyman, L.-A.; Winnberg, A. 1998, A&A, 329, 1059
- Olofsson, H., Maercker, M., Eriksson, K., Gustafsson, B., Schöier, F. 2010, A&A, 515, 27
- Olofsson, G., Nilsson, R., Florén, H.-G., Djupvik, A., Aberasturi, M. 2012, A&A, 544, 43
- Pascoli, G., Lahoche, L. 2008, PASP, 120, 1267
- Pascoli, G. Lahoche, L. 2010, PASP, 122, 1334
- Peimbert, M. 1990, RMxAA, 20, 119
- Peimbert, M. 1993, IAUS, 155, 523
- Pérez-Sánchez, A. F., Vlemmings, W. H. T., Chapman, J. M. 2011, MNRAS, 418, 1402
- Peters, G. J.; Hirschi, R. 2013, *Planets, Stars and Stellar Systems*, Vol. 4, ISBN 978-94-007-5614-4. Springer Science+Business Media Dordrecht
- Ragland, S., Traub, W. A., Berger, J.-P., Danchi, W. C., Monnier, J. D., Willson, L. A., Carleton, N. P., Lacasse, M. G., Millan-Gabet, R., Pedretti, E.; Schloerb, F. P., Cotton, W. D., Townes, C. H., Brewer, M., Haguenaue, P., Kern, P., Labeye, P., Malbet, F., Malin, D., Pearlman, M., Perraut, K., Souccar, K., Wallace, G. 2006, ApJ, 652, 650
- Ransom, R. R.; Uyaniker, B.; Kothes, R.; Landecker, T. L. 2008, ApJ, 684, 1009
- Ramstedt, S., Schöier, F. L., Olofsson, H., Lundgren, A. A. 2008, A&A, 487, 645
- Ramstedt, S., Maercker, M., Olofsson, G., Olofsson, H., Schöier, F. L. 2011, A&A, 531, 148
- Reid, M. J., Moran, J. M., Leach, R. W., Ball, J. A., Johnston, K. J., Spencer, J. H., Swenson, G. W. 1979, ApJ, 227, 89
- Reid, M. J. 1990, IAUS, 140, 21
- Reid, M. J., Menten, K. M. 1997, ApJ, 476, 327
- Reid, M. J., Menten, K. M. 2007, ApJ, 671, 2068
- Richards, A. M. S., Elitzur, M., Yates, J. A. 2011, A&A, 525, 56

- Richards, A. M. S., Etoke, S., Gray, M. D., Lekht, E. E., Mendoza-Torres, J. E., Murakawa, K., Rudnitskij, G., and Yates, J. A. 2012, *A&A* 546, 16
- Rudnitski, G. M., Pashchenko, M. I., Colom, P. 2010, *ARep*, 54, 400
- Sahai, R., Morris, M. R., Villar, G. G. 2011, *AJ*, 141, 134
- Sánchez Contreras, C. 1997, *AcC*, 23, 175
- Sánchez Contreras, C., Desmurs, J. F., Bujarrabal, V., Alcolea, J., Colomer, F. 2002, *A&A*, 385, 1
- Sánchez Contreras, C., Gil de Paz, A., Sahai, R. 2004, *ApJ*, 616, 519
- Schöier, F. L., Lindqvist, M., Olofsson, H. 2005, *A&A*, 436, 633
- Sedlmayr, E. 1994, in *Molecules in the Stellar Environment*, LNP 428, 163, ed. U. G. Jørgensen (Berlin: Springer)
- Shaw, R. A. 2012, *IAUS*, 283, 156
- Shintani, M., Imai, H., Ando, K., Nakashima, K., Hirota, T., Inomata, N., Kai, T., Kamenno, S., Kijima, M., Kobayashi, H., Kuroki, M., Maeda, T., Maruyama, K., Matsumoto, N., Miyaji, T., Nagayama, T., Nagayoshi, R., Nakamura, K., Nakagawa, A., Namikawa, D., Omodaka, T., Oyama, T., Sakakibara, S., Shimizu, R., Sora, K., Tsushima, M., Ueda, K., Ueda, Y., Yamashita, K. 2008, *PASJ*, 60, 1077
- Shure, M., Sellgren, K., Jones, T. J., Klebe, D. 1995, *AJ*, 109, 721
- Smith, N., Humphreys, R. M., Davidson, K., Gehrz, R. D., Schuster, M. T., Krautter, J. 2001, *AJ*, 121, 1111
- Soker, N., Livio, M. 1994, *ApJ*, 421, 219
- Soker, N. 1997, *ApJS*, 112, 487
- Soker, N. 1998, *ApJ*, 496, 833
- Soker, N. 2006, *PASP*, 118, 260
- Stanghellini, L., Corradi, R. L. M., Schwarz, H. E. 1993, *A&A*, 279, 521
- Steffen, M., Schönberner, D. 2000, *A&A*, 357, 180
- Sudou, H., Omodaka, T., Imai, H., Sasao, T., Takaba, H., Nishio, M., Hasegawa, W., Nakajima, J. 2002, *PASJ*, 54, 757

- Surcis, G., Vlemmings, W. H. T., Curiel, S., Hutawarakorn Kramer, B., Torrelles, J. M., Sarma, A. P. 2011, *A&A*, 527, A48
- Swihart, T. L. 1968, *Astrophysics and Stellar Astronomy*, New York John Wiley
- Szymczak, M., Błaszkiwicz, L., Etoke, S., Le Squeren, A. M. 2001, *A&A*, 379, 884
- Uyaniker, B. 2004, in *The Magnetized Interstellar Medium*, ed. B. Uyaniker, W. Reich, & R. Wielebinski (Katlenburg-Lindau: Copernicus GmbH), 71
- Villaver, E., Manchado, A., García-Segura, G. 2012, *ApJ*, 748, 94
- Villaver, E., Garcia-Segura, G., Manchado, A., Stanghellini, L. 2014, *Asymmetrical Planetary Nebulae VI conference proceedings*, ed. C. Morisset, G. Delgado-Inglada & S. Torres-Peimbert, 110
- Vlemmings, W., Diamond, P. J., van Langevelde, H. J. 2001, *A&A*, 375, 1
- Vlemmings, W. H. T., Diamond, P. J., van Langevelde, H. J. 2002, *A&A*, 394, 589
- Vlemmings, W. H. T., van Langevelde, H. J., & Diamond, P. J. 2005, *A&A*, 434, 1029
- Vlemmings, W. H. T., Diamond, P. J., Imai, H. 2006, *Natur*, 440, 58
- Vlemmings, W. H. T., Diamond, P. J. 2006, *ApJ*, 648, 59
- Vlemmings, W. H. T. 2007, *IAUS* ,242 ,37
- Vlemmings, W. H. T., Ramstedt, S., Rao, R., Maercker, M. 2012, *A&A*, 540, 3
- Walker, R. C. 1999, *ASPC*, 180, 433
- Wardle, J. F. C., Kronberg, P. P. 1974, *ApJ*, 194, 249
- Wehmeyer, R., Kohoutek, L. 1979, *A&A*, 78, 39
- Weiner, J., Tatebe, K., Hale, D. D. S., Townes, C. H., Monnier, J. D., Ireland, M., Tuthill, P. G., Cohen, R., Barry, R. K., Rajagopal, J., Danchi, W. C. 2006, *ApJ*, 636, 1067
- Weinzielrl, S. 1991, *Diplomarbeit*, Technische Universität, Berlin
- Whittet, D. C. B. 1996, in *Greenberg J. M., ed., The Cosmic Dust Connection*. Kluwer, Dordrecht, p. 155
- Wing, R. F., Lockwood, G. W. 1973, *ApJ*, 184, 873

Wolak, P., Szymczak, M., Gérard, E. 2012, *A&A*, 537, 5

Yates, J. A., 1993, PhD thesis, University of Manchester

Yates, J. A., Cohen, R. J. 1994, *MNRAS*, 270, 958

Zeeman, P. 1897, *Philosophical Mag.*, 43, 226

Zhang, B., Reid, M. J., Menten, K. M., Zheng, X. W. 2012, *ApJ*, 744, 23

Zijlstra, A. A., Chapman, J. M., te Lintel Hekkert, P., Likkell, L., Comeron, F., Norris, R. P., Molster, F. J., Cohen, R. J. 2001, *MNRAS*, 322, 280



# Abbreviations

**AARP** = Azimuthal Averaged Radial Profile

**AGB** = Asymptotic Giant Branch

**AIPS** = Astronomical Image Processing System

**ALMA** = Atacama Large Millimeter/submillimeter Array

**CSE** = Circumstellar Envelope

**eMERLIN** = extended Multi-Element Radio Linked Interferometer

**ESO** = European Southern Observatory

**EVPA** = Electric Vector Position Angle

**FWHM** = Full Width at Half Maximum

**HST** = Hubble Space Telescope

**ISM** = Interstellar Medium

**LSR** = Local Standard of Rest

**LTE** = Local Thermodynamic Equilibrium

**MHD** = Magnetohydrodynamic

**PN** = Planetary Nebula

**PNe** = Planetary Nebulae

**POLA** = Polarization angle

**PolCor** = Polarimeter and Coronagraph

**POLI** = Polarization intensity

**PSF** = Point Spread Function

**RSG** = Red Supergiant

**SMA** = Submillimeter Array

**SNR** = Signal to noise ratio

**VLBA** = Very Long Baseline Array

**VLBI** = Very Long Baseline Interferometry

# Acknowledgments

*I would like to reserve some space in this thesis to express my gratitude to several people that were fundamental in the accomplishment of this thesis. I am sure that without the help of each one of them I would not have been able to perform the work presented here.*

*First of all, I would like to express a big thank you to Wouter Vlemmings, the advisor of my PhD project. Thank you for giving me the opportunity to perform this research, and for your kindness and patience during the whole time that I have been working with you. You are an amazing advisor! Thank you also for providing me the chance to attend conferences, summer schools, observations and training trips. I extend similar acknowledgments to Sofia Ramstedt and Matthias Maercker, members of our research group. Thank you both for offering me the chance to work in the PolCor project and thank you for your support in the performance of the respective part of my thesis. Göran Olofsson, I would also like to thank you for your helpful support during the work in the PolCor project. Many thanks also to Frank Bertoldi, who accepted me as his formal student once Wouter moved to Sweden.*

*Thank you to all members of the IT staff of AIfA, in particular to Reinhold Schaaf, for your always fast help regarding the installation of software and/or packages, and on fixing bugs. I also add special thanks to my desktop aibn82, which did not present any major problems during my stay in Bonn. Gabriele Surcis and Ramiro Franco Hernández, your help on working with AIPS were fundamental in the beginning of my PhD project, and for that I am very grateful.*

*I thank Adam Frank and his group, in particular Martin Huarte-Espinosa, for hosting me in Rochester in the fall of 2010 and for introducing me to the AstroBEAR code.*

*Thank you, DAAD for offering me a fellowship to perform this research project. I am*

also grateful to the DAAD staff, in particular to Maria Salgado, for being always helpful regarding the paperwork and further bureaucratic issues.

*Christina Stein-Schmitz* I have no words to expose my gratitude to you. You have always been extremely helpful regarding paperwork, but that was not all. You have welcomed me in Bonn and made me feel comfortable in a new country since my first day in Germany. As if that was not enough, you have always shared your good mood with me, and that meant a lot to me.

Some other people have also been important to make me feel comfortable in Bonn in my first weeks in Germany. I would like to thank Iskren, Jackie, Guilherme, Amanda, and Patricia for embracing me on my arrival. Thank you also to Letícia and to Andrés for your support in my first months in Bonn. Your support was very important to me.

Along the years I stayed in Bonn, I was lucky enough to meet nice people that I can happily consider friends today. Your friendships were substantial for my welfare in Bonn, and you were my Bonn family during these last years. Thank you for that Anna, Felipe, Katha, Benja, Maria, Tatiana, Hananeh, JC, and Aarti. I am also very thankful for every single friend that visited me in Bonn, making me feel closer to home. Thank you Guto, Álvaro, Bruna, Gina, Camila, Betão, Bebel, Tche, Eduardo, Felipe, Theo, Gi, Pilar, Wlad, and JP. I add to this list my mom, brother and aunt, whose visits always gave me extra motivation. Moreover, even from across the Ocean, your encouragement and trust were very important during the process of my PhD project.

I am also grateful to Denise Gonçalves and to Carlos Rabaça, my master's and bachelor's advisors, respectively. Thank you both to introduce me to the evolved stars field, and for inspiring me to follow this path. Without your influences I would not be here today.

Thank you for everyone that proof-read my thesis. Your comments and suggestions were extremely helpful: Wouter Vlemmings, Matthias Maercker, Sofia Ramstedt, Jean-Claude Passy, Richard Stancliffe, Tomasz Kaminski, Rodolfo Montez, and Sandra Martin.

Finally, nothing that I write here would be sufficient to express how much I appreciate your support in the last months of this thesis, Sandra. Thank you for cheering me up and calming me down in moments of stress. Thank you for your company and for being there for me. You were amazing during the whole time!





# Curriculum Vitae

## Personal Details

Name	Marcelo de Lima Leal Ferreira
Email	ferreira@astro.uni-bonn.de

## Education

1997–1999	High School, Colégio Sagrado Coração de Maria, Rio de Janeiro, Brazil.
2000–2007	BSc in Astronomy, Universidade Federal do Rio de Janeiro, Rio de Janeiro, Brazil.
2007–2009	MSc in Astrophysics, Universidade Federal do Rio de Janeiro, Rio de Janeiro, Brazil.
2010–	PhD in Astrophysics, Universität Bonn, Bonn, Germany.

## Languages

Portuguese	Native speaker
English	Fluent
Spanish	Basic

## Professional Experience

- 2003 | Poster Presentation at Yearly Reunion of the Brazilian Astronomical Society, São Pedro, Brazil.
- 2003 | Student at VIII Cycle of Special Courses at National Observatory, Rio de Janeiro, Brazil.
- 2004 | Student at I GEMAC Course on Star Formation in Galaxies at Valongo Observatory, Rio de Janeiro, Brazil.
- 2004 | Poster Presentation at Yearly Reunion of the Brazilian Astronomical Society, São Pedro, Brazil.
- 2004 | Student at V School on Image Processing at CBPF, Rio de Janeiro, Brazil.
- 2004 | Student at V School on Nuclear Physics and Stellar Evolution at CBPF, Rio de Janeiro, Brazil.
- 2004 | Student at IX Cycle of Special Courses at National Observatory, Rio de Janeiro, Brazil.
- 2005 | Poster Presentation at Yearly Reunion of the Brazilian Astronomical Society, Águas de Lindóia, Brazil.
- 2005 | Student at Latin American Astronomy Summer School at ESO, Santiago, Chile.
- 2006 | Poster Presentation at Yearly Reunion of the Brazilian Astronomical Society, Atibaia, Brazil.
- 2006 | Student at XI Cycle of Special Courses at National Observatory, Rio de Janeiro, Brazil.
- 2007 | Talk and Poster Presentation at Yearly Reunion of the Brazilian Astronomical Society, Passa Quatro, Brazil.
- 2007 | Two Poster Presentations at Asymmetrical Planetary Nebula IV Conference, La Palma, Spain.
- 2007 | Student at XII Cycle of Special Courses at National Observatory, Rio de Janeiro, Brazil.
- 2007 | Student at III Chilean Advanced School on Astrophysics at Universidad de Concepción, Concepción, Chile.
- 2008 | Student at XIII Cycle of Special Courses at National Observatory, Rio de Janeiro, Brazil.
- 2009 | Poster Presentation at IAU XXVII General Assembly, Rio de Janeiro, Brazil.
- 2009 | Student at III Advanced Course on Astrophysics at INPE, São José dos Campos, Brazil.
- 2010 | Poster Presentation at Asymmetrical Planetary Nebula V Conference, Manchester, United Kingdom.
- 2010 | Training at University of Rochester, Rochester, United States of America.



- 2011 | Talk at Valongo Observatory, Rio de Janeiro, Brazil.
- 2011 | First Author Article Published at MNRAS Journal, 411, 1395.
- 2011 | Poster Presentation at IAU Symposium 283, Tenerife, Spain.
- 2011 | Student at European Radio Interferometry School at INAF, Rimini, Italy.
- 2012 | Poster Presentation at IAU Symposium 287, Stellenbosch, South Africa.
- 2012 | First Author Article Published at A&A Journal, 540, 42.
- 2012 | Talk at Young European Radio Astronomy Conference, Pushchino, Russia.
- 2013 | First Author Article Published at A&A Journal, 554, 134.
- 2013 | Talk at Asymmetrical Planetary Nebula VI Conference, Riviera Maya, Mexico.
- 2013 | Third Author Article Published at A&A Journal, 560, 102.

## Outreach & Related

- 2004 | Hands on activities and planetarium presentations at Project UFRJ in the Schools, Búzios, Brazil.
- 2004 | Hands on activities and planetarium presentations at Exhibition of the Integrated Knowledge, Arraial do Cabo, Brazil.
- 2004 | Hands on activities and planetarium presentations at National Week of Science and Technology, Rio de Janeiro, Brazil.
- 2005 | Hands on activities and planetarium presentations at UFRJmar, Cabo Frio, Brazil.
- 2005 | Hands on activities and planetarium presentations at Astronomy at Casimiro de Abreu, Casimiro de Abreu, Brazil.
- 2005 | Hands on activities and planetarium presentations at National Week of Science and Technology, Rio de Janeiro, Brazil.
- 2006 | Hands on activities and planetarium presentations at National Week of Science and Technology, Rio de Janeiro, Brazil.
- 2011 | Talk at DAAD Stipendiatentreffen, Dortmund, Germany.
- 2012 | Invited talk at DAAD Orientierungsseminar, Bonn, Germany.
- 2013 | Invited talk at DAAD Orientierungsseminar (May), Bonn, Germany.
- 2013 | Invited talk at DAAD Orientierungsseminar (October), Bonn, Germany.
- 2014 | Invited talk at DAAD Orientierungsseminar, Bonn, Germany.

**Awards & Fellowships**

2003–2004	Scientific Initiation Fellowship (FAPERJ, Brazil), Brazil
2006	Best talk at Sputnik Session of Scientific Initiation Journey (Valongo Observatory, Brazil), Brazil
2006–2007	Scientific Initiation Fellowship (CNPq/PIBIC, Brazil), Brazil
2007–2009	MSc Fellowship (CAPES, Brazil), Brazil
2008	Outstanding Scholarly (CCMN/UFRJ, Brazil), Brazil
2011–	PhD Fellowship (DAAD, Germany), Germany
2014–	Postdoc Fellowship (CsF, Brazil), Netherlands (offered)